Upper Troposphere Lower Stratosphere structure during convective systems using GPS radio occultations

Biondi, Riccardo; Neubert, Torsten; B. Larsen, Georg

Publication date:
2012

Document Version
Publisher's PDF, also known as Version of record

Upper Troposphere Lower Stratosphere structure during convective systems using GPS radio occultations

PhD student: Riccardo Biondi

PhD committee

Supervisor:	Torsten Neubert (DTU Space - Denmark)
Co-supervisor:	Georg B. Larsen (DMI - Denmark)
Chairman:	Per Høeg (DTU space - Denmark)
External member:	Kent Lauritsen (DMI - Denmark)
External member:	Jean Pierre Pommereau (CNRS - France)

DTU Space
National Space Institute

Dedicated to my Dad and my Mom

Abstract

The deep convective systems play a fundamental role in atmospheric circulation and climate. Thunderstorms and meso-scale convective systems produce fast vertical transport, redistributing water vapor and trace gases and influencing the thermal structure of the upper troposphere and lower stratosphere (UTLS) contributing to the troposphere-stratosphere transport and affecting the Earth global circulation and the climate changes. The Global Positioning System (GPS) Radio Occultation (RO) technique enables measurement of atmospheric density structure in any meteorological condition, with extremely high accuracy, precision and vertical resolution, providing a global coverage of the Earth. The objective of this thesis is to understand if the radio occultation technique can be used to study the water vapor in the UTLS, and to characterize the convective processes. The contribution to the analysis of tropical storms for the future mission ACES will also be evaluated.

Using data from the past and ongoing GPS RO missions we have defined an algorithm to detect the clouds top of the convective systems and their thermal structure. Other satellite and in-situ measurements co-located with GPS ROs, were used to validate the results.
The outcomes are very promising. The GPS signal can be used to characterize the thermal structure of the convective systems, and to detect the storm cloud top. The RO signal contains interesting information in connection to the troposphere–stratosphere transport providing a clear signature of these processes on the atmosphere.
However the signal is not sensitive enough to detect the variation of water vapor in the UTLS. The ongoing GPS RO missions do not provide a suitable Earth coverage in order to allow a systematic study of convective systems and an increase of soundings in the tropical area is requested to exploit all the capabilities of this technique.

Dansk Resumé

Tordenvejr er dybe konvektive systemer, som spiller en fundamental rolle for atmosfærens cirkulation og for jordens klima. Den kraftige, vertikale transport påvirker den termiske struktur i den øvre troposfære og nedre stratosfære (UTLS), omfordeler vanddamp og sporgasser, og påvirker Jordens globale cirkulation og klimaændringer. Radio Okulationsteknikker (RO) er udviklede til at måle parametre, der karakteriserer atmosfæren og som assimileres i vejrmodeller. RO udnytter perturbationer i de præcise signaler fra Global Positioning System (GPS) satellitterne, som modtages på andre satellitter. Ændringer i signalet, når det passerer gennem atmosfæren, gør det muligt at måle atmosfærens massefylde uanset de meteorologiske betingelser, og dette kan gøres med stor nøjagtighed, præcision og vertikal opløsning. Et sådant satellitbaseret system har desuden den store fordel at dække hele Jorden.

Ved hjælp af data fra tidligere og nuværende GPS RO-missioner, har vi søgt at udtrække information om den øverste troposfære og nederste stratosfære for at undersøge transporten af vandamp i dette område. Ved disse højder er atmosfæren så tynd, at ændringer i GPS signalet er ganske små. Det er imidlertid lykkedes at defineret en algoritme, der kan detektere de konvektive systemers skytoppe og systemernes termiske struktur. RO-signalet indeholder dermed interessante informationer omkring troposfære-stratosfære-transporten. Perturbationerne i GPS signalet er imidlertid ikke store nok til direkte at detektere ændringer i vanddampen i UTLS. Endvidere tillader de nuværende RO-missioner ikke en tilstrækkelig dækning af Jorden for en systematisk analyse af konvektive systemer. Dette må vente til næste generation GPS og fremtidige RO satellit konstellationer.

Validering af vore konklusioner er gjort ved udnyttelse af et stort antal observationer fra andre satellit- og in-situ målinger.

Acknowledgements

I would like to thank my supervisors, *Torsten Neubert* and *Georg Larsen,* for giving me the great opportunity to spend these 3 years at DTU Space working in this nice and inspiring environment. I´m extremely grateful to *Torsten* for his patience, sympathy and availability any time I needed it.

Special thanks to:
Stig Syndengaard, always present during these 3 years giving me advices and supporting in all the issues.
Bill Randel, giving me the opportunity to spend a wonderful and worthwhile period at NCAR and teaching me a lot even with the short time available.
Ben Ho, believing in my job from the first time we met and always available to develop my ideas.
Francesco Cairo, giving me the opportunity to spend a short period at ISAC-CNR and "helping my future".

I would also like to thank *Johannes Nielsen, Rich Rotunno, Joan Alexander, Georg Beyerle* and *Federico Fierli* helping me in different ways during this study.

Thank you to *Lene* always ready to help and a big thank you to *Birte* always taking care of my problems either professional or personal.

Thank you to my "Danish" friends *Matija, Stavros, Joanna, Olivier, Yongcun, Deniz, Valentina* and *Andrea* for keeping me alive.

Thank you to *my sister* and *my mother* accepting me to live so far during this extremely difficult period.

Thanks to *Sabrina* for sharing with me her life as much as she could.

Table of Contents

List of Figures 4
List of Tables 6
List of Abbreviations 7
Chapter 1 9
Introduction 9
1.1 Motivation 9
1.2 Objectives 10
1.3 Thesis contents 10
Chapter 2 12
Background 12
2.1 The convective systems and the troposphere-stratosphere interaction 12
2.2 The stability of the atmosphere 13
2.3 The water vapor in the Upper Troposphere Lower Stratosphere 17
2.4 The GPS radio occultation technique and the International Space Station 19
Chapter 3 22
Data description 22
3.1 The convective systems and the tropical cyclones 22
3.2 Satellite data 23
3.2.1 The GPS radio occultations data 23
3.2.2 The Cloud-Aerosol Lidar and Infrared Pathfinder Satellite Observation data 24
3.2.3 The geostationary satellites data 25
3.3 In situ measurements 25
3.3.1 The radiosondes data 26
3.3.2 The airborne data 26
3.3.2 The World Wide Lightning Location Network data 27
3.4 Models 28
3.4.1 The ECMWF re-analyses 28
3.4.2 The Cloud Model 1 28
Chapter 4 29

Methodology 29
4.1 The GPS radio occultation technique 29
4.2 The bending angle anomaly technique 32
4.3 Cloud top detection algorithm 35
4.4 Validation of the technique 36
Chapter 5 38
Data analysis 38
5.1 The GPS radio occultation parameters and sensitivity 38
5.2 Tropical cyclones 41
5.2.1 Case study: Bertha 2008 44
5.2.2 Case study: Bill 2009 51
5.2.3 Case study: Krosa 2007 54
5.2.4 The TC top determination 56
5.2.5 Model analysis 58
5.2.6 Statistics 66
5.3 Convective systems 70
5.3.1 Case study 72
5.3.2 Statistics 76
5.3.3 Campaigns data analysis 81
Chapter 6 90
Discussion 90
6.1 Results 90
6.2 Uncertainties of the method 91
6.3 Applications 92
6.4 Originality, relevance and impact of the project 93
Chapter 7 95
Summary and conclusions 95
References 98
Appendices 107
Published works 107
Appendix A 108
Appendix B 117

Appendix C..... 126

List of Figures

2.1 Cartoon of convective system anvil formation 17
2.2 COSMIC radio occultations latitudinal distribution 20
2.3 ACES radio occultations latitudinal distribution 21

3.1 Tropical cyclones best tracks 23

4.1 GPS radio occultation technique scheme 31
4.2 GPS radio occultation coverage 32
4.3 Bending angle anomaly with different references 34
4.4 Bending angle anomaly in respect to annual and monthly climatology 35

5.1 Refractivity profile during tropical cyclone 39
5.2 Sensitivity analysis of refractivity 40
5.3 Tropical cyclone bending angle trend 44
5.4 Hurricane Bertha – track 45
5.5 Bertha track reconstruction 47
5.6 Bertha bending angle anomaly compared to local monthly means 48
5.7 Atmospheric parameters profiles during Bertha 49
5.8 Bending angle anomaly and temperature profiles during a case of Bertha 50
5.9 Averaged bending angle anomaly profile during Bertha 51
5.10 Hurricane Bill - case study 52
5.11 GOES brightness temperature inversion during Bill 53
5.12 Bending angle anomaly and temperature profiles during a case of Bill 54
5.13 Typhoon Krosa – case study 55
5.14 Krosa cloud top detection using GPS and CALIPSO 56
5.15 Tropical cyclones cloud top detection using GPS and CALIPSO 57
5.16 Bending angle anomaly and temperature profiles during tropical cyclones 58
5.17 Simulated vertical wind cross section during tropical cyclone 61
5.18 Simulated v-component wind cross section during tropical cyclone 62
5.19 Simulated u-component wind cross section during tropical cyclone 63
5.20 Simulated anvil cloud cross section during tropical cyclone 64
5.21 Simulated temperature anomaly cross section during tropical cyclone 65
5.22 Simulated temperature soundings during tropical cyclone 66
5.23 Distribution of positive bending angle anomalies in the UTLS 67
5.24 Distribution of mean negative bending angle anomalies in the UTLS 68
5.25 Temperature from radiosondes and GPS during tropical cyclones 69

5.26 Bending angle and RAOB temperature profiles during tropical cyclones 70
5.27 Convective clusters map 72
5.28 Case study cloud top detection from GPS and CALIPSO 75
5.29 Convective systems cloud top detection using GPS and CALIPSO 77
5.30 Temperature anomaly profiles during convective systems 78
5.31 Bending angle anomaly profiles during convective systems 79
5.32 Lapse rate profiles during convective systems 80
5.33 Convective systems thermal structure 81
5.34 AMMA campaign 8th of August 2006 - case study 82
5.35 AMMA campaign 8th of August 2006 - profiles 83
5.36 AMMA campaign 8th of August 2006 - profiles 84
5.37 AMMA campaign 11th of August 2006 - case study 85
5.38 AMMA campaign 11th of August 2006 - profiles 86
5.39 AMMA campaign 11th of August 2006 - profiles 87
5.40 TC4 campaign 6th of August 2007 – case study 88
5.41 TC4 campaign 6th of August 2007 – profiles 89

List of Tables

5.1 GPS radio occultation availability 41
5.2 GPS radio occultations co-located with tropical cyclones 42
5.3 GPS radio occultations during different storm strengths 42
5.4 GPS radio occultations co-located with tropical cyclones and CALIPSO 43
5.5 GPS radio occultations co-located with convective systems and CALIPSO 71

List of Abbreviations

ACES	Atomic Clock Ensemble in Space
ASIM	Atmosphere-Space Interactions Monitor
atmPrf	atmospheric Profile
BT	Brightness Temperature
CALIOP	Cloud-Aerosol Lidar with Orthogonal Polarization
CALIPSO	Cloud-Aerosol Lidar and Infrared Pathfinder Satellite Observation
Cat.	Category
CC	Convective Cluster
CDAAC	COSMIC Data Analysis and Archive Center
CHAMP	CHAllenging Minisatellite Payload
CLASS	Comprehensive Large Array Data Stewardship System
CLIVAR	CLImate VARiability and predictability
CM1	Cloud Model 1
COSMIC	Constellation Observing System for Meteorology, Ionosphere and Climate
CPL	Cloud Physics Lidar
CS	Convective System
ecmPrf	ECMWF Profile
ECMWF	European Centre for Medium-Range Weather Forecasts
FISH	Fast In-Situ Hygrometer
FLASH	Fluorescent Airborne Stratospheric Hygrometer
FSL	Forecast System Laboratory
GCSS	Global Cloud Systems Study
GEOSS	Global Earth Observation System of Systems
GEWEX	Global Earth's Water Experiment
GLONASS	GLObal NAvigation Satellite System
GMS	Geostationary Meteorological Satellite
GOES	Geostationary Operational Environmental Satellite
GPS-MET	Global Positioning System/Meteorology
GRACE	Gravity Recovery And Climate Experiment
GPS	Global Positioning System
IPCC	Intergovernamental Panel on Climate Changes
IRNSS	Indian Regional Navigational Satellite System
ISCCP	International Satellite Cloud Climatology Project
ISS	International Space Station
JAXA	Japan Aerospace Exploration Agency

JMA	Japan Meteorological Agency
LEO	Low Earth Orbit
MAS	Multiwavelength Aerosol Scatterometer
MetOp	Meteorological Operational
MTSAT	Meteorological SATellite
NOAA-ESRL	National Oceanic and Atmospheric Administration Earth System Research Laboratory
PSC	Polar Stratospheric Clouds
ppmv	part per million in volume
QZSS	Quasi-Zenith Satellite System
RAOB	RAdiosonde OBservation
RO	Radio Occultation
ROSA	Radio Occultation for sounding the Atmosphere
SAC-C	Satellite de Aplicaciones Cientificas-C
sonPrf	sonde Profile
SPARC	Stratospheric Processes and their Role in Climate within the World Climate Research
TC	Tropical Cyclone
TD	Tropical Depression
TOGA (ECMWF)	Tropical Ocean and Global Atmosphere
TOGA (WWLLN)	Time Of Group Arrival
TS	Tropical Storm
UTC	Coordinated Universal Time
UTLS	Upper Troposphere Lower stratosphere
VLF	Very Low Frequency
wetPrf	wet Profile
WWLLN	World Wide Lightning Location Network

Chapter 1

Introduction

1.1 Motivation

The convective systems pump the water vapor in the upper troposphere and lower stratosphere (UTLS) and they modify the thermal structure of the atmosphere contributing to the troposphere-stratosphere transport and affecting the Earth global circulation and the climate changes.

The central purpose of this study is to improve techniques for detection of atmospheric water vapor and to study the transport above severe thunderstorms using the GPS radio occultation technique. The study is related to two missions planned for the external payload platforms on the Columbus module of the International Space Station (ISS) in 2015. One is the "Atmosphere-Space Interactions Monitor" (ASIM) (Neubert et al., 2009) for observations of extreme thunderstorms and their influence on the atmosphere and the other one is the "Atomic Clock Ensemble in Space" (ACES). ASIM project is led by DTU-Space and includes a number of optical instruments to observe electrical discharges in the stratosphere and mesosphere and some cloud parameters. ACES payload includes a GPS receiver (led by the Technical University of Münich) that can be used for limb sounding measurements of atmospheric density, and estimation of temperature and water vapor content with high vertical resolution and accuracy. The ACES limb sounding combined with the ASIM optical limb observations of cloud cover will provide new insights on the UTLS transport from convective systems. The UTLS is today studied from satellites though without an appropriate vertical resolution and coverage. The limb sounding technique from the ISS then holds the promise of both giving important altitude distributions and complete coverage of the tropical regions of the Earth thank to its orbit inclination of 51.6^{o}. With these instruments the ISS may potentially ensure a unique data set on tropopause processes, and it will contribute to increase the number of occultation measurements in the tropical regions expected having increased importance for monitoring climate change together with Europe's investment in the Galileo project.

1.2 Objectives

This thesis has multiple objectives. The first one is to understand if the radio occultation technique can contribute to the study of the water vapor in the UTLS. The second aim is to assess the contribution that ACES GPS receiver will provide to the tropical areas coverage with high vertical resolution density profiles. The last but not the least objective is to use the GPS radio occultation receivers to characterize the convective systems processes.
In other words we would like to answer the following 3 questions:

1) What is the contribution that the future missions ACES will provide to the study of the convection?
2) Is the GPS signal able to provide information on the water vapor content in the UTLS during extreme events?
3) Is the GPS signal able to provide any interesting information on troposphere-stratosphere transport?

1.3 Thesis contents

The thesis is structured in 7 chapters describing the work done and 3 appendices, each one reporting a publication related to this PhD project.

This chapter outlines the motivation (1.1), the objective that we want to reach (1.2), and the structure of the thesis itself (1.3).

The second chapter provides the status of the art giving a short background on the convective systems physics and dynamics and the interaction processes between the troposphere and the stratosphere (2.1 and 2.2), the role of the water vapor in the Upper Troposphere and Lower Stratosphere, the chemistry and its connection to the climate changes (2.3) and a brief introduction to the technique that we are going to use which will soon also be available from the International Space Station (2.4).

The third chapter describes the dataset used for this work. The convective systems and the tropical cyclones are first introduced (3.1). The satellite datasets from GPS, meteorological geostationary satellites and polar satellites are presented (3.2) as the principal tool to achieve the expected results. In situ measurements from radiosondes,

aircraft and lightning network (3.3) are outlined to validate the acquisitions from satellite and finally the models (3.4) providing the theoretical effectiveness of the achievements.

The fourth chapter addresses the methodology used to reach the objectives. After an introduction on the theory of the GPS radio occultation technique (4.1), the new "bending angle anomaly technique" is introduced (4.2), followed by a description on how the convective systems can be detected using the GPS signal (4.3). The validation procedure is then presented (4.4).

In the fifth chapter the main activity that has been done during the PhD project is presented. All the parameters used in this work and their sensitivity are introduced (5.1) and specific cases study, tropical cyclones (5.2) and convective systems (5.3), are described in detail, comparing all the results from the GPS radio occultations with other satellite and in situ measurements.

The sixth chapter shows the most significant results achieved during this work (6.1), describes the uncertainties of the method (6.2), presents the originality, the relevance and the impact of this project (6.3) and finally shows the future applications of the new technique (6.4).

The summary and the conclusions are given in the chapter 7.

Chapter 2

Background

2.1 The convective systems and the troposphere-stratosphere interaction

Tropospheric air that enters the stratosphere in the tropics is caught in the ascending branch of the Brewer-Dobson circulation (Brewer, 1949; Dobson, 1956) hence it is able to influence the whole stratosphere. The processes in the tropical Upper Troposphere and Lower Stratosphere (UTLS) determine the composition of air and the global circulation. Several studies have shown the importance of water vapor transport in the UTLS which plays a major role in the climate changes (Manabe and Wetherald, 1967; Soden and Fu, 1995; Forster and Shine, 2002; Solomon et al., 2010) and having an impact comparable to those due to carbon dioxide (CO_2) trends (Forster and Shine, 2002; Solomon et al., 2010). A small increase of water vapor concentration in the UTLS contributes to the cooling of the stratosphere (Forster and Shine, 1999) and the warming of the troposphere, but the reason of the water vapor variation at those altitudes is largely unknown and still debated (Scherer et al., 2008; Fueglistaler et al., 2009).

Newell and Gould-Stewart (1981) assume the troposphere-stratosphere transport to be preferentially over Micronesia where the coldest tropopause was detected but other cases of convective penetration have been later detected in different areas (Danielsen, 1982, 1993; Liu and Zipser, 2005; Pommereau and Held, 2007; Chaboureau et al., 2007; Corti et al., 2008). This suggests that the overshooting is more frequent than expected and the troposphere-stratosphere transport can occur in different areas of the world.

The deep convective systems play a fundamental role in atmospheric circulation and climate. Thunderstorms and meso-scale convective systems (including tropical cyclones) produce fast vertical transport, redistributing water vapor and trace gases and influencing the thermal structure of the UTLS (Bath et al., 2002; Sherwood et al., 2003; Kim, 2005; Ray and Rosenlof, 2007; Cairo et al., 2008; Fueglistaler et al., 2009; Romps and Kuang, 2009; Chae et al., 2011). Measurements of atmospheric parameters such as temperature and water vapor with high vertical resolution and accuracy near the tropopause altitudes is difficult, especially during severe weather events, and the processes that determine the details of the UTLS structure needs to be deepened (Forster and Shine, 1999, Pommereau and Held, 2007). Hydration and dehydration of the UTLS are also poorly understood, different models and measurements show that overshooting convection can penetrate the

tropopause and, with different mechanisms, either hydrate or dehydrate the UT or the LS (Kley et al., 1982; Danielsen, 1993; Wang, 2003; Corti et al., 2008).
The ongoing satellite missions do not provide suitable time/space coverage to study such kind of phenomena with adequate horizontal and vertical resolution and sensitivity. The in situ measurements are too sparse and the acquisitions at the UTLS altitudes are always difficult and often not reliable.
The determination of the convective systems cloud top height is also important to understand the climate changes and to improve the climate modeling which are affected by the radiative interaction between the clouds, the surface and the atmosphere. The same type of clouds located at different altitudes can affect the atmospheric radiative budget in a completely different way. The Intergovernamental Panel on Climate Changes (IPCC) has identified the clouds as one of the most important issues influencing the climate changes and it is still the less understood giving the highest error to the radiative forcing (IPCC, 2001).
Some clouds, like cirrus, are really difficult to detect due to their low optical thickness, but their impact on the climate warming is really high. It has been demonstrated that cirrus can lead to positive or negative radiative heating rate depending on the altitude, the optical depth and their location with respect to underlying clouds (Hartmann et al., 2001).
Many studies have been conducted to determine the altitude of the cloud top, using satellite instruments and different techniques. Some techniques rely on the infrared brightness temperature measurements providing a high temporal resolution, but not accurate vertical resolution (King et al., 1992; Platnick et al., 2003). Some other technique uses the lidar to detect the attenuated backscatter, like the Cloud-Aerosol Lidar and Infrared Pathfinder Satellite Observation (CALIPSO) providing really high vertical resolution, but poor temporal resolution and coverage (Minnis et al., 2008).
A recent study (Chae et al., 2011) uses satellite measurements to study the effects of tropical convective clouds on the thermal structure and hydration of the UTLS highlighting the cooling that corresponds to the cloud top and the warming above that.

2.2 The stability of the atmosphere

Much of this paragraph is from Seinfeld and Pandis (2006) and references therein.
An air parcel moving in the atmosphere without exchanging any heat with the surroundings is called adiabatic air parcel. When it rises the surrounding pressure is lower and lower and consequently it expands and consumes energy, that results in expansion and cooling (the opposite happens if the air parcel sinks). The change in energy due to the expansion work is equal to the energy reduction due to the temperature decrease.

Denoting with T the temperature, z the height and c the heat capacity at constant pressure per unit mass of air and using the first law of thermodynamics and the law of ideal gas then

$$\Gamma = \frac{dT}{dz} = \frac{g}{c} \tag{2.1}$$

is the dry adiabatic lapse rate. The vertical gradient for a neutral atmosphere is constant since g/c is constant (c=1005 $JKg^{-1}K^{-1}$).
Γ is 9.76 K/km and given the surface temperature To, the profile temperature is

$$T = To - \Gamma z. \tag{2.2}$$

In the case of not dry air, the heat capacity at constant pressure is higher. In general the value of c depends on the water vapor mixing ratio content. If w_v is the water vapor mixing ratio in the air parcel, then

$$c_p = (1 - w_v) \cdot c_{p,air} + w_v \cdot c_{p,wv} \tag{2.3}$$

So the higher is the water vapor content, the larger is heat capacity of the air parcel, and the smaller is the adiabatic lapse rate, this implies that the presence of a cloud in the atmosphere can change the temperature profile.
If an air parcel containing water vapor rises, its temperature decreases and its relative humidity increases. When the relative humidity exceeds the 100%, the condensation take place and some latent heat is realized. In this case part of the cooling due to the rising parcel is replaced by the heating due to the condensation and the lapse rate is lower than the dry adiabatic lapse rate, this is called moist adiabatic lapse rate.
If we note as ΔH_v the latent heat of water evaporation per gram, then the moist adiabatic lapse rate is

$$\Gamma_s = \frac{g}{c_{p,air}} + \Delta H_v \cdot \frac{dw_v}{dT} \tag{2.4}$$

So the moist lapse rate strongly depends on the temperature.
In general an air parcel moving in the atmosphere is not subject to adiabatic environment alone but to different processes too, creating a non-adiabatic environment with a different lapse rate that we can denote as Λ. In this case the temperature profile becomes

$T_a(z)=To-\Lambda z$ (2.5)

If ρ is the density of the air parcel and ρ_a is the density of the surrounding atmosphere, the acceleration experienced by the air parcel is proportional to the density difference as

$$a = g \cdot \frac{(\rho - \rho_a)}{\rho} \tag{2.6}$$

so, if the density of the air parcel is lower than the surrounding, it will rise.
Given the ideal gas law (since the air parcel and the surrounding has the same pressure)

$$a = g \cdot \frac{(T - T_a)}{T} \tag{2.7}$$

which can be written as

$$a = g \cdot \left[\left(\frac{T_a(z)}{T_0} \right)^{\left(\frac{\Gamma}{\Lambda}\right)-1} - 1 \right] \tag{2.8}$$

if $\Lambda>\Gamma$ then $a>0$, so the air parcel rises and accelerates providing instability in the atmosphere. The opposite happens if $\Lambda< \Gamma$: in this case $a<0$, the acceleration is negative, so the parcel decelerates until it stops and the atmosphere becomes stable.
By comparing the environmental lapse rate with the adiabatic one we have 3 different regimes of stability in case of clear sky conditions:

$\Lambda > \Gamma$ unstable
$\Lambda = \Gamma$ neutral
$\Lambda < \Gamma$ stable

In the first case the air parcel is warmer than the surroundings and it rises, so the atmosphere is unstable and the temperature decreases more quickly with the altitude. This occurs when there is a warming of the surface air or a cooling of the air at a certain height (radiative cooling of clouds).
In the second case the atmospheric lapse rate is adiabatic and the air parcel is in equilibrium.
In the third case the air parcel cools more quickly than the environment so it is heavier and it leads to the stability.

In case of cloudy conditions we should compare Λ with the moist adiabatic lapse rate Γ_s obtaining the following 3 regimes:

$\Lambda > \Gamma$	absolutely unstable atmosphere
$\Gamma > \Lambda > \Gamma_s$	conditionally stable atmosphere
$\Gamma_s > \Lambda$	absolutely stable atmosphere

The first case is already discussed, since $\Gamma > \Gamma_s$ then $\Lambda > \Gamma_s$. The same holds for the third case.
Regarding the conditionally stable atmosphere, the stability depends on the saturation of the rising parcel. If the air parcel is not saturated, the dry adiabatic lapse rate is the reference and the atmosphere is stable. Whenever the air parcel is saturated then the moist adiabatic lapse rate is the reference and the atmosphere is unstable. Thus a cloudy atmosphere is less stable then a dry atmosphere with the same lapse rate.

Accordingly with the theory described above, Danielsen (1982) defined a process for stratospheric anvil formation during convective systems: when an air parcel ascends it cools by expansion and the water vapor condenses. The heat released by the condensations reduces the lapse rate. Positive buoyancy accelerates the parcel up to the maximum velocity until the equilibrium level, where the buoyancy becomes negative, the parcel decelerates and then it stops. When the parcel rises, the air above is also accelerated and it forms a cloud turret as a stratospheric overshooting. By entraining and mixing with the warmer stratospheric air, the temperature in the turret increases and the maximum height decreases. The turret collapses and the still ascending air diverges horizontally forming the anvil cloud in the stratosphere. The temperature profile in the anvil should approach the adiabatic gradient (9.76K per km). The predicted profile would include 2 minima, the lower one corresponding to the standard tropopause altitude and the higher one corresponding to the top of the anvil (Figure 2.1)

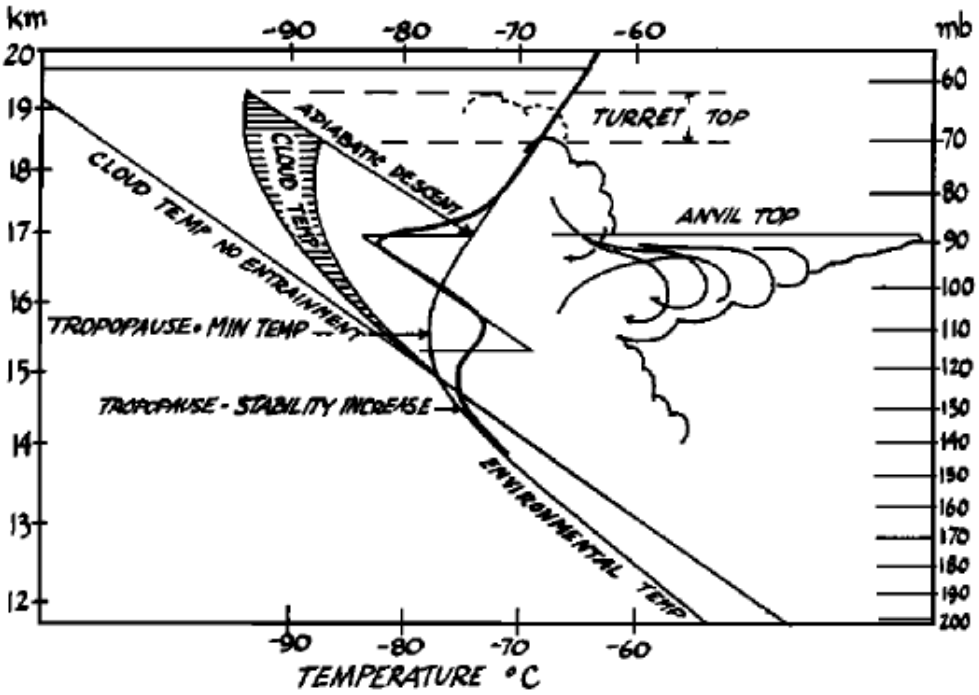

Figure 2.1: Anvil formation in the UTLS due the collapsing turrets and the corresponding double temperature minima. Cartoon from Danielsen (1982).

The mixture of tropospheric and stratospheric air in the anvil hydrates or dehydrates the UTLS depending on the difference between the water vapor mix ratio of the anvil χ_v and that one of the surrounding stratospheric background χ_{vs}. If $\chi_v > \chi_{vs}$, the ice crystals evaporate hydrating the stratospheric air. On the other hand if the radiative effect of the anvil clouds is also considered, there is heating at the base due to the warmer troposphere below and cooling at the top. This, in turn, produces turbulence and instability inside the anvil itself and it keeps the anvil stirred. This process moves the water vapor upward producing larger ice crystals at the top, which are heavier and so they fall down dehydrating that area.

2.3 The water vapor in the Upper Troposphere Lower Stratosphere

Foster and Shine (1999, 2002) have shown the large potential impact of the water vapor on the climate changes by addressing the increase of water vapor in the UTLS in the period 1980-1999 as the cause of the enhancement of climate forcing by 40% compared to the forcing due to the CO_2 alone. However an unexpected decrease of stratospheric water vapor (around 10%) has been documented after year 2000 (Randel et al., 2006) and Solomon et al., (2010) confirmed its impact on the climate changes. They show that such decrease in water vapor slow down the rising rate of global surface

temperatures by about 25% compared with the expected rate calculated from the well-mixed greenhouse gases.

Several recent trends have been reported in the tropopause region. Globally the lower stratospheric temperature was 1.5 K lower in the last decade than in the 1960's (Ramaswamy et al., 2006). Average trends from radiosonde data are -0.5 ± 0.16 K/decade for the period 1979-2008. However, differences of 0.1 K/decade are found between datasets, and satellite-based data show less cooling than radiosondes (Peterson and Baringer, 2009).

The increase in stratospheric water vapor is capable of causing a radiative forcing of up to 0.29 W m^{-2} and a cooling of more than 0.8 K in the lower stratosphere over the past 20 years of the last century (Forster and Shine 2002). Stratospheric water vapor plays a role in the formation of tropical ultrathin cirrus clouds, which, in turn, contribute to the global warming due to their albedo (Luo et al., 2003; Peter et al., 2003; Dessler et al., 2003; Liu et al., 2007; Haladay et al., 2009). However the water vapor is also important for chemistry of the UTLS (Hofmann et al., 1992; Shindell et al., 2001; Rohs et al., 2006; IPCC report AR4, 2007; Tian et al., 2009; Flury et al., 2009), in fact it is the source of the hydroxyl radical (OH) in both the troposphere and the stratosphere. OH is of direct importance in many chemical cycles in both regions (Brasseur et al., 1984; Wayne et al., 1985).

HO_2 radicals take part in important catalytic cycles which regulate the production and destruction of ozone in both the troposphere and stratosphere (Wennberg et al., 1994). A stratospheric water vapor increase leads to an increase of OH concentration, which results primarily in an enhanced ozone depletion by the HO_x-cycle. A long-term growth in stratospheric water vapor affects the heterogeneous ozone destruction (ClO_x-cycle) within the Antarctic polar vortex which is caused by an enhanced formation of polar stratospheric clouds (PSCs) (Stenke et al., 2004).

OH also controls the oxidizing capacity of the atmosphere for short-lived gases, and regulates the lifetime of the longer-lived species such as CO and CH_4. Oxidation of methane may represent a minor water vapor source in the lower stratosphere, oxidation of each CH_4 molecule in the lower and mid stratosphere creates about 2 H_2O molecules (Jones et al., 1986). The tropical stratospheric water vapor is then transported poleward by the midlatitude "pumps" so that the middle and higher latitudes are basically a water vapor sink. Based on chemical transport model studies, the radiative forcing from the increase in stratospheric water vapor due to oxidation of CH_4 is estimated to be +0.07 (± 0.05) W m^{-2}, with a low level of scientific understanding (Forster et al., 2002).

H_2O is also involved in heterogeneous chemistry in the lower stratosphere. Stratospheric water vapor can modify the formation of liquid and solid aerosol particles while heterogeneous chemical reaction rates depend on the aqueous content of liquid aerosols. It is clear that the distribution of water substance in the UTLS region has significant

impact on the global climate process. In order to assess the impact of water vapor, we need to understand how it is transported in the stratosphere. There are only two known sources for stratospheric water vapor: photochemical CH_4 oxidation (Brasseur et al., 1984; Letexier et al., 1988) and the overshooting from deep convective clouds. The main source of lower stratospheric water vapor is the deep tropical convective clouds that pump water vapor from the troposphere to the stratosphere (Holton et al., 1995).

2.4 The GPS radio occultation technique and the International Space Station

The Global Positioning System (GPS) Radio Occultation (RO) technique (Kursinki et al., 1997) enables measurement of atmospheric density structure with a global coverage (Figure 2.2), in any meteorological condition (since the radiowave signal is not affected by clouds) and with high accuracy and precision (Kuo et al., 2005). According to Kuo (2004) the RO soundings have the highest accuracy between 5 and 25 km of altitude with observational errors (including measurement and representativeness errors) in the range 0.3%-0.5% in refractivity.

Several GPS RO missions are working at present, providing a high density of vertical profiles with a good time and space coverage of the Earth, like the Constellation Observing System for Meteorology, Ionosphere and Climate (COSMIC) six-satellite constellation (Anthes et al., 2008), and the Gravity Recovery And Climate Experiment (GRACE) twin satellites (Beyerle et al., 2005), and several new missions are planned for the near future (e.g. COSMIC2, ACES, MetOp-B and ROSA on SAC-D).

The use of the GPS RO has improved the weather forecast especially in remote areas of the globe where there are no other instruments available, with high vertical resolution: it has been shown that the tropical cyclone (TC) track forecast became much more precise using these acquisitions (Huang et al, 2004) and the ECMWF forecast has also been improved especially in the UTLS thank to the RO vertical resolution (Cardinali, 2009).

The GPS RO bending angle is the primary product of the GPS RO measurements and it is much more sensitive to the atmospheric variations than any other RO product since it is not affected by any elaboration and any assumption. The temperature and the water vapor profiles, as secondary products, are retrieved assimilating the European Centre for Medium-Range Weather Forecasts (ECMWF) model analysis. The use of this model and the coarse vertical resolution of the assimilated data, can influence the retrieved RO profile especially in rare cases, like during tropical cyclones (TCs), where many acquisitions are rejected from ECMWF. The sensitivity of the bending angle to the variation of atmospheric density and the high vertical resolution of the GPS RO

technique, are able to provide accurate and detailed information regarding the top of the storms (Biondi et al., 2011c).
Figure 2.2 shows the monthly latitudinal distribution of COSMIC ROs. It is clear that the coverage is really good at the mid-latitudes (between ±27 and ±60 degrees), but it definitely drops between the tropics, which is the most important area for the study of the convective systems.

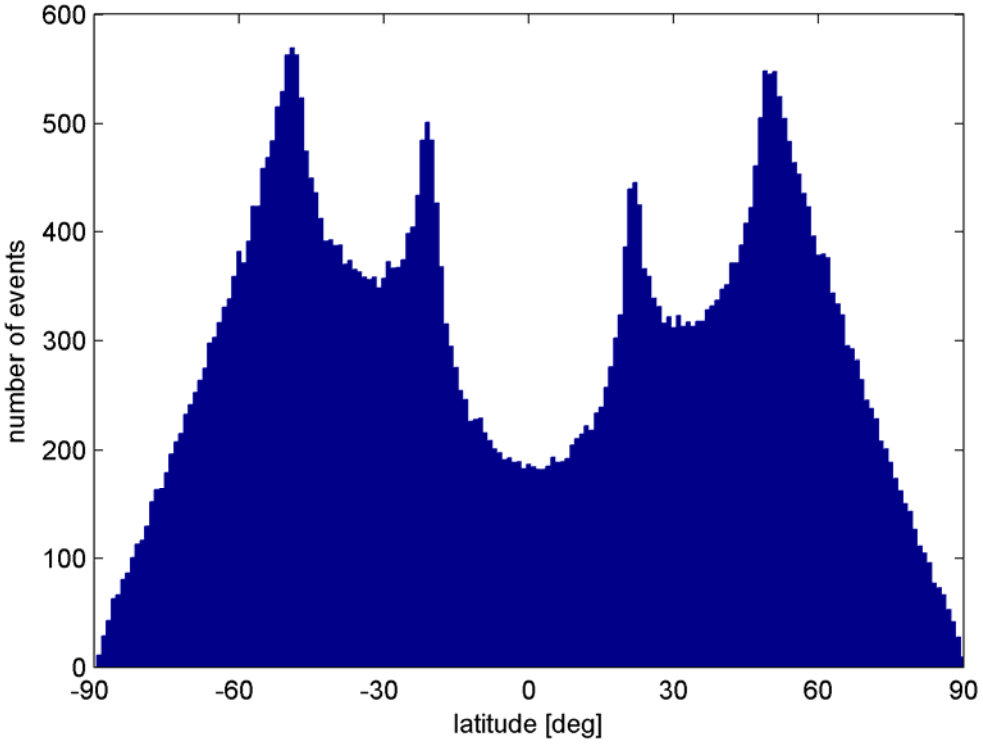

Figure 2.2: COSMIC monthly latitudinal radio occultation distribution with 1 degree resolution. Image from Biondi et al. (2011b).

In 2015 the Atomic Clock Ensemble in Space (ACES) (Svehla et al., 2006) will be launched on board of the International Space Station (ISS). ACES is also equipped with an advanced GPS RO receiver and it will be able to increase the number of RO acquisitions in the tropical area by 32%, contributing to enhance the study of the convective systems. We show in Figure 2.3 the simulated monthly latitudinal distribution of ACES ROs, the average number of occultation between ±15 degrees is 65 which is about one third of the number of COSMIC occultation (208) in the same area.

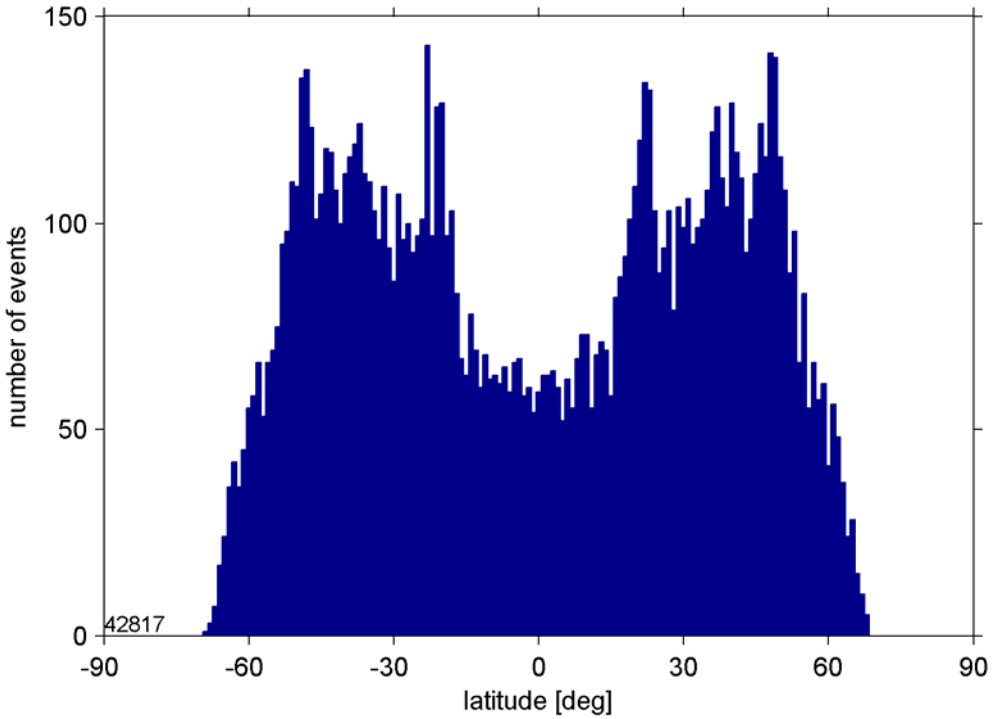

Figure 2.3: ACES simulated monthly latitudinal radio occultation distribution with 1 degree resolution. Image from Biondi et al. (2011b).

Chapter 3

Data description

3.1 The convective systems and the tropical cyclones

The Convective Systems (CSs) information comes from the International Satellite Cloud Climatology Project (ISCCP) Deep Convection Tracking Database with a nominal time resolution of 3h. This is a database created to identify and describe the properties of meso-scale deep convective cloud systems (Rossow et al., 1999) using brightness temperatures from geostationary satellite measurements. The CSs are identified by cloud top temperatures < 245 K, the Convective Clusters (CCs) are also detected as adjacent cloudy pixels with cloud top temperatures < 220 K. The CSs represent all high-level cloud systems, including isolated cirrus, deep convective towers, and anvil clouds. The dataset provides information related to location, size, shape and the properties of the clouds, including CCs when they are present, their location and properties.

We collected the tropical cyclone tracks, commonly defined "tropical cyclone best tracks" (Figure 3.1), from different institutes, each responsible of a different ocean basin: US National Hurricane Center (Atlantic, Caribbean, Gulf of Mexico and Eastern Pacific), Australian Government Bureau of Meteorology (Western, Northern, Eastern Australia), Japan Meteorological Agency (Western, Northern Pacific), Météo France (Southwest Indian Basin) and Unysis Weather (North Indian Ocean Basin, Bay of Bengal and Arabian Sea). They are post-cyclone analyses providing accurate information supported by the use of in situ and satellite based instruments. Any institute provides the data in a different format, so we have created a new database with a standard format for all the tropical cyclones information (including tropical depression, tropical storm and extra-tropical cyclone), adding, when it was possible, some other information provided by other sources. The best track provides information at least every 6h including the name, dates, coordinates, intensity (the maximum mean sustained 10-meter wind speed in a time range depending on the agency, usually between 1 and 10 minutes), and minimum pressure of the tropical cyclone. In some cases, during the Hurricane Hunters missions or specific campaigns, additional information is available, such as eye dimension, moving cyclone direction and speed.

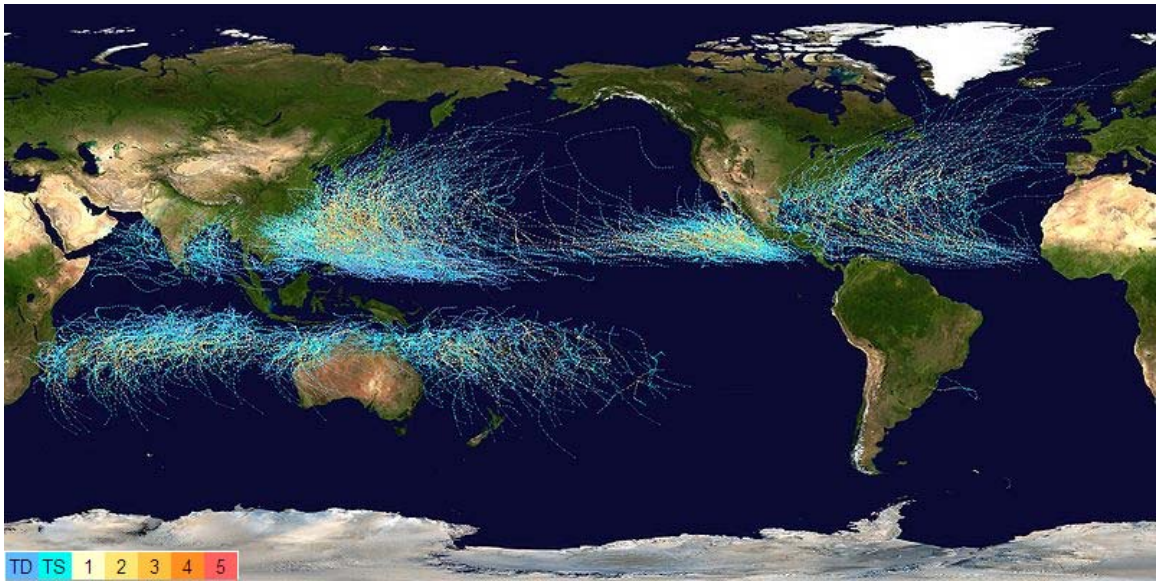

Figure 3.1: The tropical cyclones best tracks distribution from 1985 to 2005 (image from Wikipedia). The colors indicate the intensity of the cyclone from Tropical Depression (TD) status (in blue) to Tropical Cyclone (TC) category 5 (in red).

3.2 Satellite data

The satellite data are the main database used for this work. We analyzed the acquisitions from the GPS receivers in order to build an algorithm to detect the storm cloud top and to analyze the UTLS vertical cross section of the convective systems (in term of atmospheric density, water vapor and temperature). We used the data from the meteorological geostationary satellites to detect possible overshooting and to verify the location of the GPS profiles into the convective system. The advantages of the meteorological satellites are the high temporal resolution and global coverage, but they are not able to profile the atmosphere. CALIPSO instead, has an extremely high vertical resolution, but very low temporal resolution, so it indeed provides the best measurements to validate the storm cloud top when it is co-located with the GPS ROs. We want to demonstrate that the GPS could combine a good coverage of the globe with the high vertical resolution, providing a unique dataset.

3.2.1 The GPS radio occultations data

We downloaded The GPS ROs from the COSMIC Data Analysis and Archive Center (CDAAC) website (http://cosmic-io.cosmic.ucar.edu/cdaac/index.html). We collected all the level 2 product profiles in Network Common Data Form (NetCDF) format covering the period 1995-2009 coming from the missions: the Global Positioning System/Meteorology (GPS/MET, 1995-1997) satellite (Rocken et al., 1997), the

CHAllenging Minisatellite Payload (CHAMP, 2001-2008), (Wickert et al., 2001), the Satellite de Aplicaciones Cientificas-C (SAC-C, 2000-2001) (Hajj et al., 2004), the COSMIC (2006-2009) six-satellite constellation and the GRACE (2007-2009) satellite. All the products are provided in a common standard format:

- Atmospheric Profile (atmPrf), which is a product containing the bending angle, refractivity, impact parameter and the so called dry pressure and dry temperature (because derived assuming no water vapor). All the parameters are reported versus the geometric height above the mean sea level and the coordinates of the perigee point with really high vertical resolution, from 60 meters in the low troposphere to 1.5 km in the stratosphere (Kuo et al., 2004);
- Wet Profile (wetPrf), which is an interpolated product sampled every 100 meters and obtained using 1DVar (one dimensional variational) technique (Biondi et al., 2011b) together with ECMWF low resolution analysis data. This profile contains latitude and longitude of the perigee point, pressure, temperature, water vapor pressure, refractivity and mean sea level altitude of the perigee point;
- European Centre for Medium-Range Weather Forecasts (ECMWF) Profile (ecmPrf), which is a low resolution product generated from the ECMWF gridded analysis (ECMWF TOGA 2.5 degree Global Surface and Upper Air Analysis) and co-located with occultation profile for comparison purposes. It contains refractivity, pressure, temperature and moisture profile versus mean sea level altitude and coordinates;
- Radiosonde Profile (sonPrf), which is radiosonde data in FSL (Forecast System Laboratory) format, part of the National Oceanic and Atmospheric Administration Earth System Research Laboratory (NOAA/ESRL) radiosonde database, co-located with the GPS RO in a time window of 6 h and space window of 400 km. It contains latitude, longitude, pressure, temperature, water vapor pressure, refractivity and mean sea level geometric height.

3.2.2 The Cloud-Aerosol Lidar and Infrared Pathfinder Satellite Observation data

Cloud-Aerosol Lidar with Orthogonal Polarization (CALIOP) on board of CALIPSO satellite is a two-wavelength (532 nm, 1064 nm) polarization-sensitive lidar that provides high-resolution vertical profiles of aerosols and clouds (Vaughan et al., 2004; Winker et al., 2007), with footprint of 100 m and horizontal and vertical resolutions depending on the altitude:

- from -2 km to -0.5 km of altitude the horizontal resolution is 333 m and the vertical resolution is 300 m for both channels,

- between -0.5 km to 8.3 km of altitude the horizontal resolution is 333 m and vertical resolution 30 m for the 532 nm channel (vertical resolution for 1064 nm is 60 m),

- between 8.3 km and 20.2 km of altitude the horizontal resolution is 1 km and the vertical resolution is 60 m for both channels

- between 20.2 km and 30.1 km of altitude the horizontal resolution is 1.67 km and the vertical resolution is 180 m for both channels,

- between 30.1 km and 40 km of altitude the horizontal resolution is 5 km and the vertical resolution is 300 m for the 532 nm channel (measurement not available for the 1064 nm channel).

CALIPSO was launched in 2006 and the data are available from June 2006. We used the lidar product level 1 (CAL_LID_L1), release ValStage1 and version V03 to analyze the total attenuated backscatter and to compare it with the cloud altitude retrieved by the GPS ROs. We also have used the ground track coordinate files with 10 seconds temporal resolution to find the ROs co-located with CALIOP cross section profiles.

3.2.3 The geostationary satellites data

The Geostationary Operational Environmental Satellite (GOES) is an American meteorological satellites' pair providing real-time weather data for use in short-term weather forecasting, space environment monitoring, research and development. They are commonly called GOES-East covering the US East Coast and GOES-West covering the US West Coast. One of the instruments on board of the GOES is the Imager (Schmit et al., 2001) measuring the radiance in 5 different channels (frequencies depending on the satellite generation) and the brightness temperatures (BTs) are distributed for any frequency. We have analyzed the BTs near the location of the RO profiles in order to detect the overshooting during the convective systems in the Atlantic and East Pacific basins.

We downloaded from the Comprehensive Large Array Data Stewardship System (CLASS) the GOES VARiable IMaGer data (GVAR_IMG) in "area" format with native spatial resolution acquired by GOES11 and GOES12 at 6.8 microns (band 3), which is sensitive to the water vapor, and the BT at 10.7 microns (band 4).

The Meteorological SATellite 1 (MTSAT-1) images (Puschell et al., 2002) from Japan Meteorological Agency (JMA) and the Geostationary Meteorological Satellite (GMS, known as "Himawari") images from Japan Aerospace Exploration Agency (JAXA) were also used for the same purpose since they provide products similar to GOES.

3.3 In situ measurements

Due to the difficulties to measure atmospheric parameters at the UTLS altitude using the satellite sensors, the acquisition from in situ sensors becomes fundamental to validate the GPS RO profiles. The radiosonde data are well distributed on the land with a good temporal resolution during the severe weather (6 hours), but their water vapor

measurements in the UTLS are not reliable due to the (limited) accuracy of the instruments (Miloshevich et al., 2006) and besides they are not available on the ocean. We used the temperature profile acquired with radiosonde to validate the ones retrieved from the co-located GPS ROs.
The airborne data are the best way to acquire accurate and precise information on the UTLS, however we can get a limited amount of those data only during campaigns which are really expensive. Neverthelles those data are extremely important to validate other acquisitions and to get a clear knowledge of the dynamics of the convective systems from an "inside" point of view.
The lightning data are a good proxy for the convection, but the coverage of the lightning detection network is limited to a few hundred kilometers from the sensor.

3.3.1 The radiosondes data

The radiosondes (RAOBs) are units suspended to a weather balloons filled of hydrogen or helium, measuring atmospheric parameters such as pressure, temperature, relative humidity and wind (some of them are also able to measure radiation and ozone). The units are also equipped with a GPS receiver which allows us to know the actual coordinates of any acquisition and they transmit all the data to the ground station via radio frequency signal ranging from 1675 to 1685 MHz. The RAOB can reach altitudes above 30 km, the diameter of the balloon when released is about 2 meters, but it expands reaching higher altitudes (since the surrounding pressure decreases) and it bursts when the diameter is between 6 and 8 meters.
There are more than 800 stations all over the world providing two acquisitions each day at the same time (00.00 and 12.00 UTC) and in case of severe weather the frequency of the acquisition is increased to 1 every 6 hours.
The RAOB dataset used in this work are in FSL (Forecast System Laboratory) format, and they are part of the National Oceanic and Atmospheric Administration Earth System Research Laboratory (NOAA-ESRL) radiosonde database. They provide the time of report in UTC, the latitude and longitude of the station together with the profiles of temperature, dew point temperature, wind direction and wind speed at each pressure level. The pressure levels are then converted in geopotential height using an algorithm (Durre et al., 2006).

3.3.2 The airborne data

The field campaigns, so far, are the principal way to get clear and detailed information on the UTLS structure, especially during convective systems, when many remote sensing techniques are of difficult implementation. In cloudy conditions there is no any other method equally effective than aircraft and balloon in getting measurements

with the same vertical resolution of the ROs. We use for our studies 3 different instruments on board of the Russian stratospheric aircraft Geophysica M55 (Borrmann, 1995), the Multiwavelength Aerosol Scatterometer (MAS) (Adriani et al., 1999), the Fast In-Situ Hygrometer (FISH) (Zoger et al., 1999) and the Fluorescent Airborne Stratospheric Hygrometer (FLASH) (Yushkov et al., 2000), and an instrument on board of the American aircraft ER-2, the Cloud Physics Lidar (CPL) (McGill et al., 2002).

- MAS uses 3 laser diodes as a light source at 680, 780, and 830 nm and it is able to measure the scattering and depolarization of aerosols and clouds. The atmospheric particles backscatter part of the light back to the MAS and, in case the particles do not have spherical shapes, part of that light is depolarized.
- FISH is a hygrometer based on the Lyman alpha photofragment fluorescenctee technique, it is able to measure the total water (gas phase and ice particles) at stratospheric conditions with at least 5% precision (0.2 ppmv) with time integration of 1 second (Schiller et al, 2009). It can be mounted on aircraft and on balloon: it can resolve horizontal structures of the H_2O mixing ratio of 200 m.
- FLASH is also a Lyman alpha hygrometer measuring water vapor (just gas phase) with accuracy of 4% in the range between 3 and 100 ppmv. The measurement precision is 5.5%, with time integration of 4 seconds at stratospheric conditions. The total uncertainty of the measurement is less than 10% at stratospheric mixing ratios greater than 3 ppmv, increasing to about 20% at mixing ratios less than 3 ppmv.
- CPL is a 3 wavelengths laser working at 355, 532 and 1064 nm. CPL is able to profile clouds with 30 m of vertical resolution and 200 m horizontal resolution providing information about the optical depth, depolarization ratio and particles size.

3.3.2 The World Wide Lightning Location Network data

The World Wide Lighting Location Network (WWLLN) is a network of about 40 sensors (updated to 2009) spread all around the world, able to locate the lightning strokes with high accuracy (1-2 km), but with an efficiency of approximately 30% to detect strokes of 30 kA (Rodger et al., 2005). A single sensor cannot locate the strokes, for this reason it is important to use a network providing the Time Of Group Arrival (TOGA) of the very low frequency (VLF) radiation (3−30 kHz) from the stroke. At least 5 WWLLN detections are requested to unambiguously locate the stroke. The sensors can be located thousands of km away from the stroke, but typically just 15% to 30% of the strokes detected from one sensor are also detected from other 4 or more and they are the strongest ones. Any receiving station acquires and processes the dispersed sferic waveform determining the TOGA from the progression of phase versus frequency using the whole wave train (Dowden et al., 2002). The station consists of an electric field whip antenna, a processing computer and an internet connection to send TOGA to the main

elaboration center. The coverage of this system is obviously limited and influenced from the distribution of the sensors; there are areas well covered and areas with missing acquisitions, like Africa. We used for this work, data from 2006 (28 stations available) to 2008 (32 stations available).

3.4 Models

3.4.1 The ECMWF re-analyses

We used for this work the ECMWF TOGA 2.5 degree Global Surface and Upper Air Analysis which is a dataset containing uninitialised analysis values interpolated to a 2.5° x 2.5° regular latitude/longitude grid. The surface dataset available from January 1985 contains surface pressure, surface temperature level1, mean sea level pressure, u- and v-components of wind at 10 m, temperature at 2 m, dewpoint at 2 m, surface geopotential and land-sea mask. The upper air dataset (available from April 1999 in this format and from January 1985 with coarser vertical resolution) contains 21 standard pressure levels, temperature, vertical velocity, u- and v-components of horizontal wind, and relative humidity at each level. The data are provided by CDAAC website in netCDF format.

3.4.2 The Cloud Model 1

The Cloud Model 1 (CM1) is a three-dimensional, non-hydrostatic, non-linear, time-dependent numerical model suitable for idealized studies of atmospheric phenomena (http://www.mmm.ucar.edu/people/bryan/cm1/). This model is specifically realized to study meso-scale processes in the atmosphere, like thunderstorms and tropical cyclones. Its governing equations conserve total mass in a moist atmosphere and retains several terms in the internal energy equation as terms associated with the heat content of hydrometeors, and dissipative heating (Bryan and Fritsch, 2002; Bryan and Rotunno 2009). CM1 is also able to simulate all the processes in a very large domain with high vertical and horizontal resolution and to use several equation sets, for different applications. The user can choose to get the output in netCDF, HDF or GRID format and to get the output in a single big file or to split it in several files depending on the time resolution. One important feature provided together with the code is the possibility to use pre-configured input settings like supercell, squall line, 3D hurricane, axisymmetric hurricane, and nonhydrostatic gravity waves, allowing the user to get confidence with the code and to play with it.

Chapter 4

Methodology

4.1 The GPS radio occultation technique

The GPS RO technique involves two different satellites to measure the density of the atmosphere. The signal transmitted by the GPS satellite (GPS 24 satellites network and potentially all the future missions listed in the section 6.3) is received from a Low Earth Orbit (LEO) satellite which measures the propagation delay and the intensity of the signal. This technique allows us to retrieve profiles of atmospheric parameters, such as refractivity, temperature, water vapor and pressure with extremely high vertical resolution.

The radio occultation technique uses the phase and amplitude of two L-band signals (L1 at 1575.42MHz and L2 at 1227.60MHz) transmitted from GPS satellites and received by the GPS receivers on board of LEO satellites (e.g. COSMIC). When the signal passes through the atmosphere it is refracted due to the different density and it can be characterized by three parameters: the bending angle α, the impact parameter a and the tangent radius r_p (Figure 4.1). The retrieval of the atmospheric parameters (such as temperature, pressure and water vapor) from the GPS signal can be obtained in 9 steps detailed by Kuo (2004):

1) *Detection of L1 tracking error*: when the distance between the Earth´s limb and the receiver is large enough, the fractional variation of the Doppler frequency shift of the RO signal is smaller than the fractional variation of the refractivity, this introduces significant error in the final product. The L1 Doppler frequency shift is modeled with respect to the position and the velocity of the GPS satellite, the LEO and the climatological refractivity (Sokolovskiy, 2001) and then it is compared with the measured values. If the difference exceeds the threshold defined by the algorithm, the RO signal is truncated.
2) *Filtering the noise of L1 and L2*: the raw signals are affected by noise that could cause a bending angle coming from a multi-valued function of the impact parameter, so the noise is filtered before computing the bending angle and the impact parameter.
3) *Estimation of the occultation point*: the occultation point is the projection on the Earth surface of the tangent point connecting the GPS satellite to the LEO. This is defined as the occultation point corresponding to the L1 excess phase of 500m.

4) *Change of reference*: the oblateness of the Earth introduces significative errors in evaluating the inverse problem under spherical symmetry (Syndergaard, 1998). Thus, the reference center is moved from the real Earth center to the virtual center assigned to the occultation.
5) *Computation of bending angles*: in absence of water vapor (high troposphere and above) the multipath is rare and the bending angle is directly calculated from the Doppler frequency shift. In the moist atmosphere the multipath propagation requires more complex techniques like radioholographic algorithms (Gorbunov and Gurvich, 2000; Sokolovskiy, 2001; Gorbunov, 2002; Jensen et al., 2003) and the heuristic method proposed by Beyerle et al. (2004). Above 13 km of altitude the L2 signal is not taken in to account. The bending angles computed in the moist and dry atmosphere are then combined giving the final profile.
6) *Ionospheric calibration of the bending angle*: a linear combination of L1 and L2 bending angles acquired at the same impact parameter, provides the calibration. At the altitudes where the L2 signal is usable, the L1 signal is corrected using the L1-L2 bending angle computed from above.
7) *Optimal estimation of bending angle*: the noise affecting the bending angle is roughly constant at all the altitudes also after filtering and ionospheric calibration. The magnitude of the bending angle instead decreases exponentially with altitude creating problems in the measurements at high elevations. For this reason the bending angle observation at high altitudes is replaced by the first guess model, having smaller error.
8) *Retrieval of refractivity through Abel inversion*: under local spherical symmetry conditions the refractive index n can be derived from α, a and r_p using the Abel inversion (Fjeldbo et al., 1971):

$$n(r_p) = \exp\left(\frac{1}{\pi} \int_{a_{r_p}}^{\infty} \frac{\alpha(a)}{\sqrt{a^2 - a_{r_p}^2}} da \right) \tag{4.1}$$

where $a_{r_p} = n(r_p) \cdot r_p$ is the impact parameter of the ray with radius r_p.

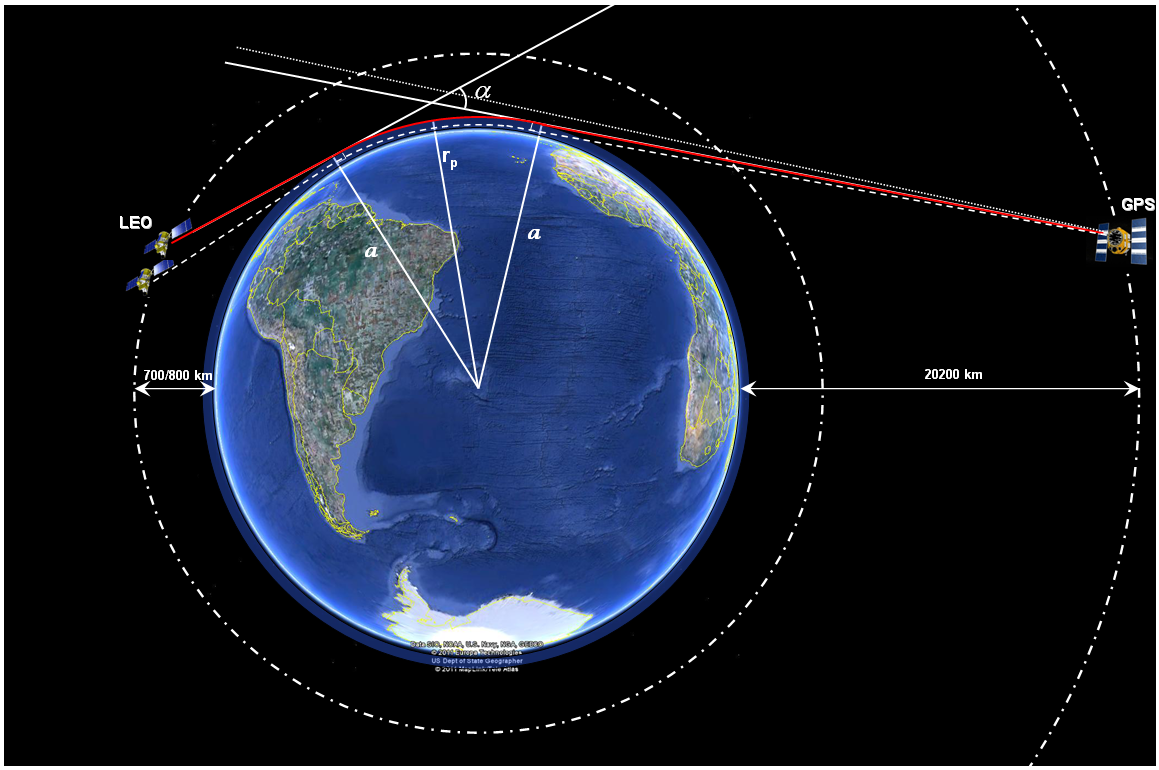

Figure 4.1: The GPS RO technique scheme (the proportions are not respected). Dash and dot lines are the satellite orbits (LEO and GPS). The dot line is the signal transmitted from GPS not crossing the atmosphere. The red and dash line are two different signals bended by the atmosphere and received from the LEO satellite. With respect to the red signal, α is the bending angle, a is impact parameter and r_p the tangent radius.

The refractivity profile is then

$$N = (n-1)\cdot 10^6 \tag{4.2}$$

9) *Retrieval of temperature, pressure and water vapor*: assimilating the refractivity together with the ECMWF model, with a one-dimensional variational (1DVar) method, it is possible to retrieve the temperature (T in Kelvin), pressure (p in millibar) and water vapor pressure (e in millibar) profiles which are basically consistent with the refractivity (N) according to the equation

$$N = 77.6\frac{p}{T} + 3.73\cdot 10^5 \frac{e}{T^2} \tag{4.3}$$

4.2 The bending angle anomaly technique

Using all the GPS ROs collected from the CDAAC website from 1995 to 2009, we have created a grid with one-degree resolution containing the averaged bending angle profiles (from the atmPrf product) and the averaged temperature profiles (from the wetPrf product). This grid becomes our reference and is defined in the text as "climatology".
In figure 4.2 we show the map with the number of occultations used for any box.

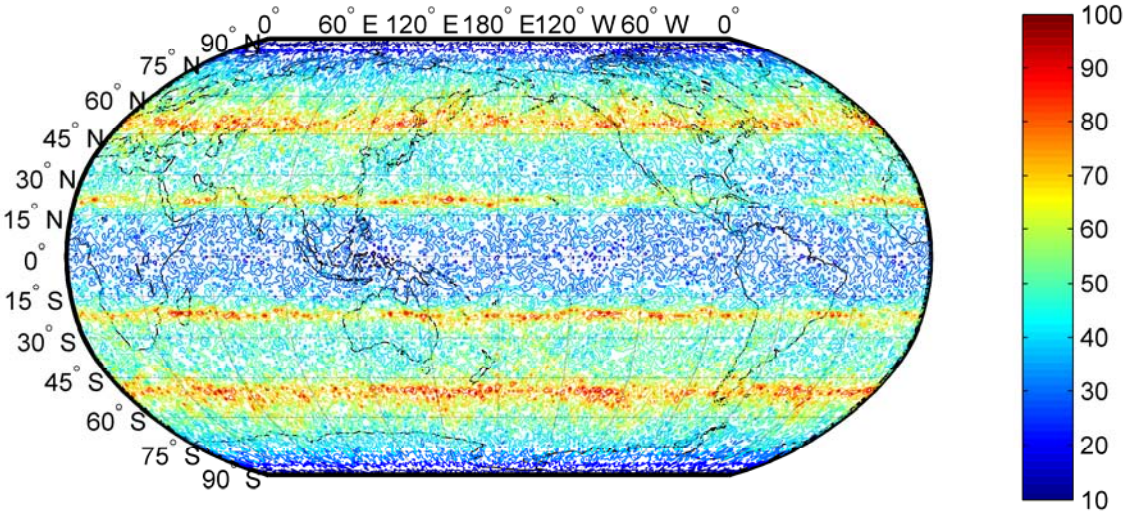

Figure 4.2: GPS RO coverage using one degree latitude/longitude resolution.

Comparing the actual profiles during the storm with the climatology, we have obtained the anomaly which is the primary parameter used in this work. The full process to compute the anomaly fundamentally consists in 4 steps:

- *Interpolation*. The vertical distribution of atmPrf acquisitions is not fixed, providing anytime a different number of measurements in the same altitude range. To create a standard reference to be comparable with other products, we decided to interpolate the atmPrf data with a common vertical resolution of 50 meters.
- *Geo-location*. The interpolated profiles where indexed with respect to the tangent point latitude and longitude at 16 km of altitude (average altitude of the tropical tropopause) with one-degree resolution.
- *Average*. In each geo-located box, we averaged all the values at the same altitude obtaining one reference profile for every Latitude/Longitude degree with 50 meters vertical resolution: this becomes the climatological reference ("climatology") for the corresponding coordinates.
- *Anomaly computation*. For the bending angle we computed the percentage anomaly with respect to the climatology as shown in the Eq. (4):

$$\alpha_{anomaly} = 100 \cdot \frac{\alpha_{Storm} - \alpha_{C\lim}}{\alpha_{C\lim}} \quad (4)$$

where α_{Storm} is the bending angle profile during the storm and α_{Clim} is the climatological bending angle from the gridded reference.

For the temperature, since the real value of the temperature variation is an important parameter to be evaluated, we simply computed the temperature difference as shown in the Eq. (5):

$$T_{anomaly} = (T_{Storm} - T_{C\lim}) \quad (5)$$

where T_{Storm} is the temperature profile during the storm and T_{Clim} is the climatological temperature from the gridded reference.

We decided to use as reference a full-dataset climatology (instead of seasonal or monthly) since in certain areas the number of samples is too small to represent a standard atmospheric trend. The monthly mean in the area of the storm is sometimes the result of the average of only a few ROs, and we would not be able to argue that the anomalies are statistical significant on such a basis. However, our studies show that the anomalies behavior is the same using as reference, either the full-dataset mean, the mean of one year of data or the monthly mean, or just the anomaly amplitude changes. Figure 4.3 shows the averaged bending angle anomaly profile (versus altitude from the ground up to 20 kilometers above mean sea level) computed for all the ROs co-located with the TCs best tracks using as reference different climatological datasets.

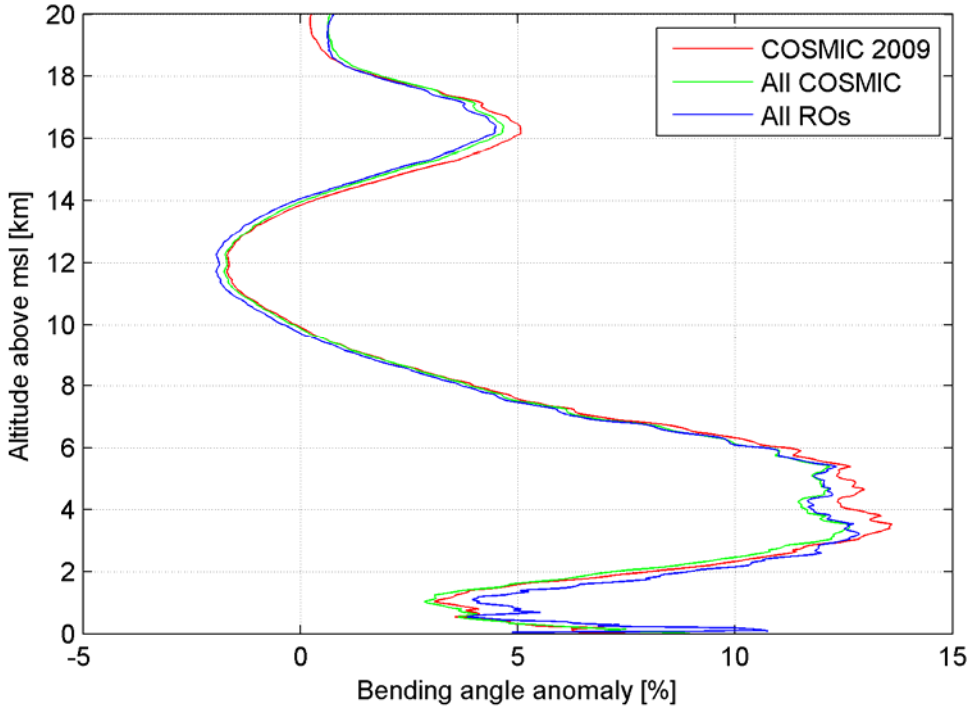

Figure 4.3: Averaged bending angle anomaly during tropical cyclones using different climatologies as reference. The blue line is the averaged anomaly referenced to the full climatology, the green line is the same anomaly using as reference the climatology of all the COSMIC data from 2006 to 2009 and the red line is the anomaly using as reference the climatology of 2009 COSMIC data.

The red profile is obtained using climatology coming from the COSMIC dataset of 2009, the green profile is obtained using a climatology from all the COSMIC data (2006-2009) and the blue using all the available ROs (from GPS-Met, SAC-C, CHAMP, GRACE and COSMIC). The trend is the same for all the 3 profiles. One year of data (2009) is probably not enough to provide a solid background, but increasing the number of samples (green and blue lines) the profile seems to become stable.
In Figure 4.4 we compare the bending angle anomaly for a specific case during a TC (Bertha 2008, described in the section 5.2.1) when using annual climatology as reference (green profile) and monthly climatology (dark green) as reference. Also in this case the trend is the same, but the amplitude is slightly different.

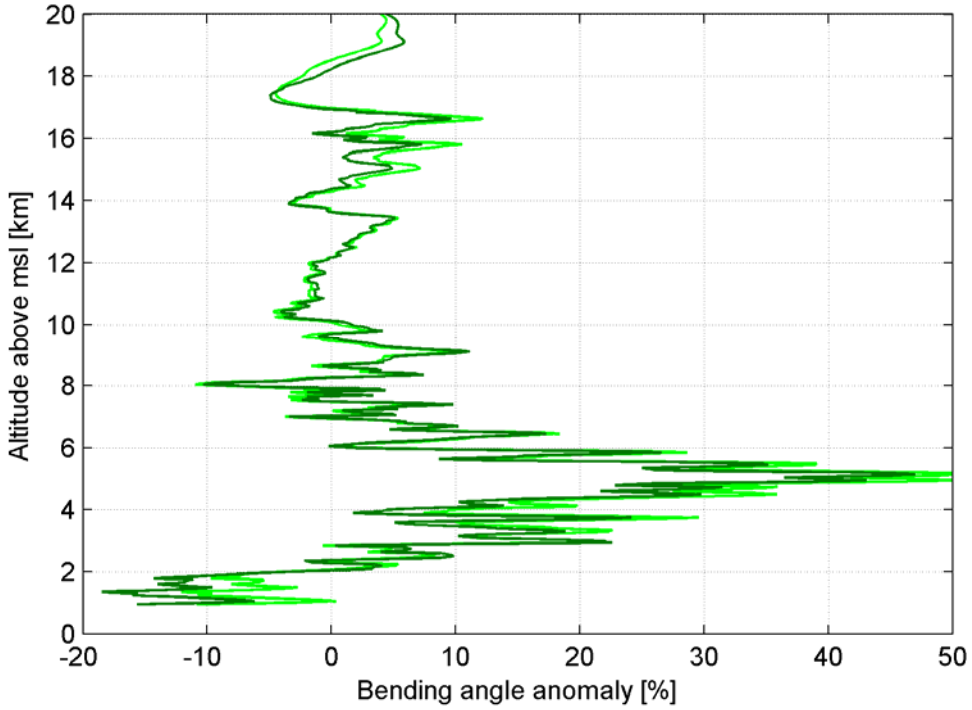

Figure 4.4: Bending angle anomaly using as reference the annual climatology (green) compared to the bending angle anomaly using as reference the monthly climatology (dark green).

4.3 Cloud top detection algorithm

The criteria to select ROs into the TCs or into the CSs were slightly different due to the available information coming from different datasets and due to their different structure and lifetime.

Comparing the coordinates of the TC best tracks with the RO tangent point coordinates at 16 km of altitude, we selected 1194 profiles in a time window of 3 hours and a space window of 300 km from the center of the storm in the period 1995-2009.

Comparing the ISCCP Deep Convection Tracking Database with the RO tangent point coordinates at 16 km of altitude, we have selected 2157 cases in a time window of 2 hours and within the actual radius of the CC in the period 2006-2008.

The reason because we use as reference the coordinates at 16 km of altitude, is that we focus our study on the UTLS and a RO profile tangent points can span a couple of hundred kilometers from the surface to the top. The time window is shorter for convective systems because of their smaller dimension than TCs and shorter lifetime.

Each time a storm is present, it influences the UTLS modifying the bending angle behaviour (Biondi et al., 2011a). The $\alpha_{Anomaly}$ shows at least one positive spike in the

UTLS during severe storms. In case of one single spike, the algorithm assumes the cloud top to be at the same altitude as the maximum amplitude of the spike, in case of multiple spikes the cloud top is supposed to be at the altitude of the lowest spike. We will call RO_{ctop} the cloud top altitude determined with this algorithm.
Most of the time a $\alpha_{Anomaly}$ trend corresponds to an opposite $T_{Anomaly}$ trend (positive $\alpha_{Anomaly}$ spike corresponds to negative $T_{Anomaly}$ spike) and in principle in these cases it should be possible to identify the storms just by looking at the $T_{Anomaly}$. However, the bending angle is much more sensitive than the temperature since it is the first product coming out from the GPS RO measurements and not affected by any elaboration and any assumption. As already described in this section, the temperature profile is retrieved assimilating ECMWF model analysis and this can influence the profile especially in rare cases like during the tropical cyclones and in the UTLS, where the vertical resolution of the assimilated data is quite coarse. For these reasons we prefer to use the $\alpha_{Anomaly}$ to detect the cloud top, rather than the $T_{Anomaly}$.

4.4 Validation of the technique

All the selected cases were compared with the CALIPSO ground track coordinate files to find RO profiles co-located with CALIOP vertical cross section attenuated backscatter, this allowed us to get an independent validation of the effectiveness of our algorithm.
We used the GOES data to monitor the position of the radio occultation, the CALIPSO track and the RAOB relative to the position of the storm. We also used GOES BTs and the WWLLN data as further proxy of convection.
In clear sky conditions and low level clouds, the BT in the water vapor channel is lower than the BT in the 11 microns channel, in case of high clouds the reverse is true and the 6.8 microns BT becomes larger by a few degrees (Schmetz et al., 1997; Chaboureau et al., 2007). In this way GOES measurements were extremely important to detect overshooting in the North American area. Unfortunately in the Asian area just the raster images of the BTs acquired by GMS and MTSAT-1 are available online and just a roughly evaluation of the BT inversion was possible on this study.
Moreover, due to the friction between the particles, the number of lightnings during the convection increases especially during the intensification of the cyclone (Molinari and Idone, 1999) and the lightning stroke rate is correlated with the strength of the system (Williams, 1992), so the high number of strokes identifies a strong convective system. During TCs the number of strokes is definitely lower than the other convective systems (Molinari, 1994 and 1999) and they are mostly located in the eyewall and in the rain-

bands just before the intensification of the cyclone (Molinari and Idone, 1999; Squires, 2008; Solorzano et al., 2010).

The CM1 was used to verify the TC thermal structure and its dependency on the radiative scheme.

We finally used co-located temperature and water vapor profiles (from aircraft and balloon) together with particle detectors (lidar and scatterometer) to validate the CSs structure obtained using the GPS ROs.

Chapter 5

Data analysis

5.1 The GPS radio occultation parameters and sensitivity

As already discussed in the paragraph 4.1, the GPS RO signal allows to measure the bending angle, the refractivity is retrieved using the Abel inversion and the temperature, pressure and water vapor are obtained assimilating the model. This procedure creates errors especially in the evaluation of secondary products such as temperature and water vapor, thus, before using them an analysis of uncertainties and sensitivity is required.

The GPS RO vertical resolution is higher than RAOB and models vertical resolution, so the comparisons between profiles should be done carefully avoiding interpolation of lower resolution data to higher resolution (since they could introduce small scale features). The down sampling of GPS RO profiles is a better solution but it could also introduce aliasing errors. In this work has been decided to compare the acquisitions at the same altitude when available otherwise to downscale the ROs (Kuo et al., 2004).
The GPS RO provides profiles with respect to the altitude, and not with respect to the pressure. Thus, comparisons with data provided as function of the pressure could introduce error since the measurements (estimations) at the same altitudes could be different than measurements (estimations) at the same pressure surface (Kuo et al., 2004).
From the eq. (4.3) it is clear how the refractivity is function of the temperature and the water vapor pressure. The variation of each parameter contributes to a different amount of refractivity variation and these contributions are difficult to be separated. In general we can assume that errors in water vapor pressure mostly contribute to refractivity errors in the lower troposphere (and moist regions, e.g. tropics) and the errors in temperature mostly contribute to refractivity errors in the UTLS (and dry regions, e.g. poles). The propagation of refractivity error into the temperature and water vapor pressure estimates can be evaluated just assuming correct the other parameter:

- By assuming the water vapor being correct, an error of 1% in refractivity corresponds to about 2 K error in temperature in the UTLS increasing to 2.5/3 K in the lower troposphere;
- By assuming the temperature being correct, an error of 1% in refractivity corresponds to about 1 mb error in water vapor pressure in extremely moist lower

troposphere in the tropics, decreasing 0.15 mb at 10 km of altitude and 0.03 mb in the UTLS of a standard atmosphere.

Kuo et al. (2004) have found that the refractivity error can reach 3-4% near the surface at the tropics and between 0.3% and 0.5% in the rest of the troposphere and in the stratosphere. Since the temperature is quite uniform in the lower troposphere, an error of 3-4% in refractivity gives an error of 3-4 mb in water vapor pressure which means an error on relative humidity of 10-13% (since the saturation water vapor pressure is about 30 mb). In the UTLS the water vapor is negligible and a refractivity error of 0.3-0.5% gives an error of 0.6-1 K in temperature.

In figure 5.1 is shown a theoretical refractivity profile during an extreme case of TC. The black line shows the refractivity between the surface and 30 km of altitude computed with the equation (4.3), the green line shows the wet contribution to the total refractivity (second term of eq. (4.3)) and the blue line shows the dry contribution (first term of eq. (4.3)). From this plot it is evident how the contribution of the water vapor (second term of eq. (4.3) and green line of the plot) to the total refractivity is negligible above 9-10 km of altitude confirming the results obtained by Collard and Healy (2003) during a simulation study.

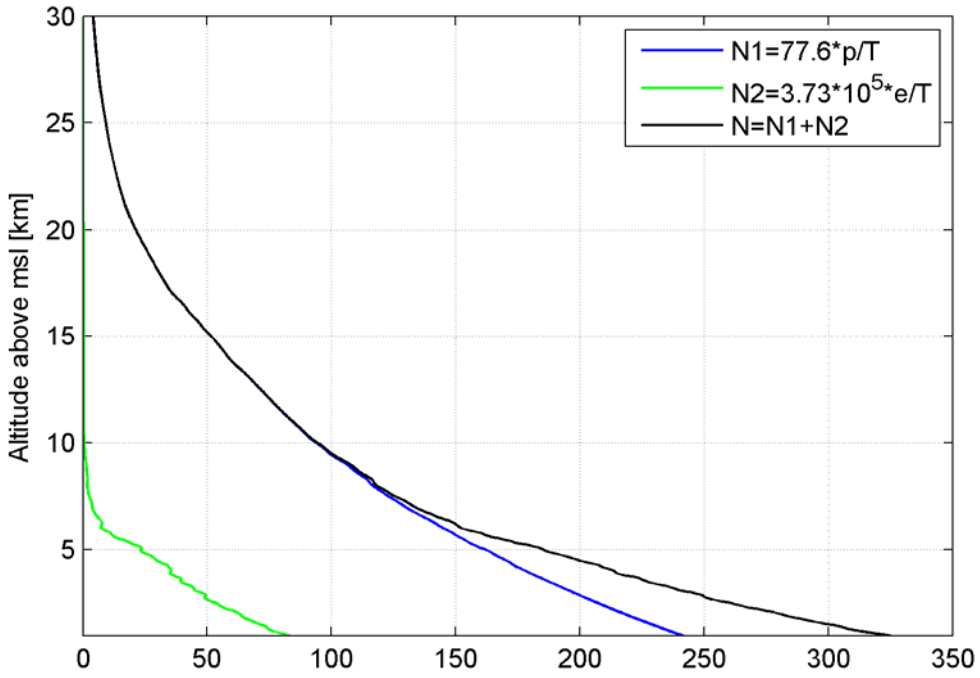

Figure 5.1: Refractivity profile during a TC between the surface and 30 km of altitude, obtained using eq. (4.3) with the temperature, pressure and water vapor pressure value during an extreme case of tropical cyclone category 3. The black line is the total

refractivity, the blue line is the dry refractivity (first term of eq. (4.3)) and the green line is the wet refractivity (second term of eq. (4.3)).

Since the bending angle depends on the derivative of refractivity, in figure 5.2 is reported the sensitivity of refractivity to all the atmospheric parameters using the partial derivative of the eq. (4.3) with respect to the variation of altitude (dh) between 10 and 20 km of altitude. The water vapor pressure contribution (terms dN3/dh and dN4/dh) is absolutely negligible in the UTLS also during extreme events (moving water vapor to higher altitudes). In this specific case above 13 km the refractivity variation is completely due to the temperature variation.

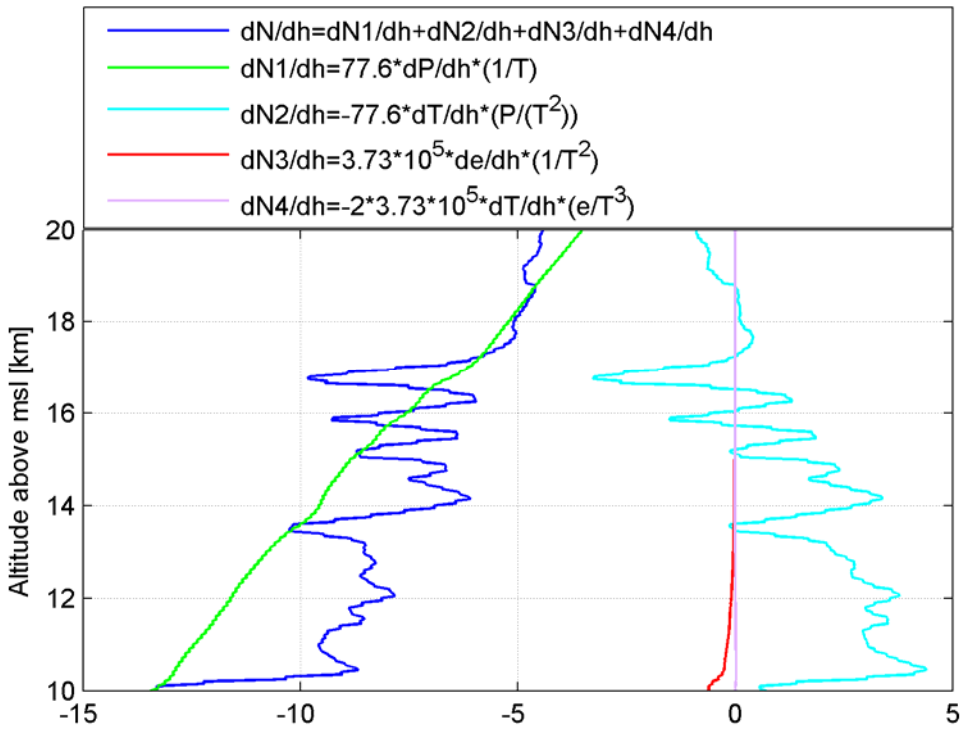

Figure 5.2: Derivative of refractivity (dN) with respect to the altitude variation (dh) in the UTLS (between 10 and 20 km of altitude). The blue line is the sum of all the partial contribution. The green line is the derivative of the first term of eq. (4.3) with respect to the pressure, the cyan line is the derivative of the first term of eq. (4.3) with respect to the temperature, the red line is derivative of the second term of eq. (4.3) with respect to the water vapor pressure and the magenta line is the derivative of the second term of eq. (4.3) with respect to the temperature.

5.2 Tropical cyclones

We started our study, analyzing TCs since a good database was already available from the literature providing all the necessary information on the structure of the systems (as described in the paragraph 3.1) and because the TCs are the strongest convective systems. A disproportionate number of deep convective plumes in a TC may retain the equivalent potential temperature needed to overshoot the tropopause and penetrate deep into the stratosphere. It is already well known that TCs alter the humidity of their local environment (Ray and Rosenlof, 2007). The overshooting clouds in the tropics are usually outside TCs, but there are some areas where overshoots are mostly due to TCs. In general they account for only 7% of the deep convection in the tropics but they contribute 15% of the convection that overshoot the tropopause (Romps et al., 2009). Such TCs increase the water vapor content of the UT (Ray and Rosenlof, 2007) and the integrated water vapor in the vicinity of the storm (Braun et al., 2007). Moreover, they warm the mid troposphere and they cool the tropopause layers (Bath et al., 2002; Sherwood et al., 2003).

The TC best tracks allowed us an easy co-location with the GPS ROs. Comparing the available GPS ROs data from all the missions (GPS-MET, SAC-C, CHAMP, GRACE, COSMIC) with the TC best tracks in a time window of 3 hours and space window of 300 kilometers, we got 1194 profiles (out of more than 2.700.000 ROs measured until 2009), acquired during different stages of the cyclones (tropical depression, tropical storm, cyclone from category 1 to 5 and extra-tropical cyclone) as described in Tables 5.1 and 5.2. More than 70% of the coincidences are coming from COSMIC mission, about 20% from CHAMP, 4% from GRACE, 4% from SAC-C and just 1 profile from GPS-MET. Table 5.3 shows the percentage of RO profiles co-located with tropical cyclone best tracks in different storm stages. This percentage reflects the probability that the cyclone has to get that strength, in fact the most likely status (tropical depression and tropical storm) are represented from a higher number of profiles and the less likely status (Cat. 4 and Cat. 5) are represented by a very little number of profiles.

Mission	Number of RO samples	Number of co-located RO-TC
GPSMET (1995-1997)	5002	1
SACC (2001-2002)	60354	40
CHAMP (2001-2008)	397193	180
COSMIC 2006	249923	179
COSMIC 2007	614201	194
COSMIC 2008	641440	335
COSMIC 2009	644035	211
GRACE (2007-2009)	113567	54

Total	2725715	1194

Table 5.1: Number of radio occultation profiles (second column) available from any mission (first column) and the number of profiles found during the tropical cyclones (third column).

Year	GPSMET	SACC	CHAMP	COSMIC	GRACE	Total
1995	1					1
1996						
1997						
1998						
1999						
2000						
2001		13	9			22
2002		27	28			55
2003			29			29
2004			40			40
2005			33			33
2006			12	179		191
2007			9	194	18	221
2008			20	335	22	377
2009				211	14	225
Total	1	40	180	919	54	1194

Table 5.2: Number of radio occultation profiles co-located with tropical cyclone best tracks for any mission (columns) in any year (rows).

Storm strength	Percentage of co-located ROs [%]
Tropical Depression (TD)	22,11
Tropical Storm (TS)	34,75
Tropical cyclone Category 1 (Cat. 1)	11,11
Tropical cyclone Category 2 (Cat. 2)	8,51
Tropical cyclone Category 3 (Cat. 3)	4,02
Tropical cyclone Category 4 (Cat. 4)	0,47
Tropical cyclone Category 5 (Cat. 5)	3,78
Extra Tropical cyclone (ET)	13,24

Table 5.3: Percentage of radio occultation profiles co-located with tropical cyclone best tracks in different storm stages.

The dataset obtained comparing the TC best tracks with the ROs was also compared with the CALIPSO ground track coordinate files in order to get co-located ROs and CALIOP profiles during TCs. We selected 13 cases (Table 5.4) satisfying this criterion, and so we could perform an extremely detailed analysis of the top structure of the system.
In figure 5.3 is shown the percentage bending angle anomaly trend during the TCs. This plot is the result of averaging all the 1194 TC profiles (green) and it is reported together with the standard deviation of the mean (dark green) to highlight the variability of the parameter. The trend shown in this figure is common to the TCs and the convective systems in general: a positive value of bending angle anomaly in the lower troposphere due to the increase of water vapor evaporating from the surface, a decrease of bending angle anomaly in the mid troposphere reaching negative values between 10 and 14 km of altitude due to the warm core of the TC and again a positive spike in the UTLS due to the extreme cold point that the cyclone produces at the top. While the variation in the lower/mid troposphere (up to 10 km) can be attributed to the combined effect of the temperature and water vapor variation, as addressed in the previous paragraph, above 10 km all the bending angle variation is caused by the temperature variation. In the rest of this thesis, this common trend will be called "TC trend".

Tropical cyclone	Distance [km]	Time distance [min]	Basin
RUMBIA	27	92	West Pacific
ALBERTO	27	119	Atlantic
KRISTY	18	96	East Pacific
PEIPAH	60	7	West Pacific
PABUK	15	52	West Pacific
MAN-YI	92	66	West Pacific
KROSA	18	39	West Pacific
PABUK	79	58	West Pacific
NAKRI	84	85	West Pacific
HANNA	58	37	Atlantic
PHANFONE	20	88	West Pacific
ELIDA	3	102	East Pacific
LOWELL	47	54	East Pacific

Table 5.4: Selected TCs co-located with ROs and CALIPSO track. The second and third columns report the space and time distance between the RO and CALIPSO.

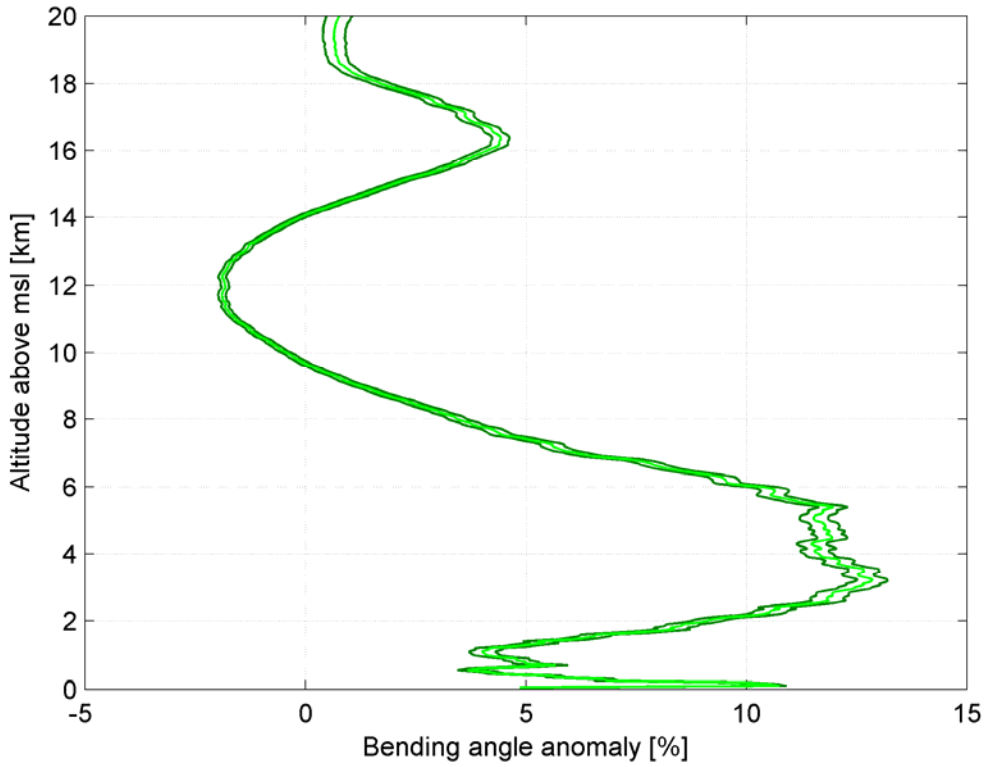

Figure 5.3: Averaged bending angle anomaly during tropical cyclones using all the radio occultation database as climatological reference (green) ± the standard deviation of the mean (dark green). Image from Biondi et al. (2011b).

Before starting a systematic analysis of all the ROs during TCs, we have decided to choose some case study to assess the feasibility of this work.

5.2.1 Case study: Bertha 2008

Bertha 2008 (Figure 5.4) developed from tropical depression on the west coast of Africa near Cape Verde Islands the 3rd of July and in just 6 hours it got the tropical storm strength. For 3 days it moved westward and the strength was almost constant then it reached warmer water and a rapid intensification transformed the storm in a hurricane Cat. 3, with sustained wind of 110 kt. Moving north-west to Bermuda Island, the hurricane gradually weakened to Cat. 2, Cat. 1 and tropical storm. After 5 days moving north-east, a new intensification occurred, the storm became hurricane Cat. 1 for a couple of days, then tropical storm again and finally extra-tropical storm reaching 60 degrees of latitude.

Bertha has been chosen to demonstrate the capabilities of the new technique and to understand what information we can retrieve from the GPS ROs on the UTLS during the storms.

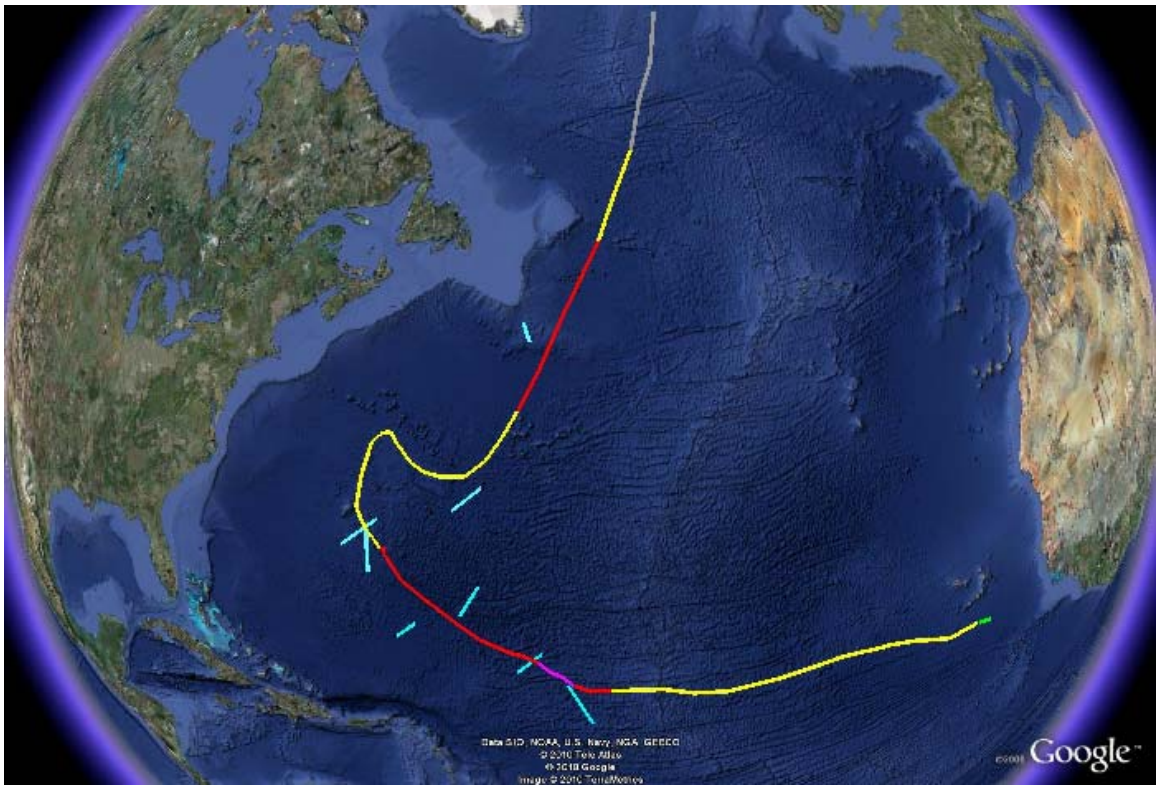

Figure 5.4: Bertha´s track (image from Biondi et al., 2011a). In green the tropical depression status, in yellow the tropical storm status, in red the tropical cyclone status, in magenta the maximum category reached and in grey the extra tropical cyclone status. The cyan lines are the radio occultation tangent points co-located with the hurricane.

Bertha was chosen among more than 100 tropical cyclones for several reasons:

- its track was really long in space (more than 9000 km) and time (19 days including the extra-tropical cyclone status) allowing to get 8 ROs close enough to the center in 4 different status (from tropical storm to Cat. 3 which was the maximum strength),
- Bertha has been in tropical cyclone status for 7 days (from Cat. 1 to Cat. 3) one of the longest periods in the GPS ROs era,
- In the same area there was not any other TC for long time, the previous one was in 2007 an the next one 2 months later, so it is very likely that the UTLS was not influenced by any other strong event for a certain time,

- Bertha passed really close to the Bermuda radiosonde station allowing GPS ROs profiles comparisons with in situ measurements.

Differently from the systematic analyses of all the other ROs cases during TCs (paragraph 4.2), the climatology that we used as reference during Bertha was computed in a different way. To get a more accurate and detailed view of the event, we did not use a reference climatology given by the average of all the RO profiles with 1 degree spatial resolution as described in the section 4.2, but we created a specific climatology with different spatial resolution depending on the dimension of the cyclone, step by step. In case of Bertha the α_{Clim} (eq. (4.4)) and T_{Clim} (eq. (4.5)) were computed averaging the values of all the profiles exactly in the same area covered by the cyclone (not with 1 degree of resolution as described in the paragraph 4.2) which is usually a few square degrees. This approach increases the number of ROs used for the analyses and it allows us to get a sufficient number of samples to study the variation on monthly and seasonal basis. By using all the information available from different satellite sensors (MODIS, GOES), from the US National Hurricane Center best track and from the hurricane hunters, we reconstructed the track of Bertha (Figure 5.5) with the use of the actual cyclone radius and eye radius and we selected all the ROs included in the area within the eye-wall and the outer edge of the cyclone to compute the climatological reference.

By using this procedure, any annual mean was given by the average of almost 200 profiles (the number is mostly depending on the latitude as shown in figure 4.2, and the radius of the cyclone) and the monthly mean is the average of more than 10 profiles at any stage. Figure 4.4 shows the $\alpha_{Anomaly}$ for the case acquired from COSMIC the 8th of July 2008 at 02.01 UTC at 117 km (mean distance of the tangent point) from the center of the cyclone. Bertha was a major hurricane Cat. 3 moving to the north-west (with speed of 10 km per hour), the diameter was about 400 km and the eye diameter was 30 km.

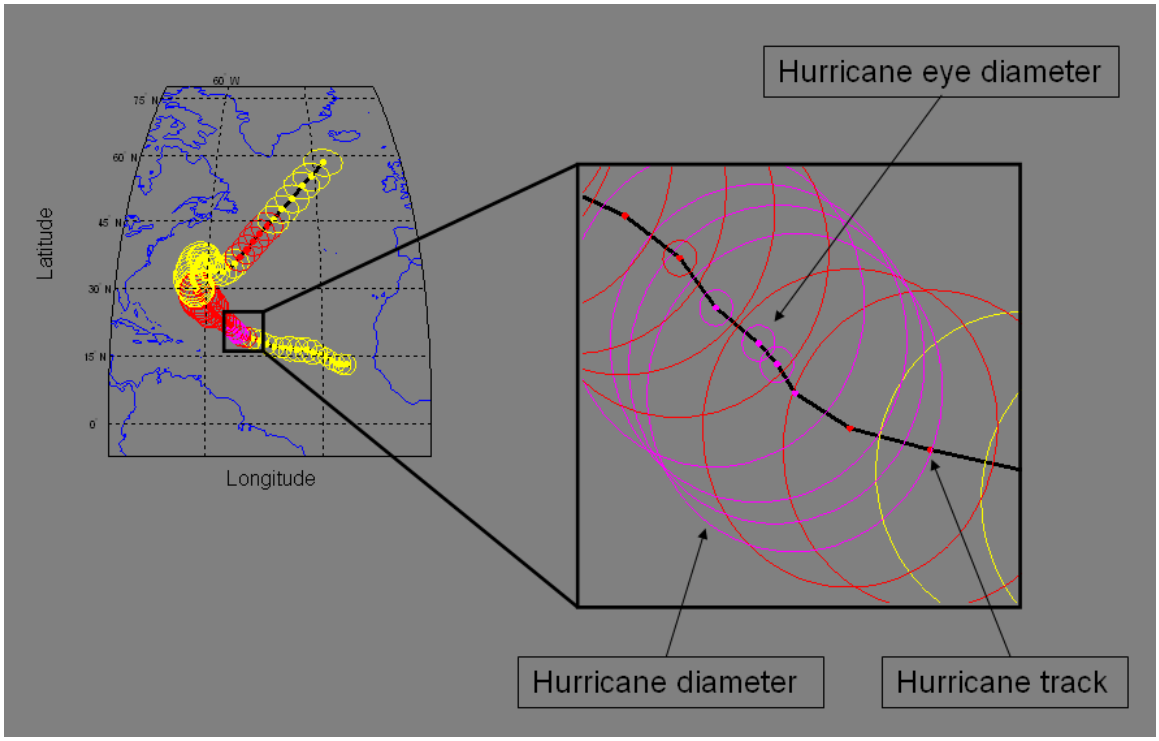

Figure 5.5: Example of Bertha 2008 track reconstruction using different datasets. The different colors represent different status with the same notation of figure 5.4. The zoom shows Bertha when it was major hurricane Cat. 3.

The $\alpha_{Anomaly}$ trend is the characteristic "TC trend", with positive values in the low troposphere, a decrease in the mid-upper troposphere and again an increase in the UTLS. Interesting from figure 4.4, is the comparison of the percentage anomaly using as reference either the annual mean or the monthly mean. The behavior is exactly the same, just the amplitude changes and the anomaly with respect to the monthly mean is slightly "amplified" with respect to the annual mean. Another interesting analysis is shown in figure 5.6, where the same case of Bertha is compared with the monthly anomaly climatologies in the same area (obtained collecting all the ROs, month by month, covered by the hurricane and computing the anomaly with the full dataset as reference). The red profiles are the monthly means during the TC season (May-October in the Atlantic) and the blue profiles are the monthly means during the non TC season (November-April in the Atlantic). It is clear how during the TC season the bending angle anomaly profile is in some way influenced by the convection, it shows the "TC trend", but the amplitude is attenuated with respect to the actual profile of the TC itself (green). During non TC season the behavior is the opposite: negative values in the low troposphere and in the UTLS and slightly positive values in the mid-upper troposphere.

For the same event Figure 5.7 shows the anomaly of all the parameters between the ground and 20 km of altitude from the RO and the co-located ECMWF data. The refractivity (both from RO and ECMWF) shows the "TC trend" as the one from the

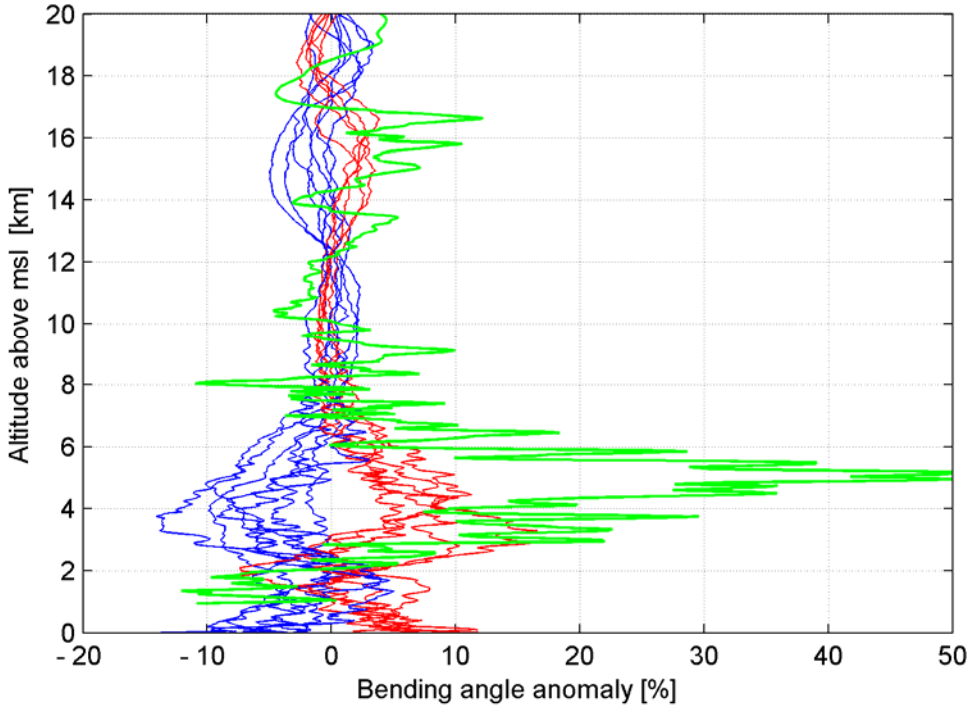

Figure 5.6: In green the bending angle anomaly for the radio occultation acquired from COSMIC the 8th of July 2008 at 02.01 UTC during the hurricane Bertha. In red the monthly bending angle anomaly during the tropical cyclone season (May-October in the Atlantic) in the same area where the COSMIC radio occultation was acquired. In blue the monthly bending angle anomaly during the non-tropical cyclone season (November-April in the Atlantic) in the same area where the COSMIC radio occultation was acquired.

bending angle but the anomaly amplitude is attenuated. According to the eq. (4.3) and discussion of paragraph 5.1, the variation of the refractivity (and the bending angle) is mainly given by the variation of water vapor pressure in the lower troposphere and by the temperature variation in the UTLS. Above 10 km of altitude the temperature anomaly profile from RO is symmetric to the refractivity anomaly (with respect to the zero line), while the water vapor profile from RO is basically following the model.

By going into details of the UTLS and by taking advantage from the Bertha´s track passing next to Bermuda Island RAOB station, it is interesting to compare the GPS RO profile with in situ measurements. In Figure 5.8 is shown the bending angle anomaly profile (green) acquired by COSMIC the 12th of July at 12.47 UTC together with the RO temperature profile (red) and the RAOB temperature profile (blue). The RAOB was launched at 12.00 UTC at a mean distance from the RO tangent point of 170 km. The

$\alpha_{Anomaly}$ from the ground is not shown because it has the typical "TC trend", the study is in this case focused between 13 and 20 km of altitude. The $\alpha_{Anomaly}$ becomes positive just above 13 km and 2 distinct spikes are clear, the lower one at 15.2 km with an amplitude of about 14% and the second one at 17.3 km with an amplitude of about 10%.

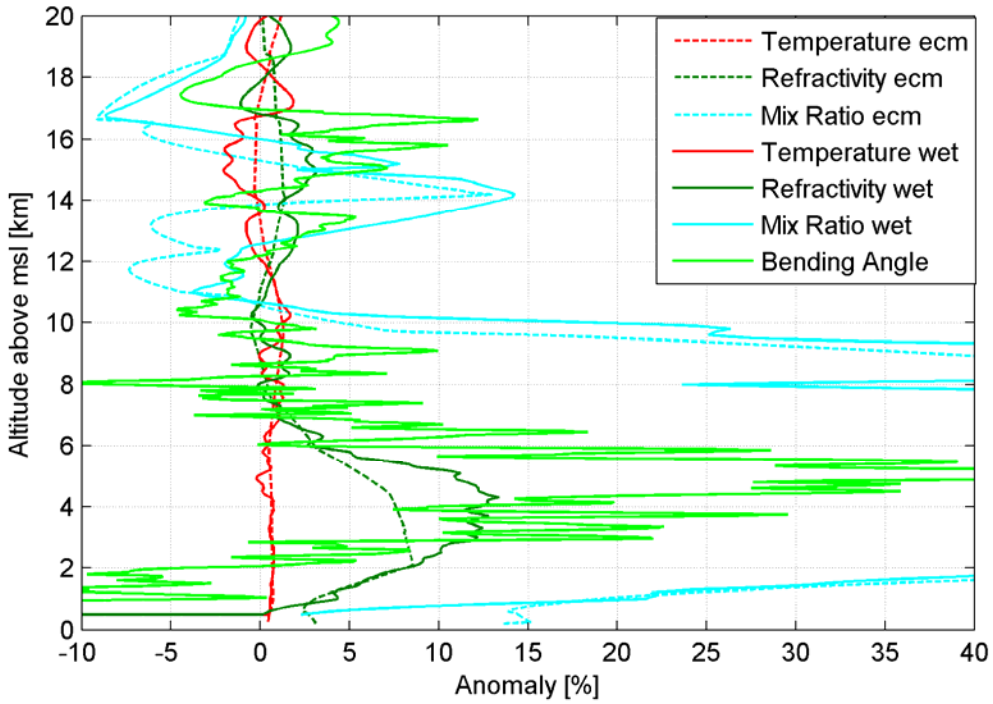

Figure 5.7: In green the bending angle anomaly for the radio occultation acquired from COSMIC the 8th of July 2008 at 2:01 UTC during the hurricane Bertha. In solid dark green, red and cyan respectively the refractivity, the temperature and the water vapor anomaly from RO. In dashed dark green, red and cyan respectively the refractivity, the temperature and the water vapor anomaly from ECMWF model. Image from Biondi et al. (2011a).

Corresponding to the 2 $\alpha_{Anomaly}$ spikes a clear double tropopause is depicted from the RO temperature profile, which is also confirmed by the RAOB. The double tropopause is a feature that we will also find in the next paragraphs characterizing TCs and CSs.
In figure 5.9 we finally plot the $\alpha_{Anomaly}$ computed averaging all the 8 RO profiles acquired during Bertha (green) and the standard deviation of the mean (dark green).

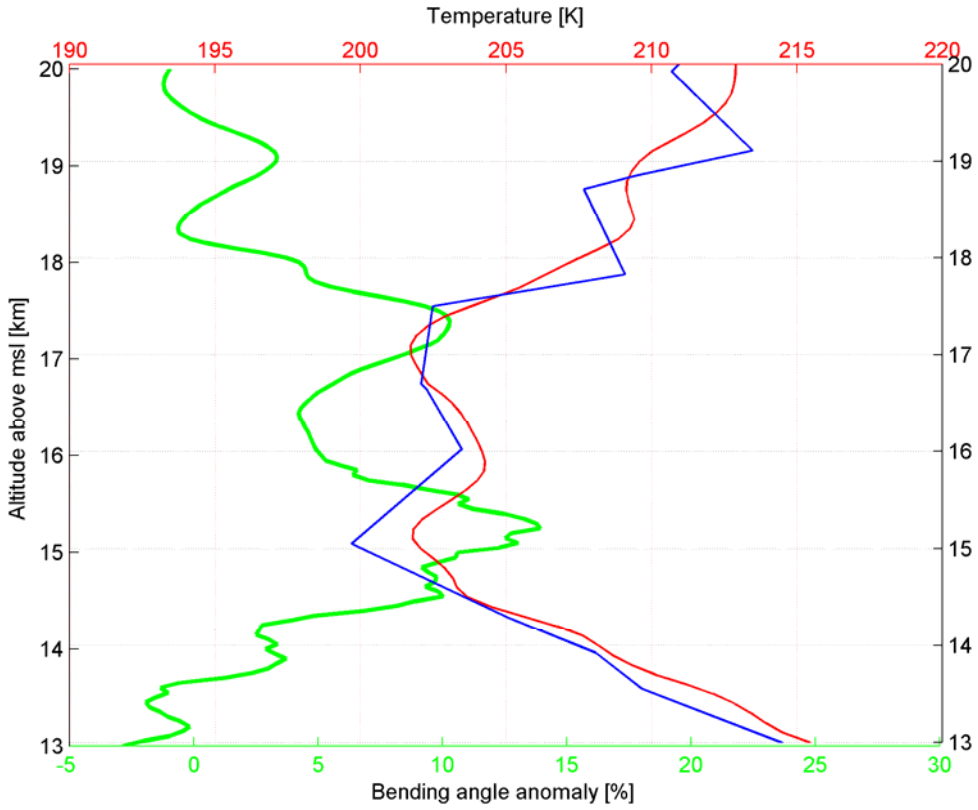

Figure 5.8: In green the bending angle anomaly for the radio occultation acquired from COSMIC the 12th of July at 12.47 UTC during the hurricane Bertha. In red the RO temperature profile and in blue the co-located RAOB temperature profile (Bermuda station). Image from Biondi et al. (2011b).

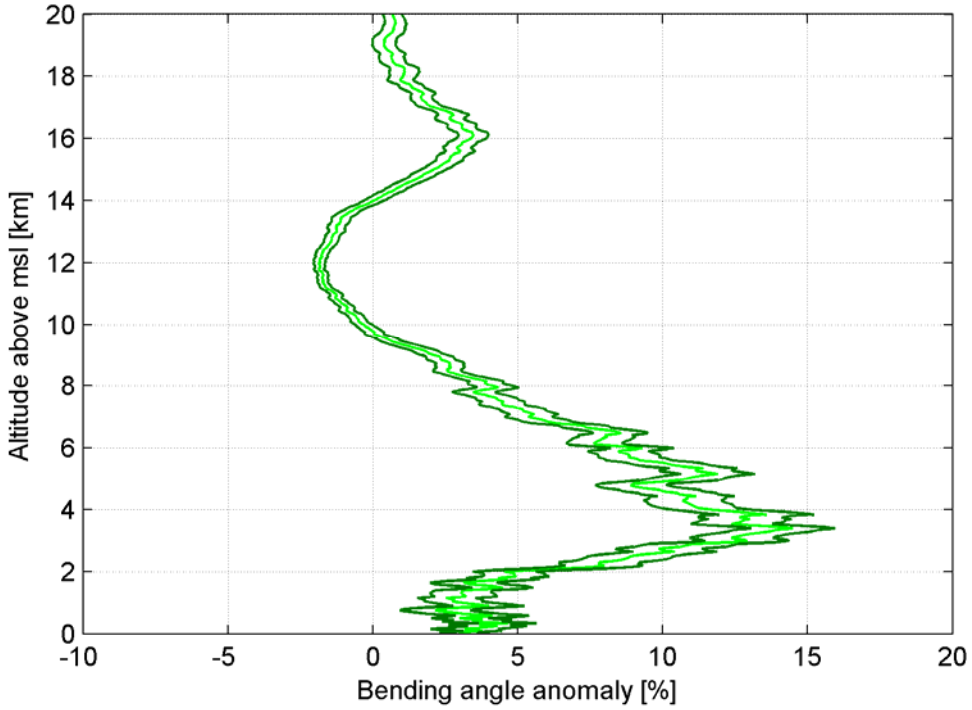

Figure 5.9: Averaged bending angle anomaly (green) during the hurricane Bertha using all the 8 radio occultations co-located with the track ± the standard deviation of the mean (dark green). Image from Biondi et al. (2011a).

5.2.2 Case study: Bill 2009

Bill 2009 track was really similar to Bertha 2008. Bill developed as tropical depression on the west coast of Africa near Cape Verde Islands the 15th of August and it became hurricane in less than 2 days. It remained hurricane for 7 days reaching the maximum strength (Cat.4) the 19th of August with a sustained wind speed of 115 kt. The 22nd of August the hurricane passed over Bermuda Island and it turned to north-east. The 24th it weakened to tropical storm status and became extra-tropical storm until reaching northern Europe.

Figure 5.10 shows the GOES BT in the water vapor channel the 22nd of August when Bill passed over Bermuda Island, the eye was located at 33.0N and 68.5W with maximum sustained wind speed of 90 kt and minimum pressure of 960 hPa weakening from Cat. 3 to Cat. 2. The RO was acquired at 08.27 UTC when Bill was weakening from hurricane Cat. 3 to hurricane Cat. 2. The radiosonde was launched at 11.00 UTC at a distance of about 98 km from the RO tangent point. Figure 5.11 shows the difference of the BT at 6.8 microns and the BT at 10.7 microns from GOES11 at 09.00 UTC exactly in the same region where the RO and the RAOB were acquired. An inversion up to 5 K is recognizable suggesting the presence of overshooting or at least high clouds (see

paragraph 4.4). In this case, as in all the other ones except Bertha, the reference climatology was computed with the methodology described in the paragraph 4.2, with 1 degree spatial resolution. The bending angle anomaly profile, shown in Figure 5.12 depicts the double spike in the UTLS that we also have found during Bertha, in fact we can see that the bending angle anomaly becomes positive above 13 km of altitude, a spike with amplitude of 10% is present just below 17 km and another one at 18.5 km. Similarly to the bending angle anomaly profile, the temperature profile from the RO shows a double tropopause, which is much more pronounced in the RAOB profile.

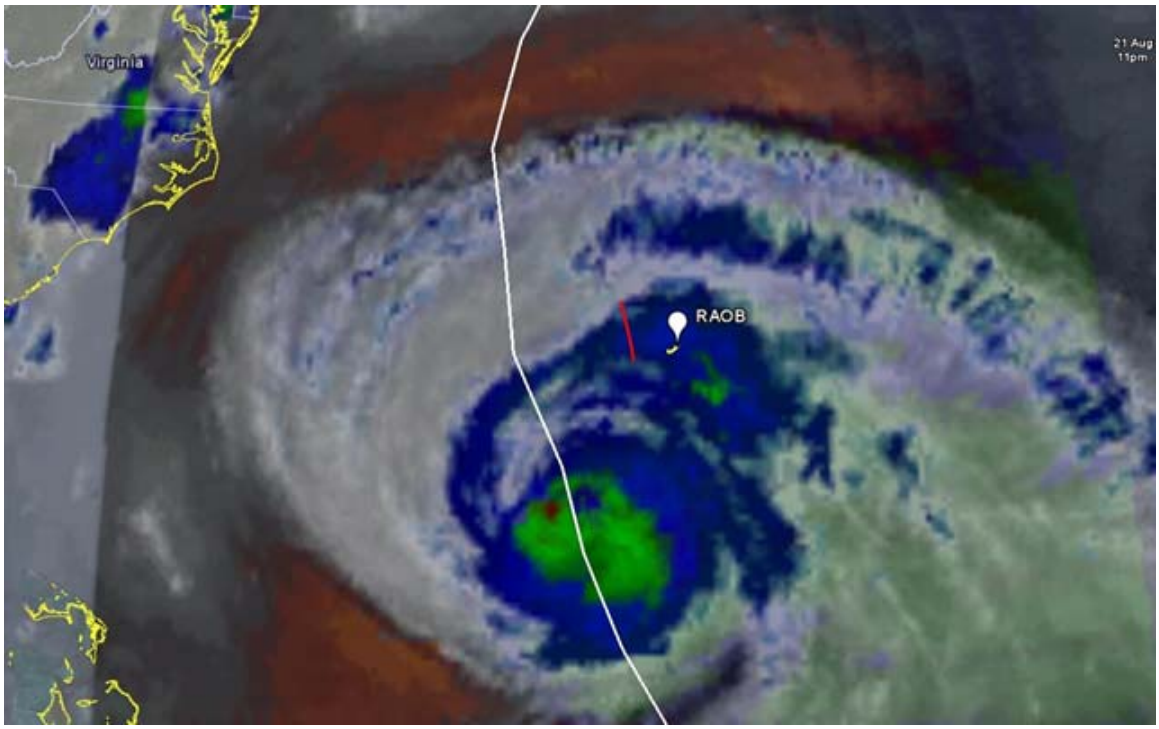

Figure 5.10: Hurricane Bill track (white line) water vapor channel brightness temperature from GOES on 22 August 2009 with the co-located radiosonde (white balloon) and radio occultation (red line). Image from Biondi et al. (2011b).

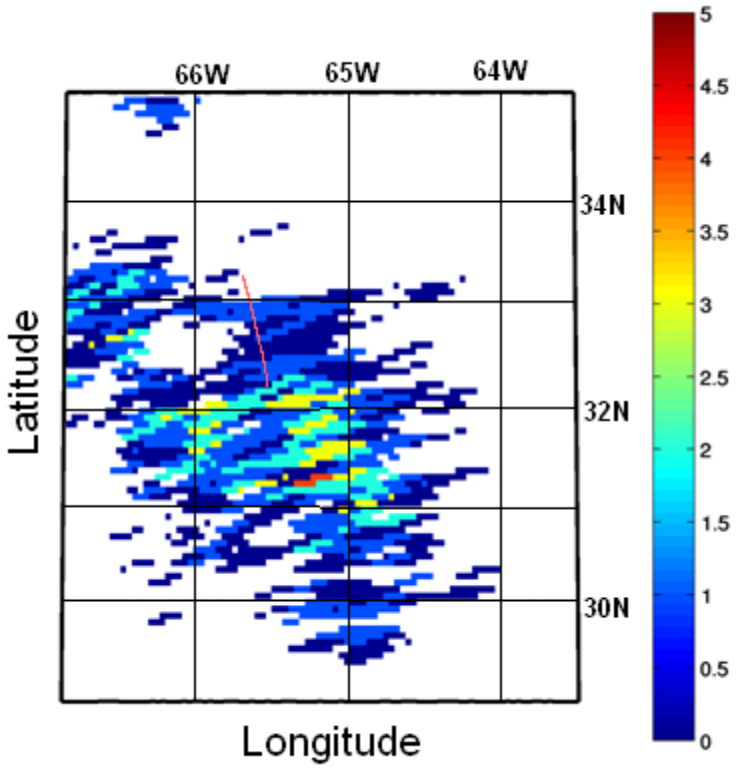

Figure 5.11: Hurricane Bill the 22nd of August 2009 at 08.27 UTC, (Latitude 32,300 and Longitude −65,420): difference between the brightness temperature (in Kelvin) at 6.8 microns and the brightness temperature at 10.7 microns from GOES 11. The red line indicates the projection of the radio occultation tangent points. Image from Biondi et al. (2011b).

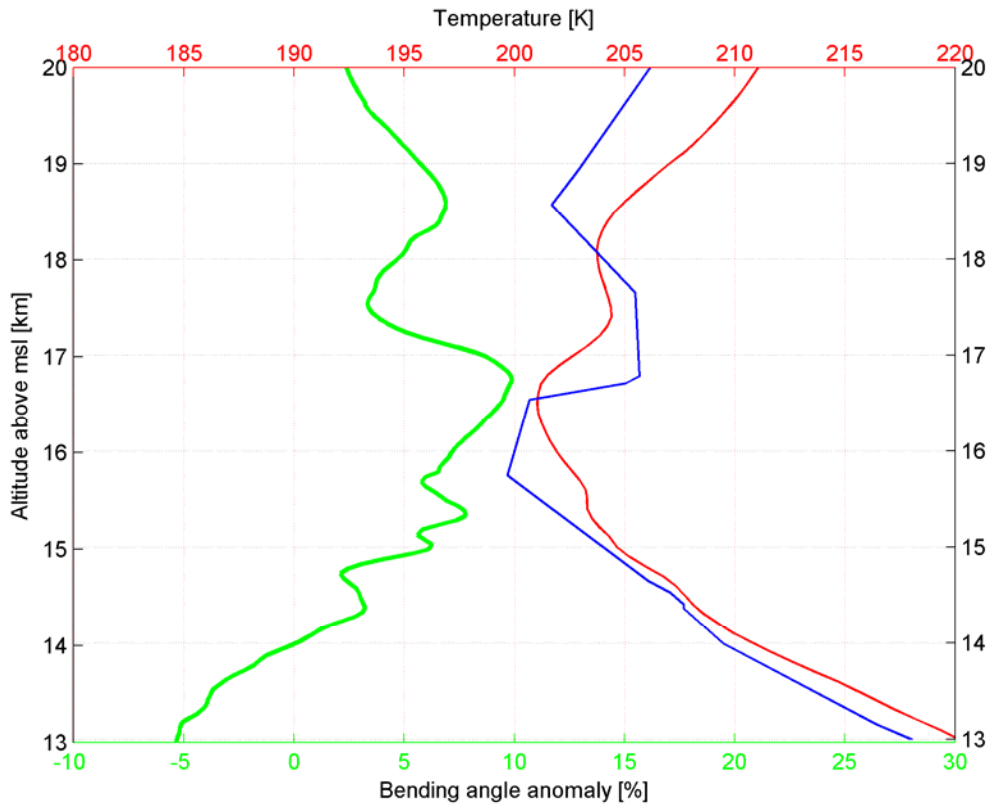

Figure 5.12: In green the bending angle anomaly for the radio occultation acquired from COSMIC the 22nd of August 2009 at 08.27 UTC during the hurricane Bill. In red the RO temperature profile and in blue the co-located RAOB temperature profile (Bermuda station). Image from Biondi et al. (2011b).

5.2.3 Case study: Krosa 2007

We report this case (Biondi et al., 2011d) in addition to the Bertha 2008 and Bill 2009, because this is one of 13 cases where we have found co-location with CALIPSO track providing an independent measurement of the TC top with high vertical resolution, and because also WWLLN data are available as independent proxy for convection. Krosa was a typhoon developed in the Western Pacific basin between the 1st and the 8th of October 2007, reaching the maximum strength the 5th of October as tropical cyclone Cat. 3 with a maximum sustained wind speed of 105 Kt. We analyzed it on the 2nd of October when Krosa was tropical storm with the eye located at 16.5N and 131.5E, with maximum sustained wind speed of 55 kt and minimum pressure of 990 hPa, rapidly intensifying to TC Cat. 1. A GPS RO profile was acquired at 03.42 UTC near the eye-wall and CALIPSO overpassed the storm at 04.50 UTC at about 60 km from the RO tangent point (Figure 5.13). The water vapor BT from GMS at the same time and in the same location as the RO, was lower than 205 K and the 11 microns BT was lower than 200 K. The

same BT values were measured at 04.50 UTC in the area where CALISPO detected the top of the storm. This suggested an inversion of BT due to convective clouds (see paragraph 4.4). Between 03.30 and 04.30 UTC more than 1500 strokes were detected from WWLLN in the same area of the RO.

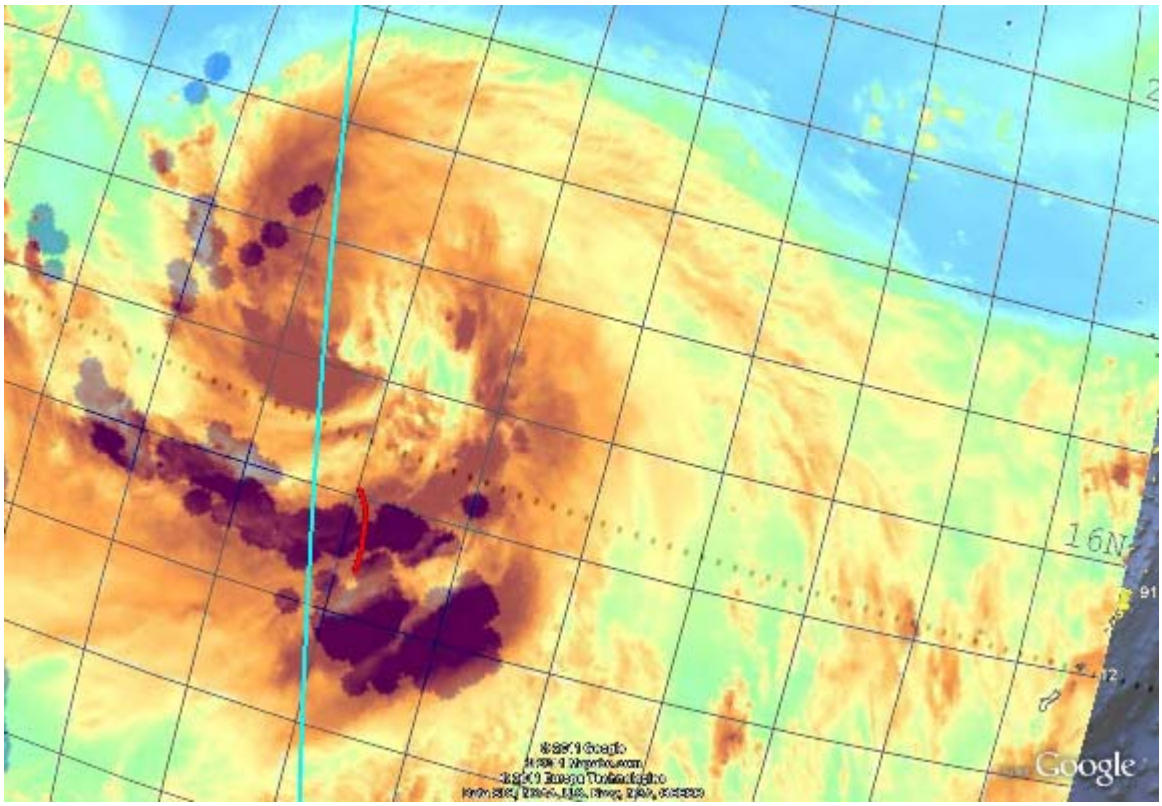

Figure 5.13: Typhoon Krosa, 2nd of October 2007. The background map is the GOES water vapor image at 03.45 UTC, the blue dots are the WWLLN strokes detected between 03.30 and 04.30 UTC, the cyan line is CALIPSO track at 04.50 UTC and the red line is the GPS RO tangent point at 03.42.

The $\alpha_{Anomaly}$ profile (Figure 5.14, left panel) shows a double positive spike in the UTLS. The lower spike is at 17.1 km of altitude, 400 m above the lowest coldest point of 192 K and another spike is a couple of km above corresponding to a second temperature minimum of 199 K. The maximum altitude of the cloud top (altitude where the total attenuated backscatter at 532 nm is higher than the background value) shown by CALIOP (Figure 5.14, right panel) is 16.9 km, just 200 m below the lower bending angle spike. A clear double tropopause is depicted in the temperature profile with the coldest point (corresponding with the lowest tropopause) 200 m below the top of the TC.

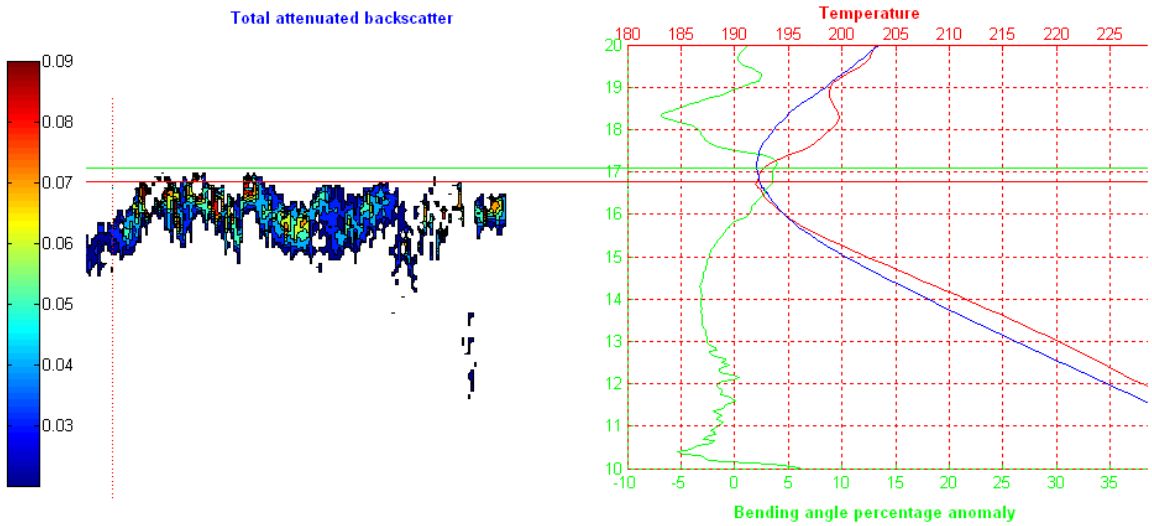

Figure 5.14: Krosa, 2nd of October 2007. Total attenuated backscatter at 532 nm from CALIOP (left panel) and the GPS RO profiles (right panel) with the bending angle anomaly (green), the temperature during the storm (red) and the climatological temperature (blue). The horizontal red line is the altitude of the coldest point and the horizontal green line is the altitude of the bending angle anomaly spike.

5.2.4 The TC top determination

The RO_{ctop} for the 13 TCs co-located with CALIPSO, was computed using the procedure described in the paragraph 4.2. All the selected cases were compared with the CALIPSO ground track coordinate files to find RO profiles co-located with CALIOP vertical cross section attenuated backscatter. This allowed us to get an independent validation of the effectiveness of our algorithm. The meteorological satellites data were used to monitor the position of the RO, the CALIPSO track and the RAOB relatively to the position of the storm. We also used GOES BTs and the WWLLN as further proxy of convection using the technique described in the paragraph 4.4. When it was possible, we used the co-located RAOB profiles as comparison for the temperature profiles.

In all the cases analyzed in this study, the bending angle anomaly shows a spike in the UTLS (often corresponding to a coldest point in the temperature profile), revealing sometimes a clear double temperature minimum (i.e. Krosa). In these cases the lower spike corresponds to the cloud top altitude and the higher one to the standard tropopause altitude. When the double temperature minimum is not present, the TC cools the tropopause by a few degrees in respect to the climatology. The TCs (stronger than any other convective systems) can reach the tropopause, and 2 different processes can happen: the tropopause is lifted up by the convection (Romps and Kuang, 2009) creating a double temperature minimum like in Krosa or the cloud top contributes to cool down the temperature of the standard tropopause (Pommereau and Held, 2007).

Our algorithm estimates the cloud top altitude with a good accuracy, within the 13 cases validated with co-located CALIOP measurements. The RO_{ctop} was compared with the maximum cloud top detected from CALIOP and with the storm averaged altitude from CALIOP, due to the co-location uncertainties (in time and space) between the RO tangent point and CALIPSO track.
In general, we detected the maximum cloud top altitude with a root mean square error of 365 meters with a correlation coefficient of 0.98. The correlation coefficient is still high (0.93), comparing the RO_{ctop} with the averaged altitude but a bigger bias is evident (Figure 5.15).

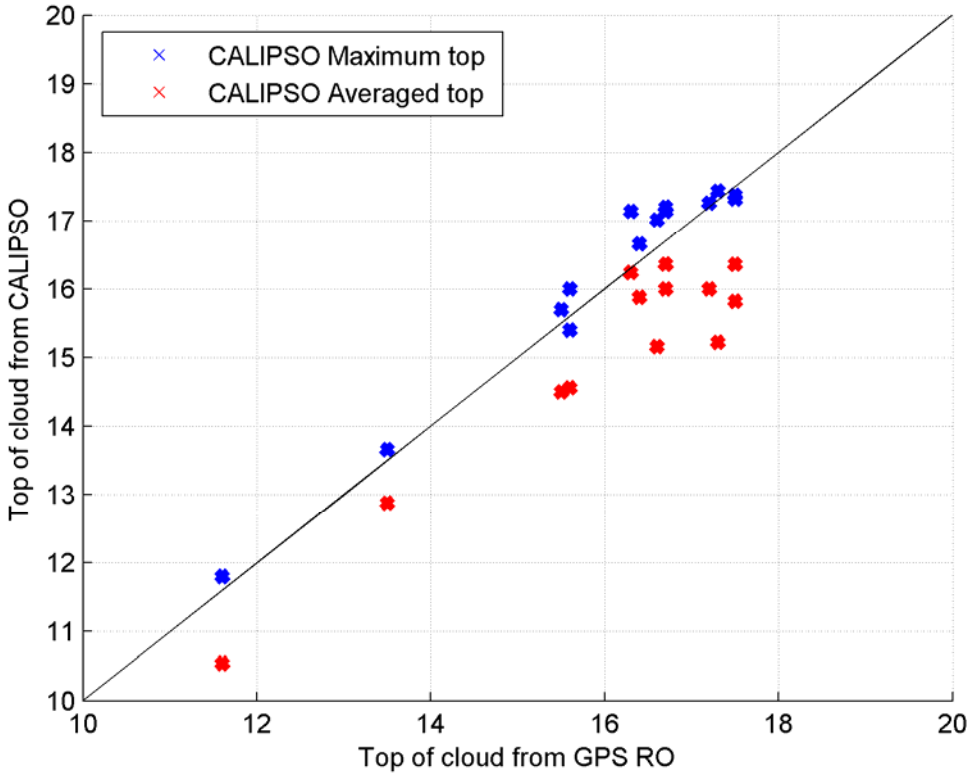

Figure 5.15: Scatter plot between the cloud top obtained using the bending angle anomaly technique (x-axis) and from CALIOP (y-axis), the blue crosses are related to the highest top of the TC and the red crosses with the averaged top of the TC. Image from Biondi et al. (2011d).

Considering the cloud top altitude from CALIOP (Zo) as reference, we plotted in Figure 5.16 the bending angle anomaly (together with the standard deviation) and the correspondent temperature anomaly as a function of altitude from 5 km below to 5 km above the top. Below the top detected by CALIOP (between 5km and 2 km), the troposphere is warmer than the climatology and the bending angle anomaly is negative. Approaching the cloud top (from 2km below to the top) the bending angle anomaly

rapidly increases, becoming positive and reaching the maximum amplitude exactly at the cloud top where the temperature is colder than the climatology. Above the cloud top there is not any significant variation in bending angle and temperature.

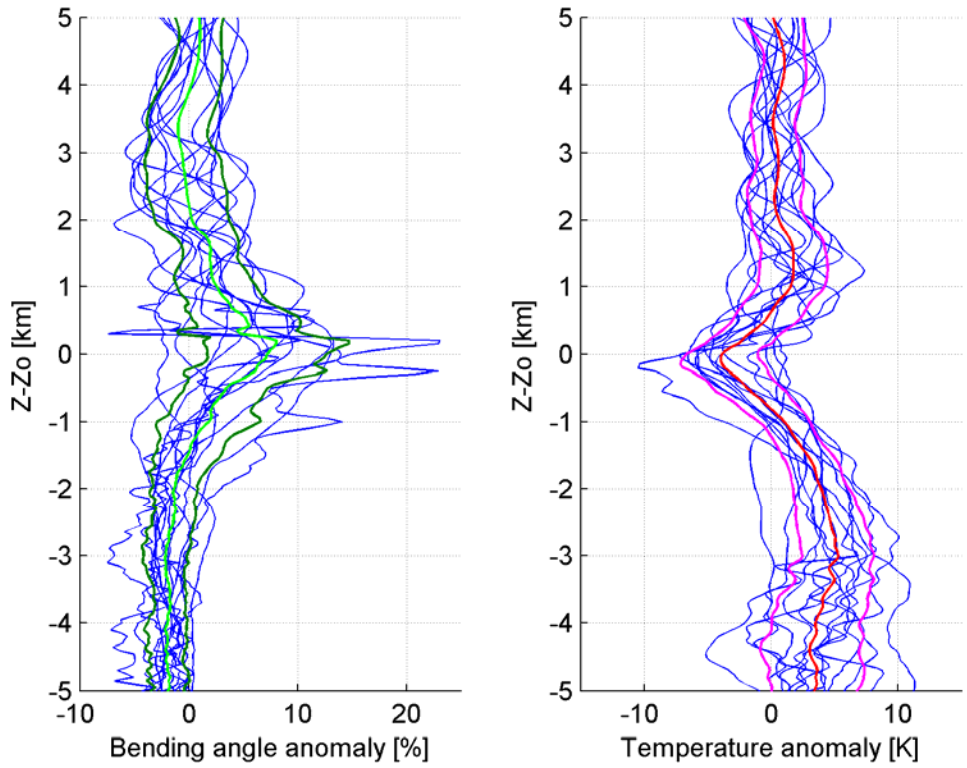

Figure 5.16: Bending angle and temperature anomaly in respect to the altitude of the cloud top Zo (±5 km) for the 13 ROs during TCs co-located with CALIOP. The blue lines are the anomalies of any single event, the green line is the averaged bending angle anomaly (± the standard deviation in dark green), and the red line is the averaged temperature anomaly (± the standard deviation in magenta).

5.2.5 Model analysis

The CM1 was used to simulate extreme TC (Rotunno and Emanuel, 1987) with different radiative schemes. The aim of the simulation was to verify if the temperature variation (double tropopause) on the top of the TC is also assumed by the model and if this depends on the radiative scheme. Any scheme can include free-floating cloud droplets and ice crystals as well as snowflakes, moderate density graupel particles and higher density ice like hail. Numerical models cannot track every particle, so the physics of condensate creation, growth, destruction and motion has to be parameterized. "Cloud microphysics" refers to how these processes are handled in a model. There are many

microphysical schemes, employing different assumptions regarding condensate number, habit, history and behavior. The available schemes for CM1 are:

1) *Rotunno-Emanuel simple water only scheme* – This is the basic scheme usually used in CM1, which is a model including a simple relaxation term that simulates the atmospheric radiation. It is a really idealized model including water vapor, cloud water and rain (Rotunno and Emanuel, 1987).
2) *Kessler scheme* - It is a simple warm cloud scheme, including water vapor, cloud water, and rain. This is the simplest scheme since it admits only two forms of condensate: cloud droplets and rain. The microphysical processes are the production, fall and evaporation of rain, the accretion and auto-conversion of cloud water, and the production of cloud water from condensation (Kessler, 1969).
3) *Morrison double-moment scheme* – This is a double-moment bulk microphysics scheme predicting the number concentrations and mixing ratios of four hydrometeor species: droplets, cloud ice, rain, snow (Morrison et al., 2005).
4) *NASA Goddard version of Lin-Farley-Orville (LFO) scheme* - The LFO scheme (Lin et al., 1983), adds three forms of frozen water to the simple water scheme (like Kessler): ice crystals, snowflakes and graupel. Two dimensional time dependent cloud model specifically realized to simulate the thunderstorms. Six forms of water are simulated: water vapor, cloud water, cloud ice, rain, snow and hail. The model uses the "bulk water" microphysical parameterization technique to represent the precipitation scheme with exponential size distribution function. It is included the accretion process for liquid and solid hydrometeors, the transformation of cloud ice to snow and the subsequent accretional growth to form hail. Also the evaporation and sublimation processes for the precipitation outside the cloud, the melting of hail and snow and the wet and dry growth of the hail are included. This is the most complex scheme used by CM1.
5) *Gilmore/Straka/Rasmussen version of LFO scheme* – In this case the LFO scheme is used with the ice processes switched off (Gilmore et al., 2004).
6) *Thompson scheme* – Any hydro meteor class (cloud water, rain water, pristine ice, snow and graupel) is represented using a simplified one parameter function for each term and two parameter function for cloud ice (Thompson et al, 2004).

The model was run for an axisymmetric TC with different horizontal resolution, vertical resolutions, domain ranges and life time of the cyclone. All these parameters were gradually increased to avoid simulation time issues.
The CM1 starting from the initial conditions develops a TC with increasing strength which becomes stationary after about 4-5 days. The first simulation was done with horizontal resolution of 15 km with a domain of 1500 km from the eye, vertical resolution of 1.25 km with a vertical domain of 20 km, and cyclone life time of 8 days.

With this structure, the simplest radiative schemes (Rotunno-Emanuel and Kessler), shows stronger convection reaching higher altitudes than the other schemes. In all the schemes, corresponding to the TC top, the density of potential temperature iso-lines is increasing and the thermal structure of the cyclone is the same: warming in the lower and mid troposphere in respect to the initial conditions, cooling on the top and quick warming above the top (not shown). This behavior is valid for a few hundred km from the eye and when the TC is mature. Increasing the vertical resolution to 250 meters with a domain of 25 km and the TC life time of 11 days, we could better define the structure of the perturbation and analyze its thermal structure distinguishing the differences within the different radiative schemes.

Figures 5.17, 5.18 and 5.19 show respectively the vertical wind component, the u-component and the v-component cross section (between the ground and 25 km of altitude and within 450 km from the TC eye) of the TC after 11 days from the formation with the different schemes. Rotunno-Emanuel and Kessler schemes, even if idealized water scheme only, approximate very well the other radiative schemes. The major noticeable difference is that the "water only" schemes reach higher altitudes with stronger convection, but all of them show the maximum intensity of the storm between 30 and 50 km from the eye.

In figure 5.20 is shown the cloud liquid content (for Rotunno-Emanuel and Kessler) and ice cloud content (for Gilmore, Morrison, NASA and Thompson) cross section corresponding to the same domain described before for the winds. The anvil from the "water only" schemes is much larger (horizontally and vertically) than in the other cases, unfortunately given to the different parameters provided by the simulations (water and ice) it is not possible to compare quantitatively these plots.

Figure 5.21 shows the thermal structure of the cyclone with respect to the initial conditions. The temperature anomaly is reported in all the panels with reddish colors representing warming and bluish colors representing cooling. All the schemes depict the warm core of the storm in the lower-mid troposphere and the cooling at the top followed by a new warming above the top. The water only schemes do present the warming just near the TC eye, instead the other schemes present the same effect also at a few hundred km away from the center. Morrison, NASA and Thompson schemes suppose the cool TC anvil trapping the heat below. The cooling corresponding to the top of the TC and the warming above that, is common to all the simulations. Sounding the TC at 40 km from the eye (Figure 5.22), distance where the maximum strength is usually detected, all the schemes show a clear wave above the top except Rotunno-Emanuel scheme that shows a profile extremely similar to those ones retrieved by the GPS ROs.

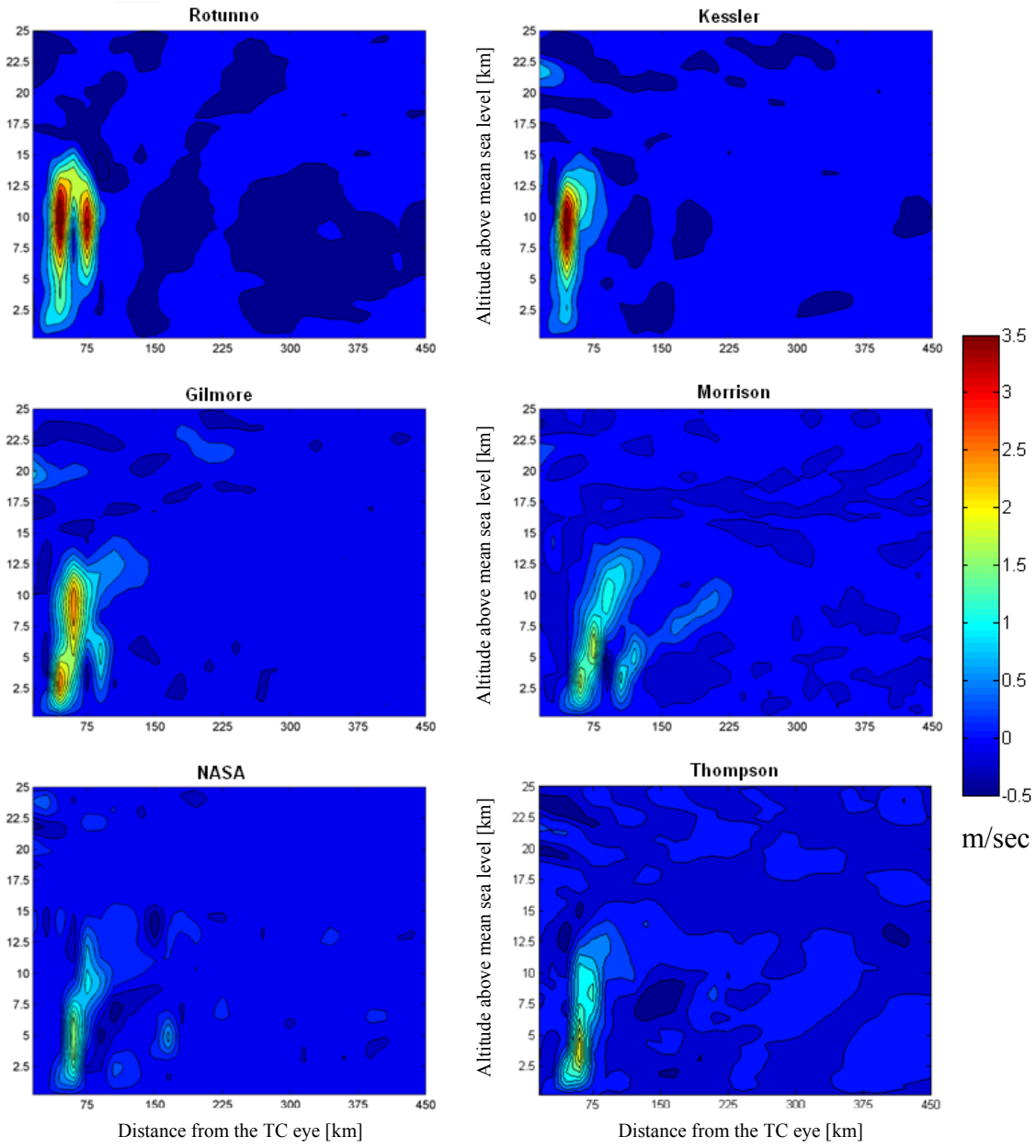

Figure 5.17: Simulated vertical wind cross section during a TC Cat. 5 after 11 days from the formation under different radiative scheme conditions.

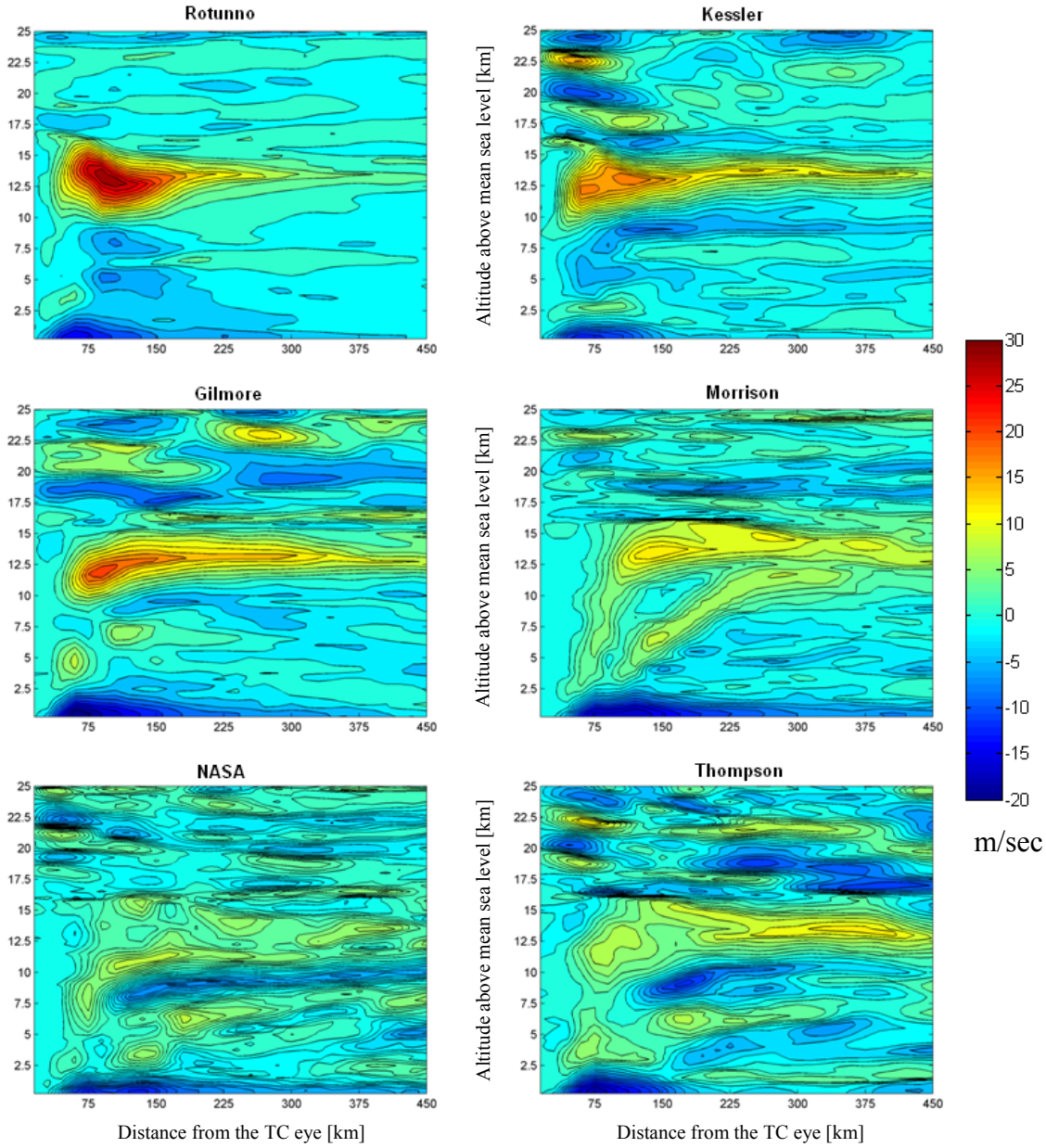

Figure 5.18: Simulated u-component wind cross section during a TC Cat. 5 after 11 days from the formation under different radiative scheme conditions.

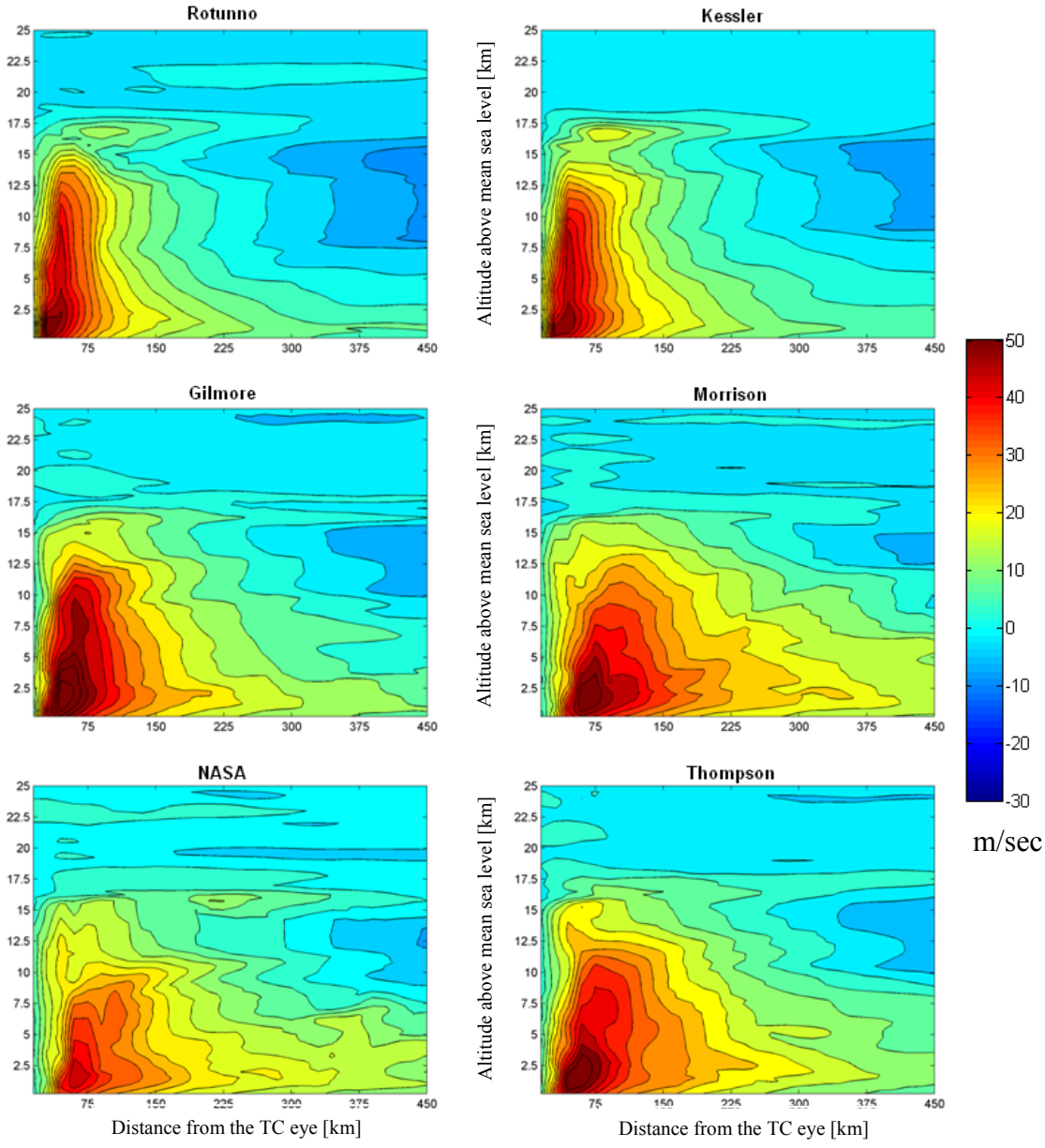

Figure 5.19: Simulated v-component wind cross section during a TC Cat. 5 after 11 days from the formation under different radiative scheme conditions.

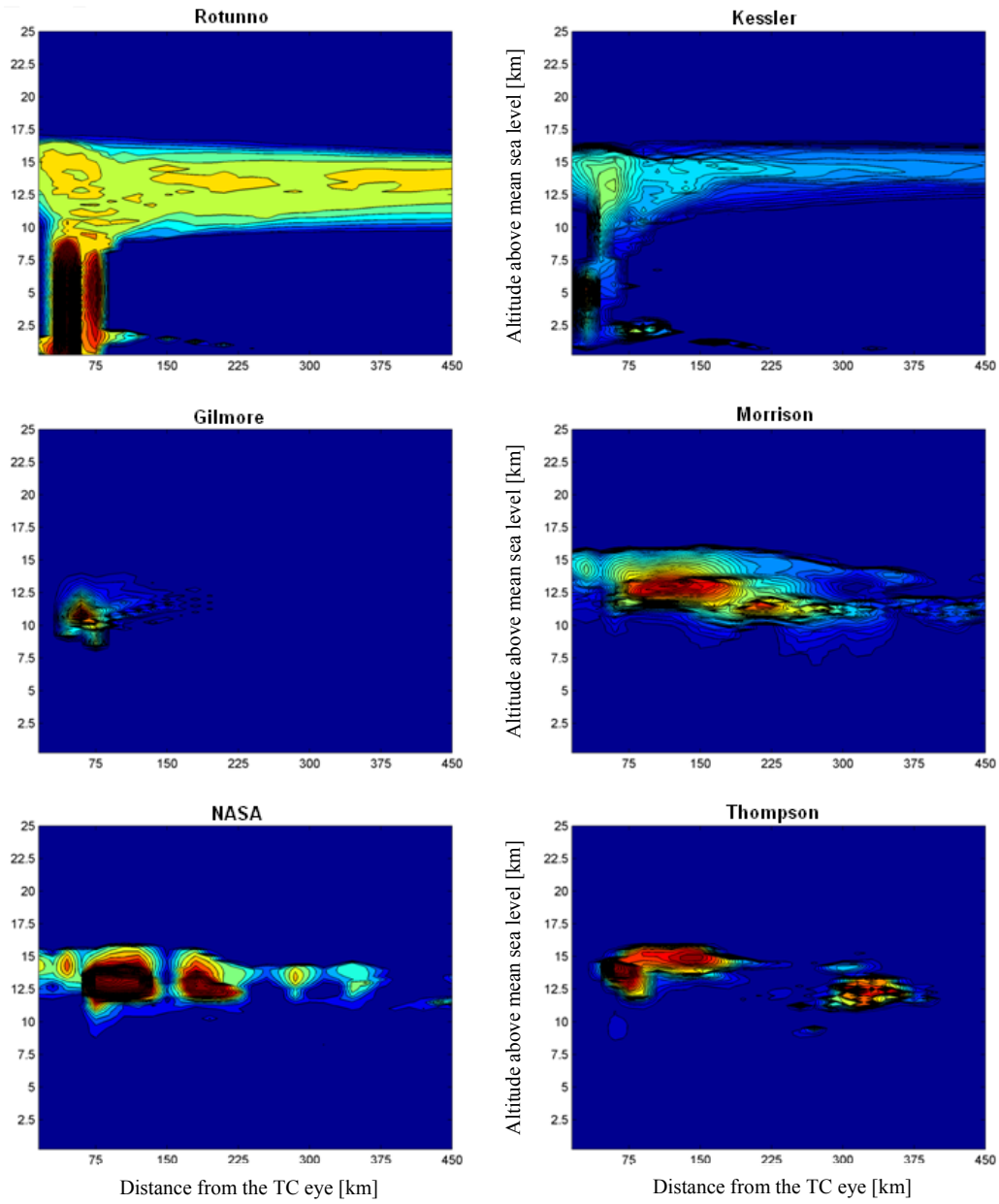

Figure 5.20: Simulated water anvil cloud (Rotunno and Kessler) and ice anvil cloud (Gilmore, Morrison, NASA and Thompson) during a TC Cat. 5 after 11 days from the formation under different radiative scheme conditions.

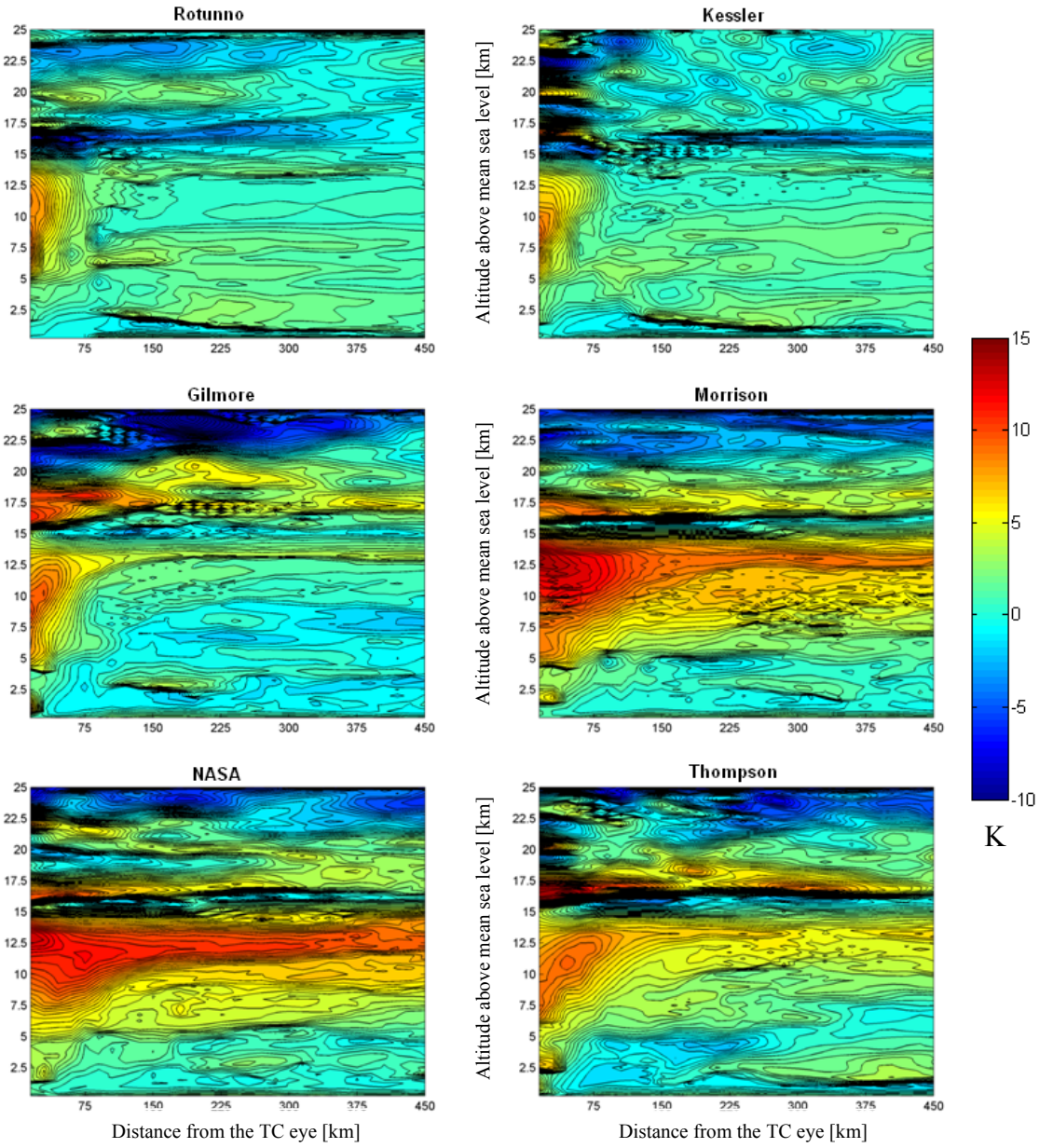

Figure 5.21: Temperature anomaly structure of a simulated TC Cat. 5 respect to the initial conditions with different radiative schemes.

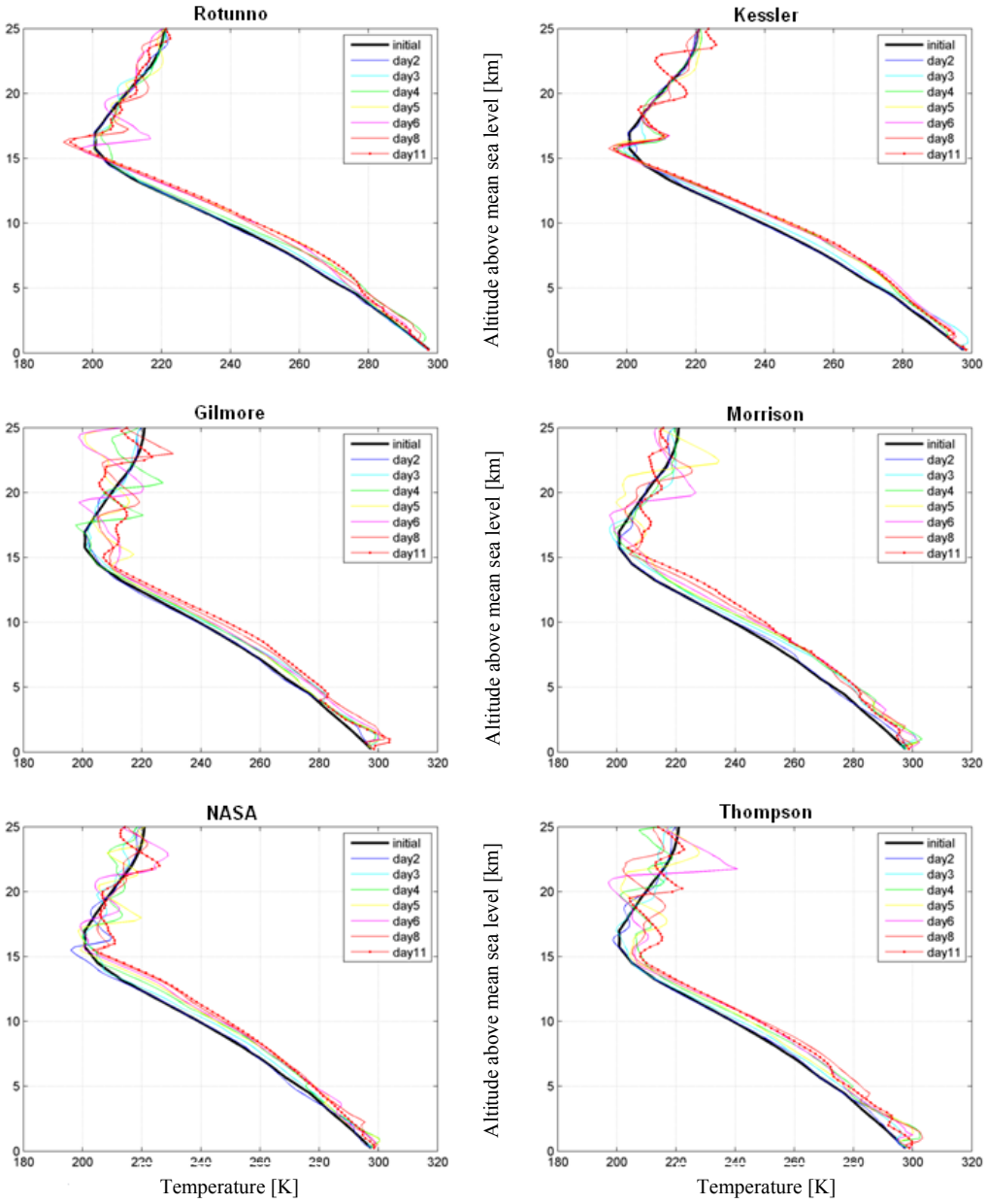

Figure 5.22: Temperature soundings at 40 km from the TC eye of a TC Cat. 5 from the initial conditions to the 11th day.

5.2.6 Statistics

More than 60% of the 1194 cases analyzed during TCs, present maximum anomaly in the UTLS between 5% and 15% greater than the climatology (Figure 5.23). Just 2% of these cases do not present any positive anomaly spike in the UTLS; since not any additional information regarding the size of the cyclone is available, we are not sure they were acquired inside the storm. The distribution of mean negative anomaly (Figure

5.24) between 14 and 18 km during TCs, shows that the 81% of the cases reveal a positive anomaly.

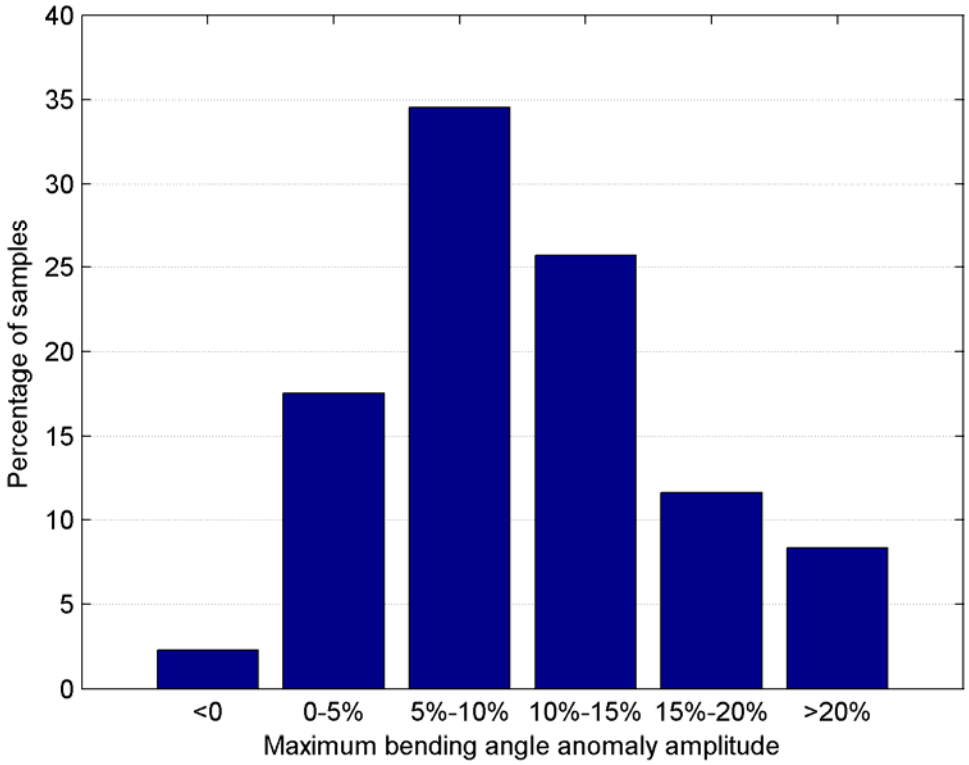

Figure 5.23: Distribution of positive peak bending angle anomalies between 14 and 18 km during TCs. Image from Biondi et al. (2011b).

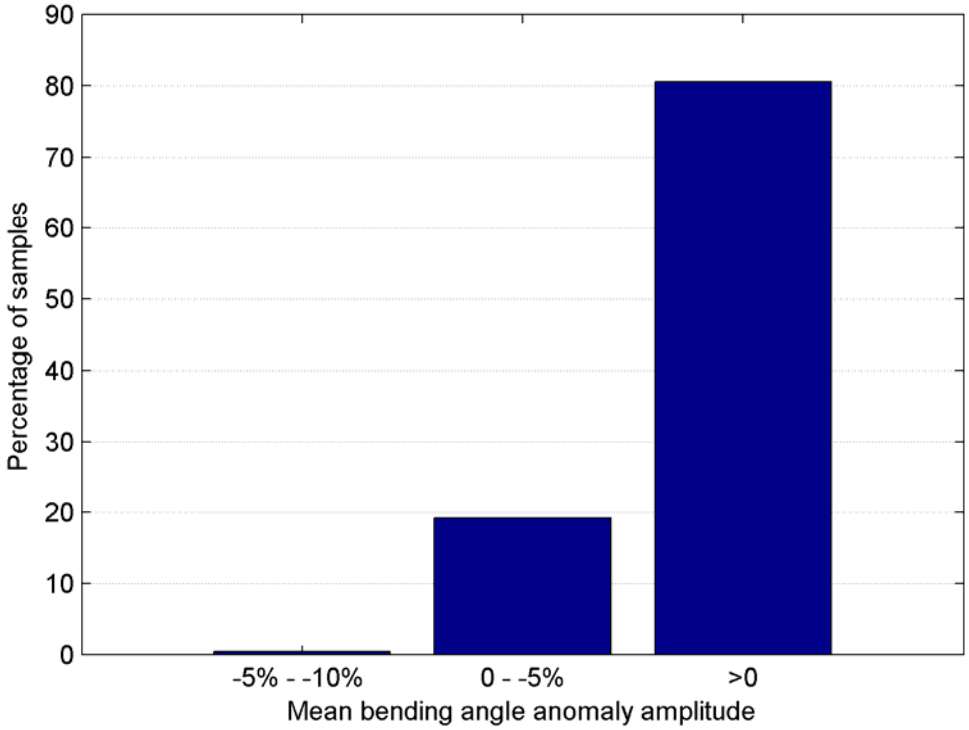

Figure 5.24: Distribution of mean negative bending angle anomalies between 14 and 18 km during TCs. Image from Biondi et al. (2011b).

During normal conditions (not shown), i.e., in the absence of TCs, the probability to get positive or negative anomaly in the same areas of the globe is evenly distributed (48% of chance to get negative anomaly and 52% having positive anomaly). This is because in normal conditions we include clear sky acquisitions but also many storms not selected as TCs.
About 60% of the 1194 ROs selected during the TCs present a double bending angle anomaly spike corresponding to a double tropopause in the UTLS where the first spike coincides with the storm top altitude and the higher one is a couple of km above. The other 40% present a single spike at the storm top altitude corresponding to a temperature decrease with respect to the climatology.

Out of the 1194 RO profiles, we sub-selected the acquisitions co-located with RAOB (Biondi et al., 2011d). The co-location is assumed to be in a time window of 6 hours and a space window of 400 km from the RO according to the CDAAC standard. A relevant number of RAOBs (291) was found with these criteria, but the number decreases if we consider the soundings reaching the UTLS (246). By applying the bending angle algorithm (eq. (4.4)) to all the 246 cases to detect the RO_{ctop} and by comparing the temperature anomaly (eq. (4.5)) at the RO_{ctop} from the ROs versus the temperature

anomaly at the same altitude from the RAOBs, a general good agreement is found (Figure 5.25), with correlation coefficient of 0.72, a mean bias of 0.95K and a standard deviation relative to the mean bias of 1.15K. However the correlation coefficient between the $\alpha_{Anomaly}$ and the $T_{Anomaly}$ from the RAOB at the top of the cloud is quite low (-0.47). The difference is probably due to the time/space distance and the coarse vertical resolution of the RAOB: the maximum temperature anomaly altitude could not exactly correspond to the maximum bending angle anomaly altitude.

Within the same dataset of 246 cases during TCs, in Figure 5.26 are shown the $\alpha_{Anomaly}$ and the $T_{Anomaly}$ from RAOB (together with the standard deviation of the mean) in the range from 5 km below to 5 km above the RO_{ctop}. It is clear from the plot that a positive $\alpha_{Anomaly}$ corresponds to a negative $T_{Anomaly}$ from the RAOBs. In the warm troposphere below the cloud the $\alpha_{Anomaly}$ is negative, at the RO_{ctop} the temperature is colder than the climatology and above the RO_{ctop} there is a decrease of $\alpha_{Anomaly}$ with a temperature relaxation to the climatological values. The temperature profile from a statistically significant dataset of RAOBs confirms, the same temperature trend that we have found for the 13 ROs co-located with CALIPSO (section 3.3): below the RO_{ctop}, the troposphere is warmer than the climatology and the $\alpha_{Anomaly}$ is negative, at the RO_{ctop} the temperature is colder than the climatology and the $\alpha_{Anomaly}$ reaches the maximum, and above the cloud top there is not any significant variation in bending angle and temperature.

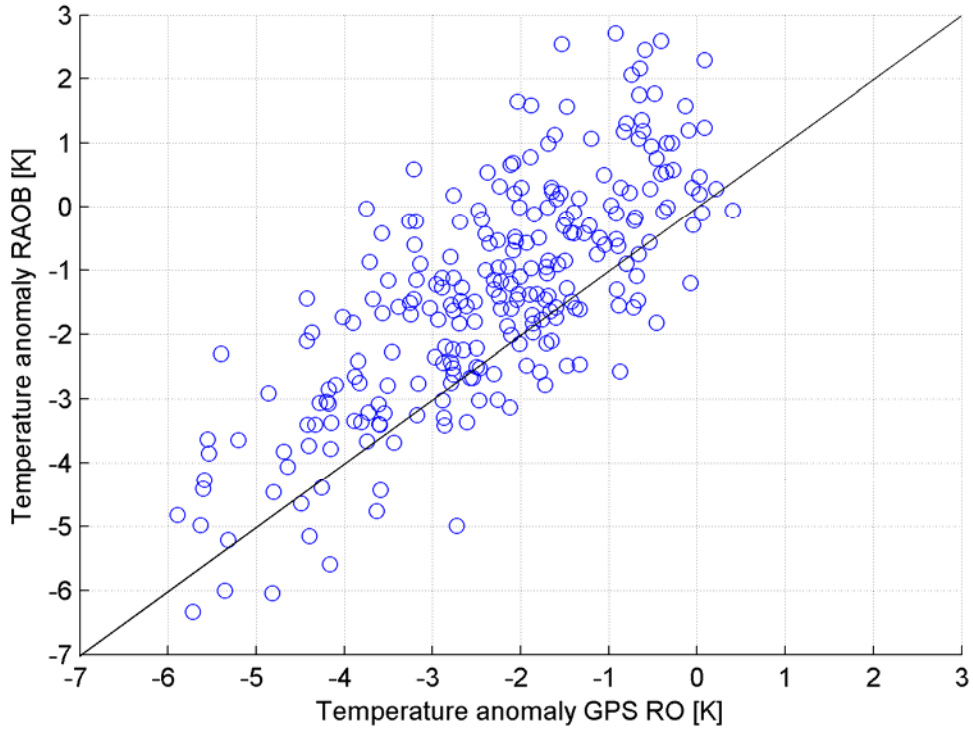

Figure 5.25: Scatter plot between the temperature anomaly from GPS radio occultations and the temperature anomaly from the co-located 246 radiosondes reaching the UTLS at the cloud top altitude. Image from Biondi et al. (2011d).

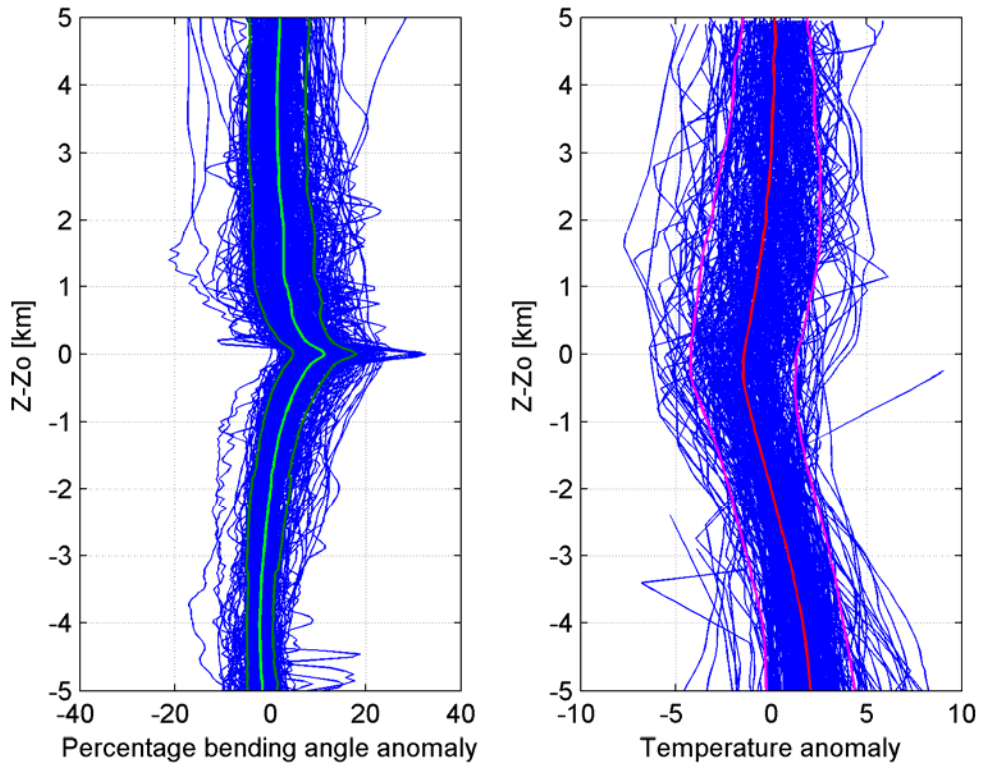

Figure 5.26: Bending angle and temperature anomaly with respect to the altitude of the cloud top Zo (±5 km) for the 246 ROs co-located with RAOBs. The blue lines are the anomalies of any single event, the green line is the averaged bending angle anomaly (± the standard deviation in dark green), and the red line is the averaged temperature anomaly (± the standard deviation in magenta).

5.3 Convective systems

After the TCs, the ISCCP Deep Convection Tracking Database was analyzed with the same procedure as above, co-locating the CC with RO and CALISPO track. In the period June 2006-July 2008 (period of availability of CALIPSO and ISCCP dataset) we have got 2157 coincidences between ROs and CC in a time window of 2 h and within the radius of the CC itself. The further comparison with CALIPSO track provided 53 cases (Table 5.5) that we used as basis for our analysis, 38 within 30^{o} N-S and 15 within the

mid-latitudes (Figure 5.27). All the results shown in the next 2 sections (5.3.1 and 5.3.2) are detailed in Biondi et al. (2011c).

Convective System	Distance [km]	Time distance [min]	Area
26/11/2006	45	20	China
20/01/2007	85	113	Kiribati
26/01/2007	84	49	Polynesia
28/01/2007	72	61	Paraguay
30/01/2007	95	36	North Pacific
01/02/2007	49	38	Australia
03/02/2007	69	48	South-West Pacific
04/02/2007	57	50	Polynesia
04/02/2007	87	54	Central Atlantic
13/02/2007	92	58	Brazil
10/03/2007	90	62	USA - Texas
17/03/2007	79	69	Guyana
28/03/2007	54	53	Botswana
11/04/2007	93	96	South Atlantic
18/04/2007	94	1	Galapagos
30/05/2007	50	97	South Atlantic
02/06/2007	58	22	South Atlantic
02/06/2007	59	106	Ukraine
02/06/2007	78	27	South-West Pacific
05/06/2007	65	89	India
08/06/2007	76	40	South Pacific
02/07/2007	84	83	Indian Ocean
03/07/2007	85	104	South Pacific
03/07/2007	94	4	USA - Texas
20/07/2007	82	25	Bay of Bengal
02/08/2007	93	68	Philippines
07/08/2007	68	47	China
14/08/2007	57	98	Nigeria
27/09/2007	95	6	Sierra Leone
09/10/2007	72	14	East Pacific
02/12/2007	98	69	Australia
04/12/2007	55	60	South Africa
06/12/2007	80	29	Central Pacific
13/12/2007	99	114	Japan
09/01/2008	47	14	Canada
10/01/2008	70	21	Angola
15/01/2008	57	63	North Atlantic
22/01/2008	**18**	**30**	**Micronesia**
02/02/2008	**32**	**15**	**East Pacific**
15/02/2008	58	117	Micronesia
02/03/2008	76	119	Zaire

19/03/2008	93	5	Cameroon
29/03/2008	92	83	Samoa
03/04/2008	71	107	Sulu Sea
12/04/2008	72	23	Iraq
12/04/2008	42	24	Cook Island
14/04/2008	**64**	**75**	**West Pacific**
01/05/2008	69	115	South Pacific
07/05/2008	77	24	North Pacific
30/05/2008	95	7	New Caledonia
02/06/2008	39	49	Portugal
21/06/2008	38	11	South Atlantic
28/06/2008	99	36	Costa Rica

Table 5.5: Convective Clusters co-located with GPS radio occultation and CALIPSO track. The time and space distance in relative to GPS radio occultation mean tangent point and the closest CALIPSO track coordinates. In bold the cases detailed in the paragraph 5.3.1.

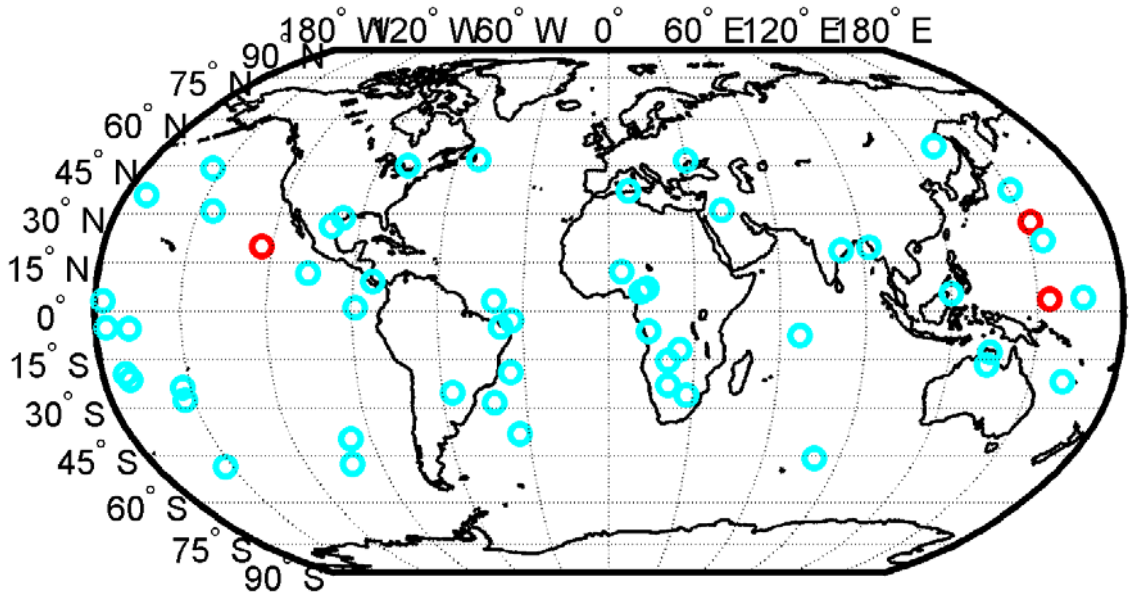

Figure 5.27: Locations of the Convective Clusters co-located with GPS radio occultations described in table 5.5. The red circles are the cases detailed in the paragraph 5.3.1.

5.3.1 Case study

Three cases (Figure 5.28) were selected from Table 5.5 (Biondi et al., 2011c), all in the tropics:

- 2nd of February 2008 (Figure 5.28, top panel)

- 22nd of January 2008 (Figure 5.28, central panel)
- 14th of April 2008 (Figure 5.28, bottom panel)

They were chosen because they represent 3 different areas of the globe and their cloud top reached different altitudes ranging from 12 to 17 km.

The first case was a squall line in the East Pacific Ocean (Latitude 21N and Longitude 123W), the GPS RO was acquired at 09.53 UTC and CALIPSO overpassed it at 10.08 UTC (15 minutes later) at a distance of 32 km from the RO. GOES BT difference shows an inversion in the area of the CS suggesting the presence of high clouds, CALIOP total attenuated backscatter at 532 nm (Figure 5.28, top left panel) shows a flat top between 12 and 12.5 km of altitude (maximum cloud top at 12.64 km and the averaged altitude of the top at 12.16 km). The right top panel of Figure 5.28 shows the $\alpha_{Anomaly}$ in green, the temperature profile during the convective system in red, the co-located temperature profile from ECMWF model in cyan and the climatological temperature profile in the same area from GPS RO in blue. The black horizontal line is the averaged altitude of the CS cloud (12.16 km), the red line is the altitude of the coldest point and the cyan line is the altitude of the standard tropopause (16.5 km).
The $\alpha_{Anomaly}$ shows a large positive spike at 12.5 km of altitude reaching amplitude of 20% and corresponding exactly to a local coldest point and just 0.14 km from the maximum CALIOP maximum cloud top. The cooling is extremely evident in comparison with the climatology of the same area: roughly 9 degrees. The temperature follows the climatological profiles up to 9 km of altitude (not shown) with the same lapse rate (moist lapse rate), from this altitude to the cloud top, the lapse rate increases reaching about 10 K/km at the cloud top level. Above the cloud, the temperature becomes warmer than the climatology and then colder again (by about 2 degrees) at the tropopause level. The temperature profile from the ECMWF model agrees with the profile from GPS RO, but, due to the coarse vertical resolution, the quick warming above the cloud is not well resolved.

The second case was in Micronesia (Latitude 4N and Longitude 154E), the GPS RO was acquired at 14.58 UTC and CALIPSO overpassed it at 15.28 UTC (30 minutes later) at a distance of 18 km from the RO, GMS shows an inversion of BTs in the area of the convective system and CALIOP total attenuated backscatter at 532 nm (Figure 5.28, central left panel) shows a convective process going on and moving upward, with the cloud top between 16 and 17 km of altitude (maximum cloud top at 16.95 km and the averaged altitude of the top at 16.24 km).
The $\alpha_{Anomaly}$ shows a large positive spike at 16.8 km of altitude near the tropical tropopause, 500 meters above the local coldest point (16.3 km) and 0.15 km below the CALIOP maximum cloud top. The cooling is also in this case really evident in

comparison with the climatology with 8 degrees of difference. Above the cloud, the temperature becomes warmer than the climatology and a new inversion shows up at 18.3 km. The temperature profile from the ECMWF model agrees with the profile from GPS RO, but does not catches the warming above the cloud.

The third case was in the western Pacific basin (Latitude 30N and Longitude 152E), the GPS RO was acquired at 17.07 UTC and CALIPSO overpassed it at 15.52 UTC (75 minutes before) at a distance of 64 km from the RO, GMS shows an inversion of BTs in the area of the convective system and CALIOP total attenuated backscatter at 532 nm (Figure 5.28, bottom left panel) shows an extremely flat cloud top with maximum cloud top at 13.95 km and the averaged altitude of the top at 13.54 km.
The $\alpha_{Anomaly}$ shows a positive spike up to 30% at 13.9 km of altitude corresponding to the local coldest point, 0.05 km below the CALIOP maximum cloud top and almost 3 km below the standard tropopause level. The cooling is also in this case really evident in comparison with the climatology with 8 degrees of difference. Above the cloud, the temperature becomes warmer than the climatology and a new inversion shows up at 18.3 km. The temperature profile from the ECMWF model agrees with the profile from GPS RO, but does not catches the warming above the cloud. The temperature anomaly near the cloud top reaches about 12 degrees, and a strong inversion is depicted above. The ECMWF analysis produces a low resolution version of this detailed structure, and completely misses the strong inversion.

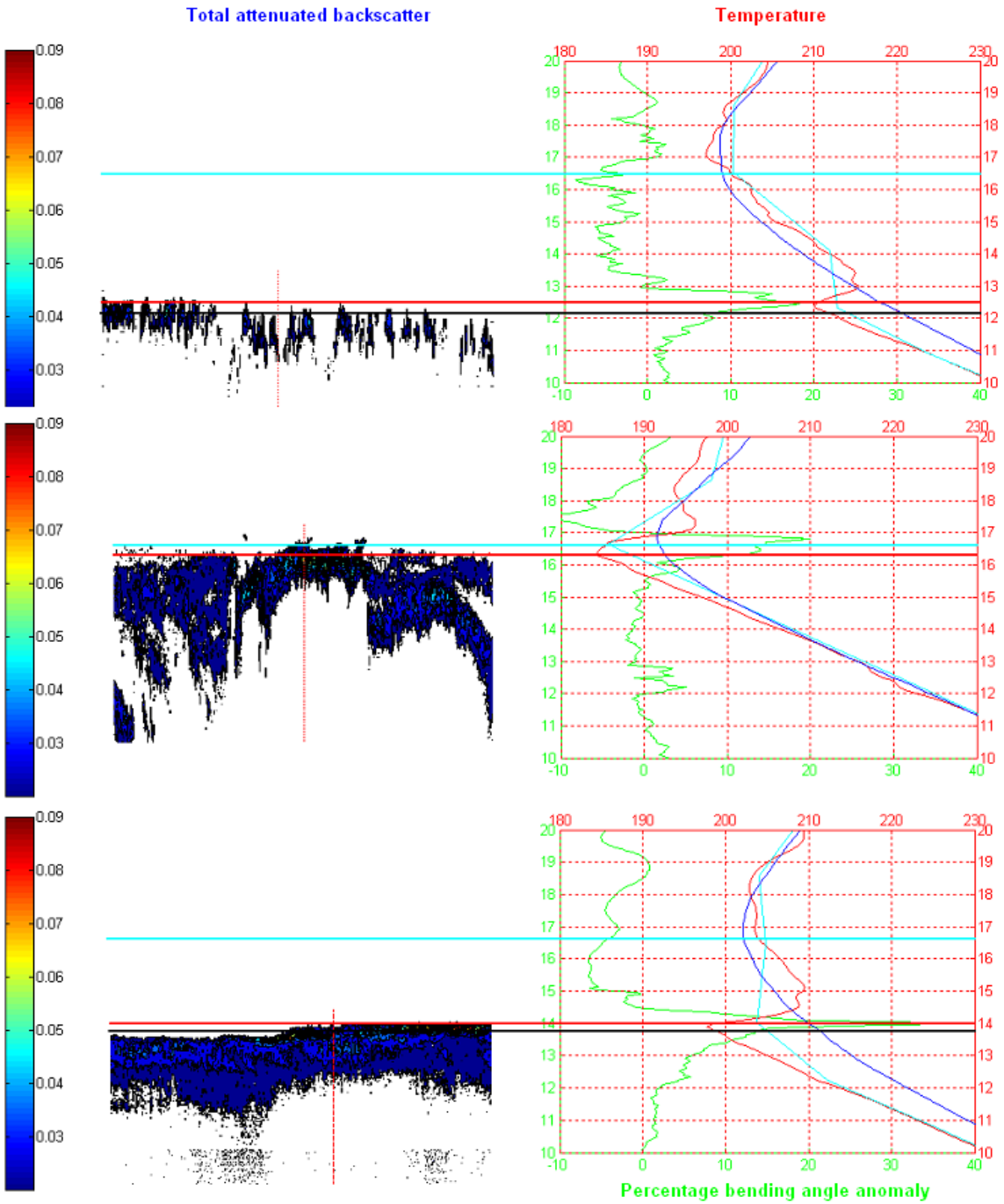

Figure 5.28: Three examples of convective systems reaching different altitude: 2nd of February 2008 (top panel), 22nd of January 2008 (mid panel) and 14th of April 2008 (bottom panel). In the left panels are plotted the total attenuated backscatter at 532 nm from CALIOP. In the right panels are plotted the bending angle anomaly profile (green), the temperature profile from GPS RO during the storm (red), the temperature profile from ECMWF model (cyan) and the climatological temperature profile (blue). The horizontal cyan line is the altitude of the standard tropopause, the horizontal red line is the altitude of the coldest point and the bending angle anomaly spike, the horizontal black line is the

averaged cloud top from CALIOP, and the vertical dashed line is the closest point to the GPS RO profile.

5.3.2 Statistics

Much of this paragraph presents the results of Biondi et al., 2011c.

In all the cases analyzed in this study, the $\alpha_{Anomaly}$ shows a spike in the UTLS (always corresponding to a coldest point in the temperature profile) with altitude lower than the standard tropopause, revealing a clear double tropopause. The Figure 5.29 shows the $\alpha_{Anomaly}$ spike altitude versus the maximum cloud top altitude from CALIOP (blue dots). The correlation is 0.93 and the root mean square error is 0.85 km. Since the GPS RO and CALIPSO track are never exactly co-located we also compare the bending angle profile with the averaged altitude of the cloud (red dots). In this case the correlation between the two altitudes is 0.85 with a root mean square error of 1.95 km, this error is mostly due to the bias. The bending angle anomaly spike altitude is well correlated to the maximum altitude of the cloud and it overestimates the averaged altitude value.

Using as reference the cloud top altitude from CALIOP, we plotted the temperature profiles (Figure 5.30), the bending angle anomaly (Figure 5.31) and the lapse rate (Figure 5.32) 5 km below and above the cloud top (Zo). These statistics are separated into cases where the cloud top altitude is below (22 cases) or above 14 km (31 cases), in order to identify any systematic differences with the depth of convection. The relative coldest point associated with the cloud is evident in all the samples reaching a maximum of more than 15 K below 14 km. Lower clouds (Figure 5.30b) show in general colder anomalies.

Associated with the cooling at the cloud top, the bending angle anomaly strong maximum is well noticeable (Figure 5.31). A mean variation of $\alpha_{Anomaly}$ larger than 10% (reaching in one case almost the 40%) is the clear signature left by the CS reaching cloud top altitudes below 14 km and a mean variation of $\alpha_{Anomaly}$ of ~5-6% is shown above 14 km. The trend of the averaged bending angle profile is symmetric to the temperature profile, confirming that the variation of this parameter in the UTLS is completely due to the temperature variation (the water vapor content amount is usually extremely low).

From the Figure 5.32 is clear how the lapse rate with respect to the climatology, starts to increase about 4 km below the cloud top and it is also evident the quick warming above the cloud, bringing back the temperature to the standard values in 1 km.

In general, as shown in Figure 5.33, during the convective systems, the temperature profile in the lower troposphere follows the climatology, but approaching the cloud top the temperature becomes colder than the climatology. Above the cloud top, is always evident a drastic warming (several degrees within a few hundred meters), then the profile follows the climatology again until the tropopause with the same lapse rate. Often the

temperature between the cloud top and the tropopause is warmer than the climatology and the coldest point is colder.

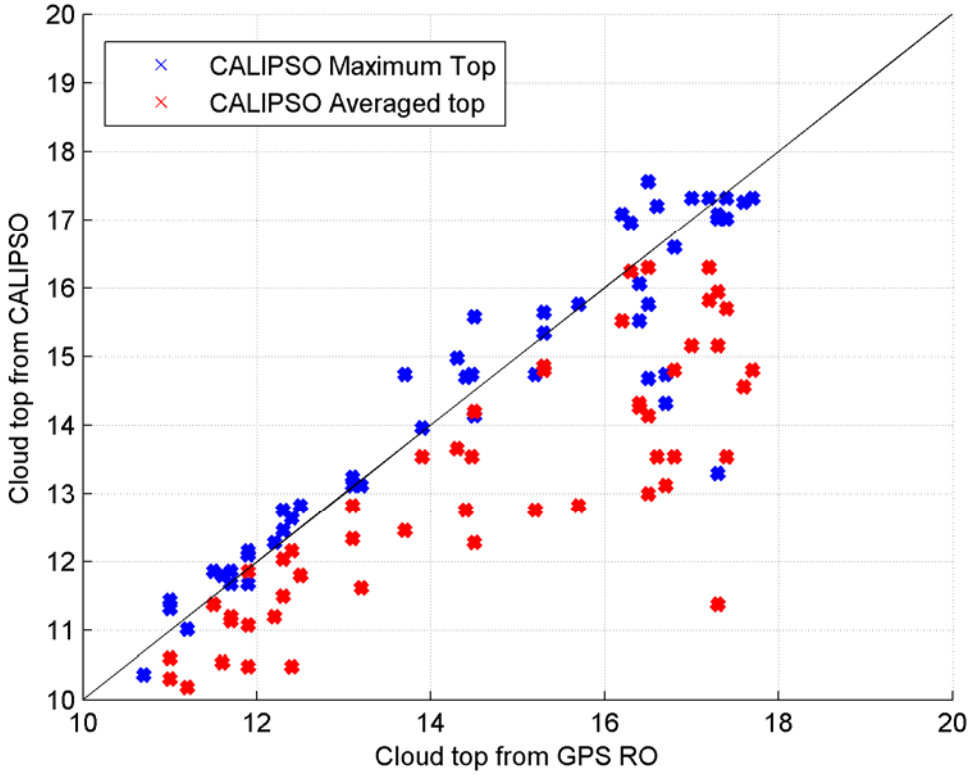

Figure 5.29: Scatter plot showing correlation between cloud top height derived from GPS RO (identified from the maximum bending angle anomaly), the maximum cloud top height from CALIOP (blue dots) and the averaged cloud top height from CALIOP (red dots).

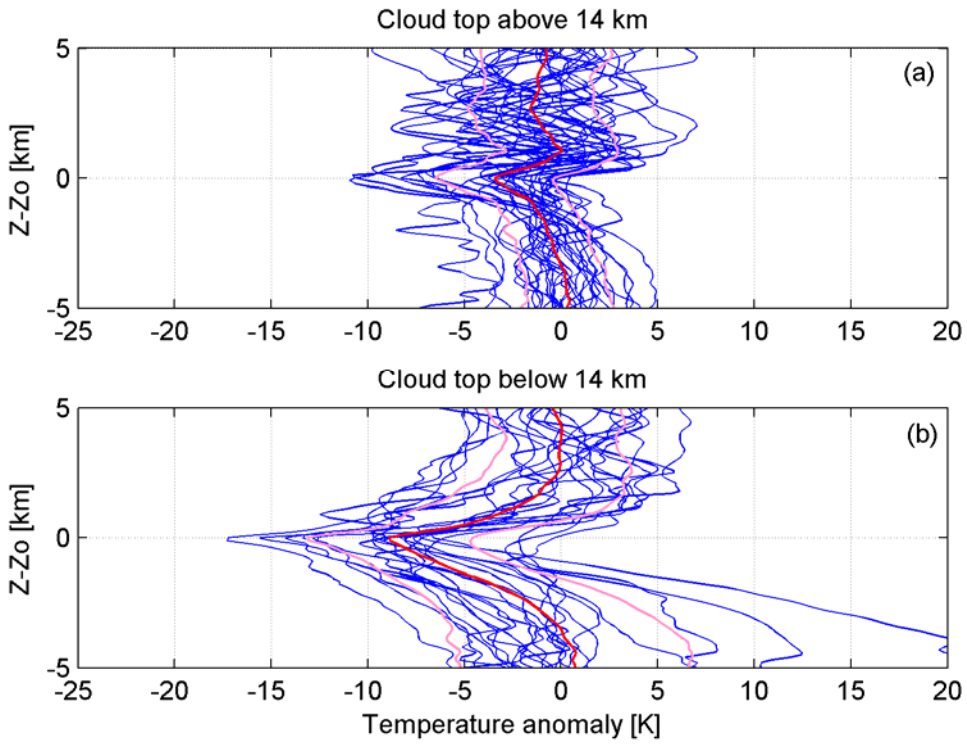

Figure 5.30: Vertical profile of the GPS temperature difference between the convective system and the background climatology, calculated with respect to the altitude of the cloud top (Zo) derived from the corresponding CALIOP measurements. Blue lines show each of the 53 cases, separated according to cloud top being above or below 14 km. The red line is the average and the pink lines are the average ± one standard deviation. Image from Biondi et al (2011c).

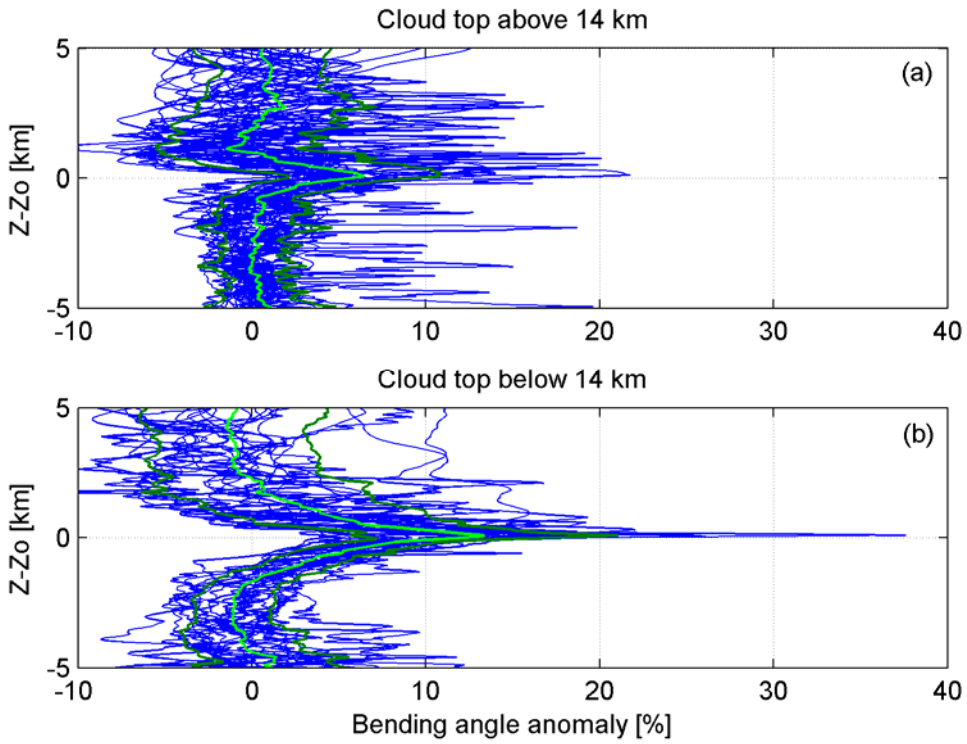

Figure 5.31: Vertical profile of the GPS bending angle anomaly, calculated with respect to the altitude of the cloud top (Zo) derived from the corresponding CALIOP measurements. Blue lines show each of the 53 cases, separated according to cloud top being above or below 14 km. The red line is the average and the green lines are the average ± one standard deviation. Image from Biondi et al. (2011c).

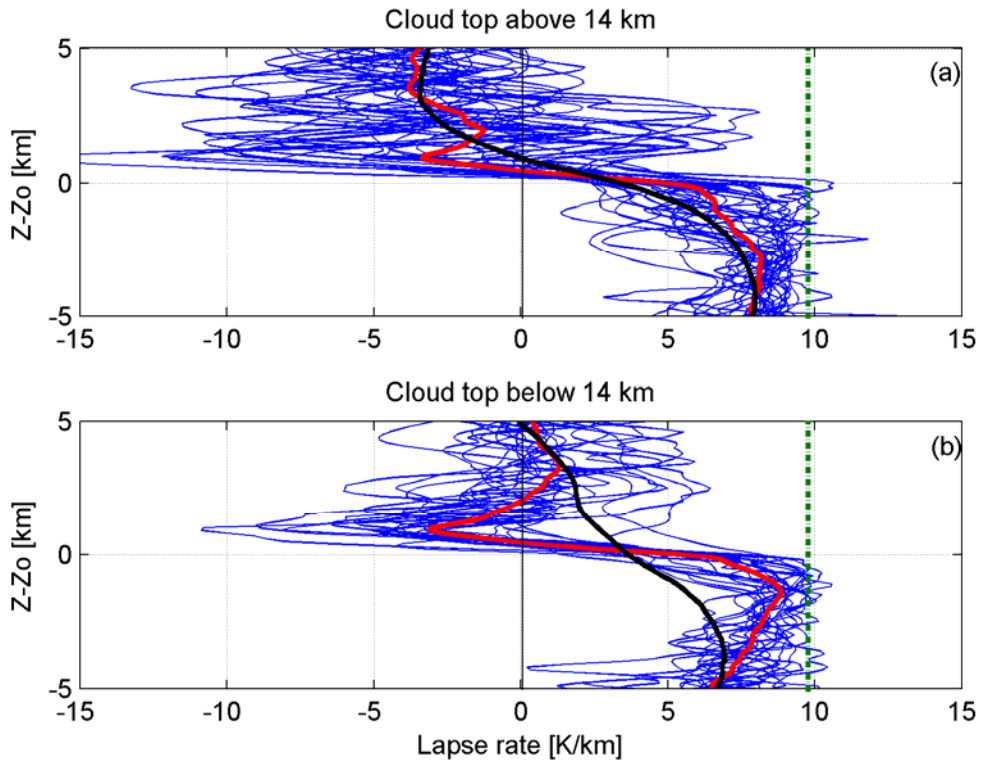

Figure 5.32: Vertical profile of the GPS lapse rate (-dT/dz) calculated with respect to the altitude of the cloud top (Zo) derived from the corresponding CALIOP measurements for 53 convective systems (blue lines). The red line is the convective systems average, the black line is the averaged climatological lapse rate and the dotted vertical green line is the dry adiabatic lapse rate (9.8 K/km). Image from Biondi et al. (2011c).

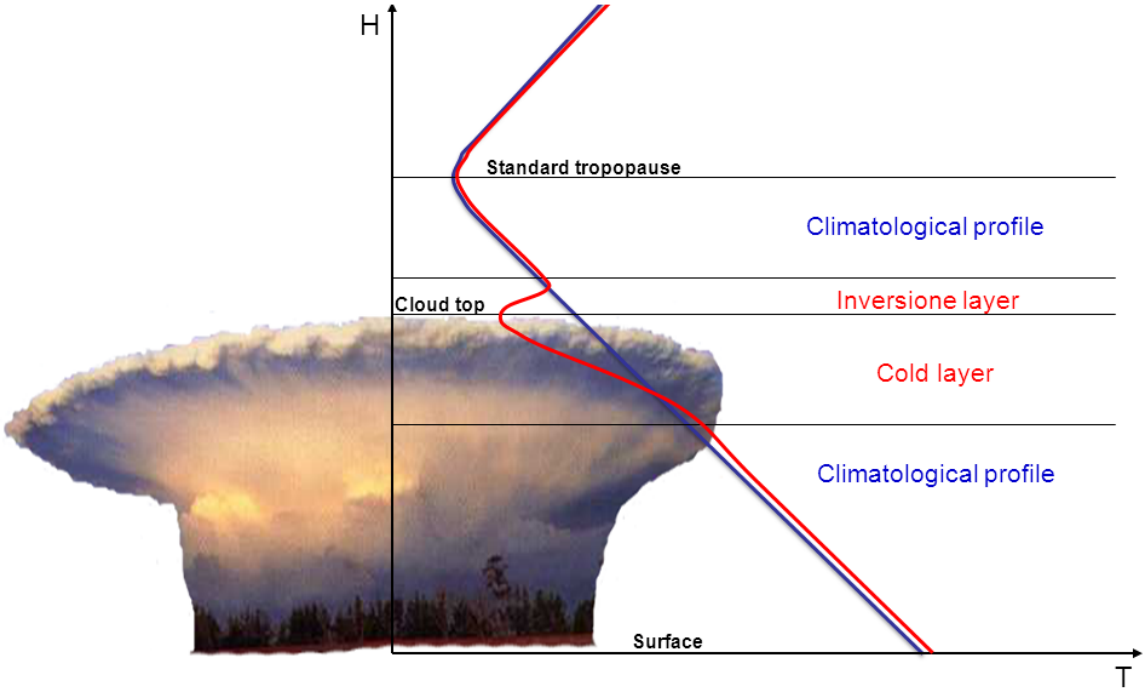

Figure 5.33: Convective system thermal structure (image from Biondi et al., 2011c). In blue the standard atmosphere temperature profile and in red the temperature profile of the convective system.

5.3.3 Campaigns data analysis

As already explained in the paragraph 3.3.2, the airborne data are the best to get detailed information on the UTLS during extreme events. From the 80´s several campaigns where conducted in the tropics for the understanding of the UTLS and the troposphere-stratosphere transport, using stratospheric airplanes such as the Russian Geophysica M55, and the American ER-2 and in the last years also the unmanned aircraft Global Hawk. Our study was focused on the campaigns ran during the GPS RO era (2001-2009).

Comparisons were done during the Tropical Convection, Cirrus, and Nitrogen Oxides Experiment (TROCCINOX) in Brasil (January-February 2005), the Stratospheric-Climate Links with Emphasis on the Upper Troposphere and Lower Stratosphere (SCOUT-O3) in Northern Australia (November-December 2005), the African Monsoon Multidisciplinary Analyses (AMMA) in West Africa (July-August 2006) and the Tropical Composition Cloud and Climate Coupling (TC4) campaign in the Eastern Pacific (July-August 2007). TROCCINOX and SCOUT-O3 campaigns were “covered” by CHAMP, AMMA campaign was “covered” by CHAMP and COSMIC and TC4 by CHAMP, GRACE and COSMIC.

During TROCCINOX not any co-located GPS RO was found, during SCOUT-O3 just 1 case was found, but it was just outside the convective system.
During AMMA campaign (Cairo et al., 2010) 3 ROs were found co-located with the flight track, one the 08th of August and two the 11th of August 2006.
During TC4 campaign (Toon et al., 2010) 1 RO from GRACE was found co-located with ER-2 track the 06th of August 2007.

a) AMMA 08th of August 2006

Figure 5.34 shows the Geophysica M55 track together with the GPS RO tangent point from COSMIC. The RO was acquired at 15.18 UTC (when Geaophysica was landing) and it was compared with the 2 profiles measured by the aircraft during the takeoff from 11.48 UTC to 12.18 UTC (Figure 5.35) and the landing from 14.36 UTC to 15.18 UTC (Figure 5.36).

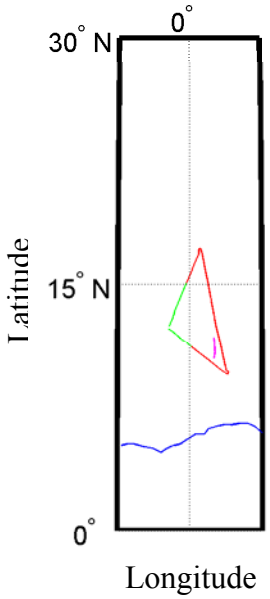

Figure 5.34: Flight track (green and red) of Geophysica M55 the 08th of August 2006. The green part is the takeoff (11.48 UTC-12.18 UTC) and the landing (14.36 UTC-15.18 UTC). The coast line is blue and the COSMIC GPS RO (15.18 UTC) tangent point is magenta.

The $\alpha_{Anomaly}$ (Figure 5.35 and 5.36, first panel from the left) shows a spike at about 14.5 km of altitude, and then another increase below 17 km. The temperature profile from the

RO (Figure 5.35, second panel from the left, red line) shows a double inversion at the same altitudes of the $\alpha_{Anomaly}$ spikes. The aircraft temperature profile (black) during the takeoff, has a trend similar to the RO temperature with the first inversion at about 14 km and the second at 17 km. The third panel from the left shows the backscatter ratio (blue, amplified by 10) and volume depolarization (green) from MAS, highlighting particles up to 14 km of altitude and some other feature between 16 and 17 km. The water vapor mixing ratio from COSMIC (red line, right panel) does not reveal any variation in the UTLS, instead the profile from FISH reveals an increase of 2 ppmv at about 16.2 km.

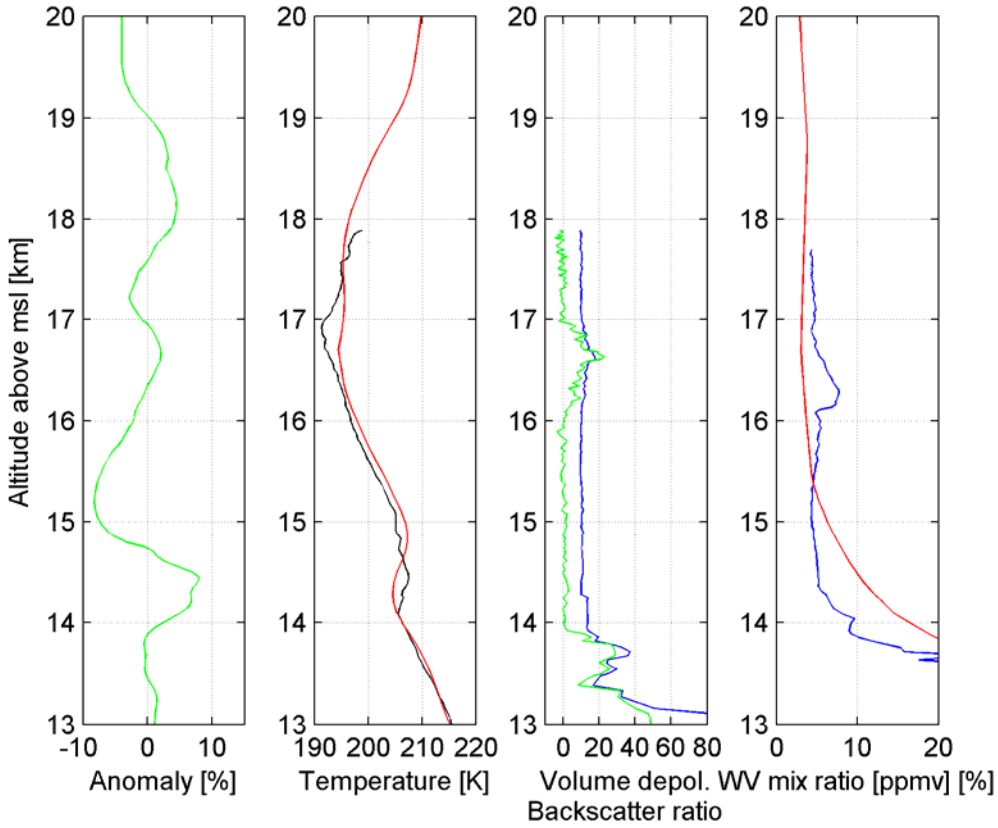

Figure 5.35: Atmospheric profiles the 8th of August 2006 during the takeoff. From the left, the first panel shows the bending angle anomaly from the COSMIC GPS RO acquired at 17.46 UTC, the second panel shows the temperature from the RO (red) and the temperature during the takeoff (black), the third shows the volume depolarization (green) and the backscatter ratio (blue) from MAS and the last panel shows the water vapor mixing ratio from the RO (red) and from FISH (blue).

During the landing the temperature profile from the aircraft does not show the lowest inversion (Figure 5.36, second panel from the left, blue line) and the cloud structure is different from the one at the takeoff with a water vapor mixing ratio from FISH which is in general higher than the RO.

Beside the comparison between the RO and the aircraft measurement (that can be argued because of the spatial and temporal co-location uncertainty), in this case it is interesting to highlight, during both the takeoff and the landing, the same thermal structure that we have found using the GPS ROs and CALIPSO: on the top of the cloud (detected from MAS, in this case) the temperature reaches the minimum value and a warming is evident above the cloud top.

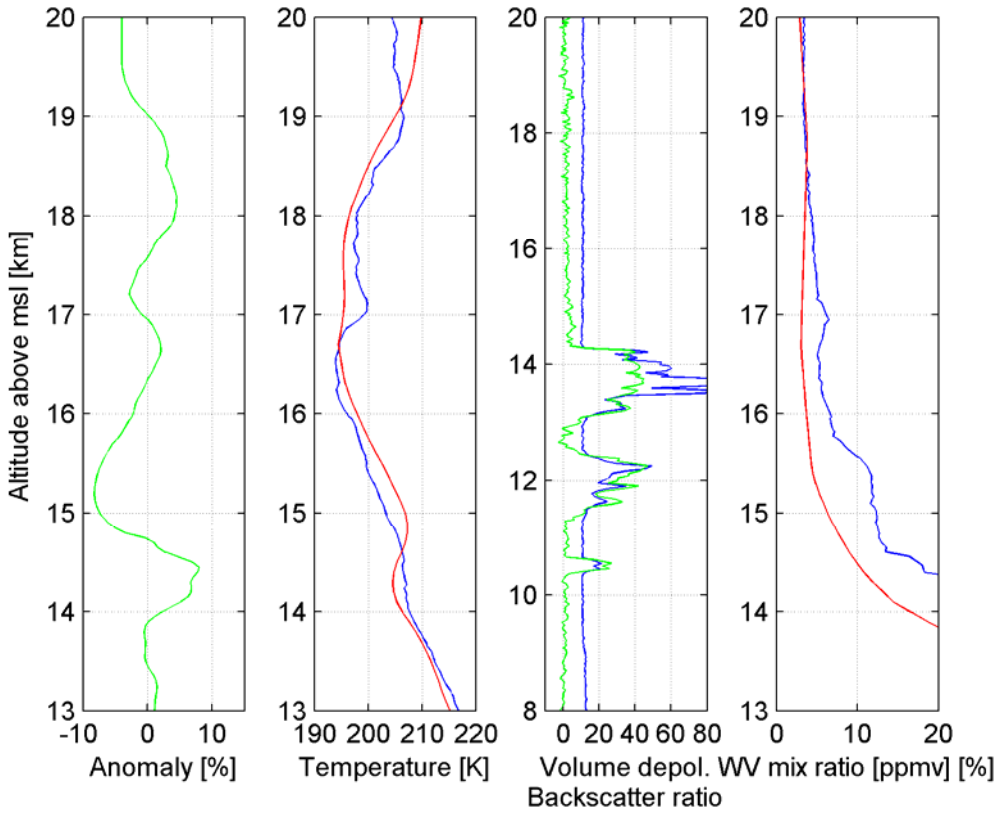

Figure 5.36: Atmospheric profiles the 8th of August 2006 during the landing. From the left, the first panel shows the bending angle anomaly from the COSMIC GPS RO acquired at 17.46 UTC, the second panel shows the temperature from the RO (red) and the temperature during the landing (black), the third shows the volume depolarization (green) and the backscatter ratio (blue) from MAS and the last panel shows the water vapor mixing ratio from the RO (red) and from FISH (blue).

b) AMMA 11th of August 2006

Figure 5.37 shows the Geophysica M55 track together with the tangent points of 2 GPS ROs from COSMIC. It is not possible to distinguish the 2 different ROs, since they were superimposed. The ROs were acquired at 15.24 UTC and at 15.25 UTC and, as we did for the previous case, they were compared with the profiles measured by the aircraft

during the takeoff from 14.40 UTC to 15.40 UTC (Figure 5.38) and the landing from 17.40 UTC to 18:20 UTC (Figure 5.39).

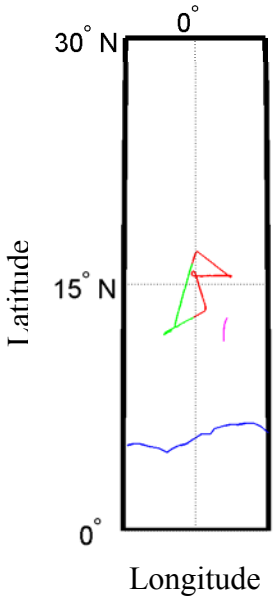

Figure 5.37: Flight track (green and red) of Geophysica M55 the 11th of August 2006. The green part is the takeoff (14.40 UTC-15.40 UTC) and the landing (17.40 UTC-18:20 UTC). The coast line is blue and the COSMIC GPS ROs tangent point are magenta (2 different ROs are superimposed).

The $\alpha_{Anomalies}$ (Figure 5.38 and 5.39, first panel from the left) show a spike at about 14.9 km of altitude and then another one at about 17.1 km with the corresponding temperature profile (Figure 5.38, second panel from the left, red line) showing a double inversion at the same altitudes as the $\alpha_{Anomaly}$ spikes. During the takeoff the aircraft temperature profile (black) shows the lower inversion at about 15.8 km and the upper at 17 km. As already described in the previous case, the temperature inversion from the aircraft corresponds to the cloud top showed by MAS (Figure 5.38, third panel from the left) and a large increase of water mixing ratio is highlighted by FISH (almost 10 ppmv) and FLASH (about 5 ppmv) at the same altitude. The large difference between the measurements of FISH and FLASH is due to the fact that FISH is a "forward" instrument measuring total water (gas phase and ice particles) and FLASH is a "backward" instrument measuring just the gas phase.

The time and space distance (almost 3 hours and a few hundred km) between the takeoff and the GPS RO can explain the different thermal structure.

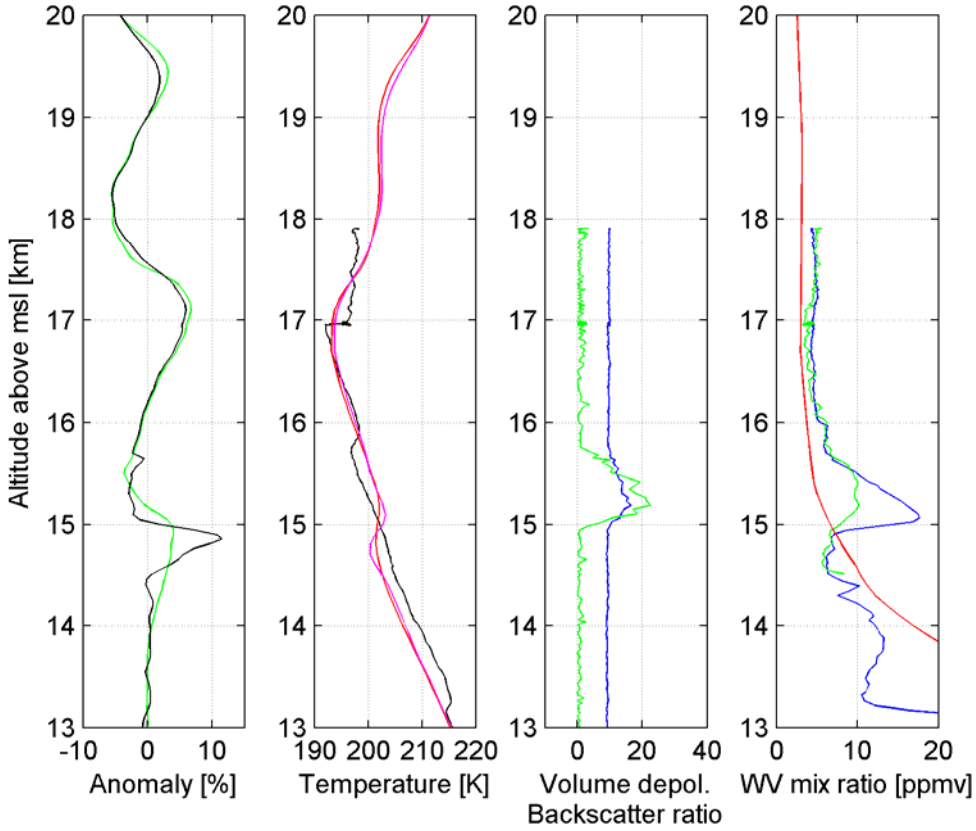

Figure 5.38: Atmospheric profiles the 11th of August 2006 during the takeoff. From the left, the first panel shows the bending angle anomalies from the COSMIC GPS ROs acquired at 15.24 and 15.25 UTC, the second panel shows the temperatures from the RO (red and magenta) and the temperature during the takeoff (black), the third shows the volume depolarization (green) and the backscatter ratio (blue) from MAS and the last panel shows the water vapor mixing ratio from the RO (red) from FISH (blue) and from FLASH (green).

The landing was temporal co-located with the RO. In this case the temperature profile from the aircraft and the RO almost agree (Figure 5.39, second panel from the left) and they behave according to the thermal structure depicted in Figure 5.33: the $\alpha_{Anomaly}$ shows the spike at 14.9 km of altitude which corresponds to the temperature inversion, which in turn corresponds to the cloud top as shown by MAS backscatter ratio and volume depolarization. The water vapor mixing ratio from the aircraft is in general higher than the same parameter from RO.

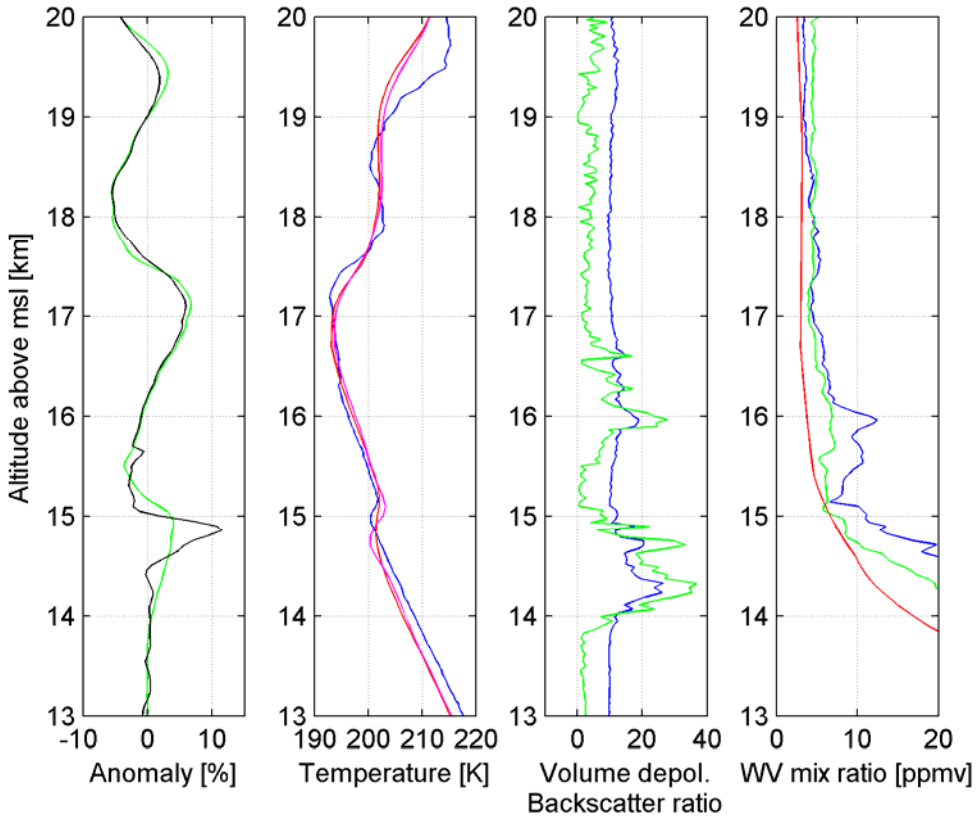

Figure 5.39: Atmospheric profiles the 11th of August 2006 during the landing. From the left, the first panel shows the bending angle anomalies from the COSMIC GPS ROs acquired at 15.24 and 15.25 UTC, the second panel shows the temperatures from the RO (red and magenta) and the temperature during the landing (black), the third shows the volume depolarization (green) and the backscatter ratio (blue) from MAS and the last panel shows the water vapor mixing ratio from the RO (red) from FISH (blue) and from FLASH (green).

c) TC4 6th of August 2007

During TC4 campaign we have analyzed an interesting colocation of 1 GRACE RO with CPL from ER-2 and a high resolution RAOB launched from Galapagos station.

Figure 5.40 shows the ER-2 track (red), the location of Galapagos RAOB station (blue circle), the GRACE RO tangent point (magenta line) and the location of the closest CPL acquisition to the RO (black circle).

The balloon from Galapagos was ascending from 13.59 UTC to 15.25 UTC and descending from 15.25 UTC to 16.02 UTC, the RO was acquired at 16.02 UTC (during the descending RAOB profile) and ER-2 with onboard the CPL overpassed the area at 15.16 UTC.

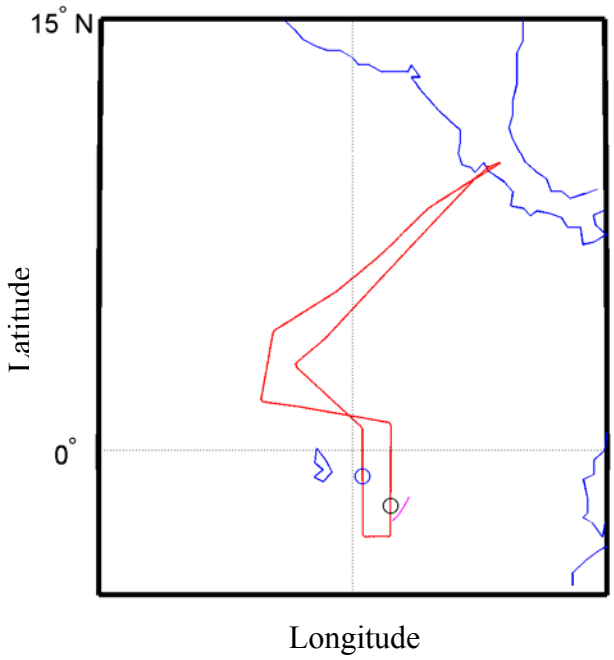

Figure 5.40: Flight track (red) ER-2 the 6th of August 2007. The coast line is blue, the GRACE GPS RO tangent point is magenta, the blue circle is the RAOB station and the black circle is the closest CLP acquisition to the RO.

Figure 5.41 in the left panel shows the temperature profiles from the RAOB (blue lines) and from the RO (magenta line). The RAOB temperature profiles present a first inversion at about 16.4 km of altitude and a second one at 17.3 km during the ascending phase, and they are 200 meters lower during the descending phase. The RO temperature profile, instead, present an inversion at 16.8 km which corresponds to the $\alpha_{Anomaly}$ spike (right panel) and it does not agree with any RAOB profile. The CPL on board of the aircraft measures the cloud top at about 15.8 km near the RO tangent point and the cloud top at 16.35 km overpassing the RAOB station at about 14.40 UTC. The $\alpha_{Anomaly}$ spike altitude and the RO temperature inversion do not agree with the cloud top detected by CPL; however the temperature inversion measured from the RAOB exactly corresponds to the CPL cloud top according to the thermal structure that was defined in the paragraph 5.3.2.

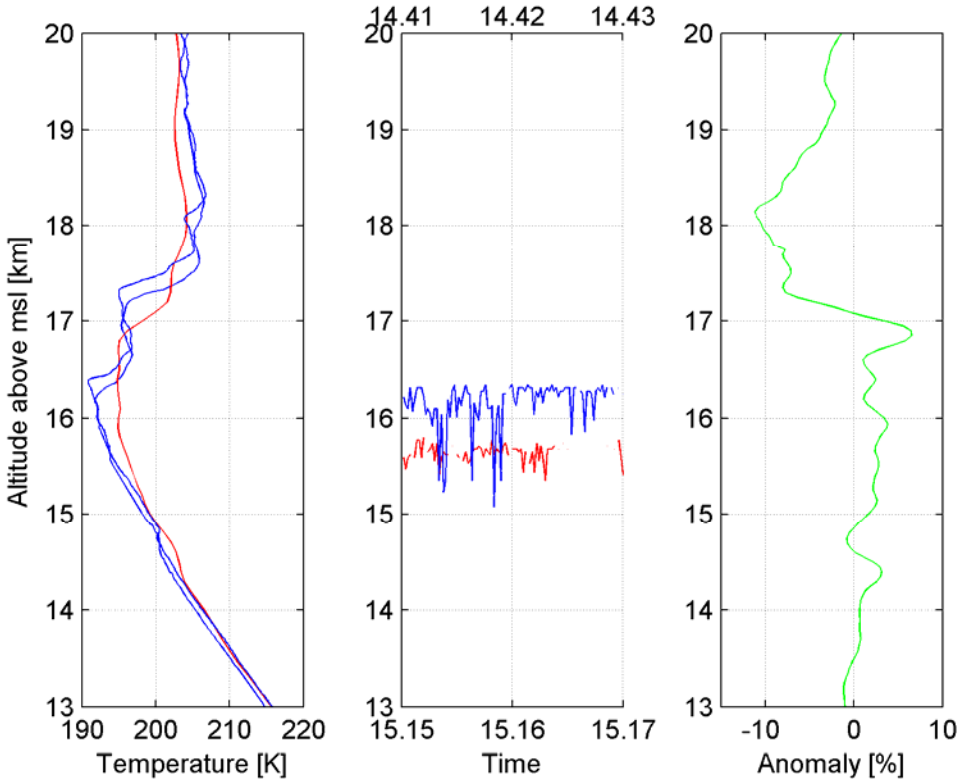

Figure 5.41: Atmospheric profiles the 6th of August 2007. The left panel shows the temperature from the COSMIC GPS ROs (red) acquired at 16.02 UTC, from the ascending (13.59 UTC-15.25 UTC) and descending (15.25 UTC-16.02 UTC) RAOB (blue). The central panel shows the cloud top altitude co-located with RAOB (blue, top x-axis) and the cloud top altitude co-located with RO (red, bottom x-axis) from CPL. The right shows the bending angle anomaly.

Chapter 6

Discussion

6.1 Results

The first result reached during this work is the estimation of ACES contribution to the analysis of convective systems. As described in the paragraph 2.5, thanks to the inclination of the ISS orbit, ACES will increase the number of GPS ROs in the tropical area by 32% in respect to the actual number COSMIC soundings.

We have created an algorithm to detect convective systems (Chapter 4) and their cloud top altitude using the GPS RO bending angle anomaly with respect to the climatological background. The analysis of the GPS ROs coverage has shown that the number of GPS ROs acquired from the past and ongoing mission is not dense enough for CSs studies based on monthly climatology (paragraph 4.2) especially in the tropical area and denser soundings are required to improve the algorithm on seasonal basis.

The present technology does not allow us to retrieve information regarding the water vapor in the UTLS even during extreme cases like TCs or deep CSs, but really interesting information can be retrieved on the thermal structure of the storms with high accuracy and vertical resolution in the UTLS (paragraph 5.1).

The results show that the bending angle anomaly provides a clear signature of the top of TCs and CSs and an unexpected cooling corresponds to this altitude (paragraphs 5.2 and 5.3). When the top of the cloud is far enough from the standard tropopause level, an evident double tropopause is detectable, the lower one corresponding to the top of the cloud and the higher one corresponding to the standard tropopause. When the storm reaches the standard tropopause altitude it is more difficult to distinguish the two contributions, but the signature is still evident in the bending angle anomaly profile. The double tropopause during the convection was already detected during campaigns from Danielsen, (1982), Pommereau and Held (2007) and Corti (2008), but the use of GPS RO allowed to get a systematic algorithm to detect this kind of process. Differently from Danielsen theory, the results of this study show that the lower tropopause is located at the cloud top. The thermal structure of the CSs, shows that the temperature from the surface decreases with a moist adiabatic lapse rate until a few kilometers from the cloud top. At this altitude, the lapse rate increases getting the dry adiabatic lapse rate in correspondence of the cloud. This reveals an extremely cold point at the top of the convective system. Above the cloud top a quick warming occurs, re-establishing a climatological-like

temperature trend. With a moist adiabatic lapse rate, the temperature reaches the coldest point at the tropopause level.
The comparisons with co-located independent datasets (CALIPSO, and RAOB), despite the uncertainties that we should take in account (paragraph 6.2), confirm that the bending angle anomaly could be a good tool for the detection of the CSs and TCs cloud top. The further comparison with models (paragraph 5.2.4) and campaigns (paragraph 5.3.3) data confirms the good quality of the results of this project. The high vertical resolution of the GPS RO allows to profile the convective systems with great accuracy and to resolve all these features otherwise not detectable with other instruments.

6.2 Uncertainties of the method

As already shown in the section 2, RO detected bending angle reflects the bending of RO ray due to atmospheric density which is function of temperature, water vapor content, and the pressure of the atmosphere. Any variation of these parameters influences the bending angle in a different way and with different amplitude. During the TCs and deep CSs, many processes combine their effects at the same time changing the physics of the atmosphere. The strong convection leads to an increase of water vapor in the mid troposphere and sometimes to the water vapor overshooting into the stratosphere (Romps and Kuang, 2009). At the same time, the temperature increases in the low and mid troposphere, but the tropopause layer usually becomes colder (Sherwood et al., 2003). Gravity waves can also be found at the top of the storms (Ming et al., 2010).
The bending angle is sensitive to all these processes and their contributions are sometimes difficult to distinguish. The derived bending angle anomaly can be due either to one single contribution or to a combination of many. The climatology that we realized using all the available GPS ROs is really solid since the bending angle anomaly during the convection with respect to the monthly mean, the annual mean or the full datasets mean, always provides the same features, as described in the paragraph 4.2.
In the paragraph 5.1 it has been also discussed the possible contribution of the water vapor to the bending angle variation and the accuracy of the RO soundings. The water vapor content in the UTLS is usually very small, up to 8-10 ppmv in the extreme cases (Corti et al., 2008) and this amount cannot cause such big $\alpha_{Anomaly}$ that we observe during the TCs. When the cloud top reaches lower altitudes (about 11-12 km) the water vapor can be up to several hundred ppmv, according to collocated AIRS (Randel and Park, 2006) measurements, but the corresponding changes in temperature are expected to be small (< 0.5 K; Sergey Sokolovskiy, personal communication 2011), and hence this is not an important source of bias in the results (Biondi et al., 2011c).

The reason of this temperature variation can be attributable either to the radiative effect of the storm anvil (or any other cloud formed by the convective system, i.e. jumping cirrus), or to the turbulent mixing due to the overshooting or to the waves.
Just in a few cases we were able to check whether the temperature variation is due to the gravity waves. In order to verify it, we need to get a reasonable number of profiles in a large area around the storm for a relatively long period and this is unfortunately very difficult because the RO coverage is not good enough and because the TCs are mostly over the ocean where not many RAOBs stations are available. However, in some cases we could check it, finding out temperature and bending angle variations attributable to gravity waves (the variation was propagated also in the surrounding areas not perturbed by the storm), but also cases where their effect could be excluded because the variation was evident just at the top of the storm and it was not propagated either horizontally or vertically (i.e. the convective system on the 2nd of February 2008 reported in the section 5.3.1).
Comparing the RO profiles with independent measurements (i.e. RAOBs and CALIPSO) we need to consider some issue that could lead to errors and misinterpretations. The temporal and spatial mis-matches between RO data and RAOB/CALIPSO data could lead to uncertainty of RO_{ctop} especially for phenomena like TCs changing their vertical and horizontal structure really quickly. The vertical resolution is another factor which could lead to RO_{ctop} uncertainty. The measurements that we use as reference, (i.e. RAOBs or ECMWF model) are often not able to resolve the feature that we can see from the high vertical resolution of the RO profile. Finally, as already mentioned in the paragraph 5.1, the comparisons with data provided as function of the pressure (i. e. RAOBs) could introduce errors since the measurements or estimations at the same altitudes could be different from measurements (or estimations) at the same pressure surface (Kuo et al., 2004).

6.3 Applications

An interesting application of the $\alpha_{Anomaly}$ technique could be the determination of cloud top height of the same storm at different stages linking the cloud top height to the intensity of the storm. The GPS ROs missions are increasing with the time due the relative low cost and this will partly increase the coverage of the Earth and the temporal resolution. A few polar missions with GPS RO receivers on board has already been launched with similar orbits like SAC-D, OceanSat-2 and MetOp-A and others are planned in the near future such as MetOp-B/C, ACES and COSMIC-2. On the other hand, the number of transmitters will drastically increase with the European GALILEO system, with the availability of the Russian GLObal NAvigation Satellite System

(GLONASS) and with the new projects from China (COMPASS), India (Indian Regional Navigational Satellite System, IRNSS) and Japan (Quasi-Zenith Satellite System, QZSS). Using just COSMIC ROs we are sometimes able to follow large TCs with long tracks, getting profiles during different status as shown in paragraph 5.2.1. With the contribution of the upcoming missions this kind of study will become definitely easier.
Following the studies of Wong and Emanuel (2007), the $\alpha_{Anomaly}$ (in terms of cloud top detection) could be linked to the intensity of the storm, providing an interesting tool for the forecast of extreme events. Many profiles during CSs and TCs up to category 1 status are already collected, since they are the most frequent stages, but the profiles during stronger events are really rare, thus a better coverage of the Earth is requested for improving the analysis of the intensity of the storm.
Since the technique is independent from the physical cause of the convection and cloud formation, and it just depends on the variation from the climatology, it could also be applied to different types of clouds being able to detect low clouds (in the lower or mid troposphere) or volcanic cloud ash supporting other platform measurements in managing hazard warnings.
As already explained in the paragraph 2.5, the actual coverage of the RO ongoing missions is not enough to address seasonal or monthly variability (especially in the tropical area). With the availability of the new GPS RO sensors, more detailed investigation will be possible like seasonal and monthly climatology connected to zonal periodic variability (e.g. Asian monsoon circulation).

6.4 Originality, relevance and impact of the project

The $\alpha_{Anomaly}$ technique is a new procedure, never used before. This approach to the study of CSs is completely new, versatile and looking to the future due the extremely low cost of the receivers and the facility to be mounted in any kind of satellite, aircraft and balloon. The temporal and spatial coverage of the Earth is potentially the highest possible (when GPS, GLONASS, GALILEO, COMPASS, IRNSS, QZSS will be active together with ACES, COSMIC-2, MetOp and many other small satellites) overtaking any other technique for the study of the cloud top, the strength of the storms and the UTLS. This technique is well suited for the study of severe weather phenomena since the radiowave signal is not affected by the presence of the clouds, the extremely high vertical resolution is a unique tool to detect quick atmospheric density variation (not detectable from any other satellite sensor) and the sensitivity of the bending angle measurements allow us to avoid any problem due to the use of model assimilations. The $\alpha_{Anomaly}$ technique allows us to detect and amplify variations of the bending angle itself otherwise not detectable due to the small values of these parameters. With respect to the state of the

art, the bending angle technique will provide a global coverage of the Earth in studying convective systems, the best vertical resolution as possible with the present technology, an accuracy in the cloud top determination higher than other techniques developed so far and improvement in the determination of the storm strength.

This work contributed to increase the capability of the GPS RO databases and to improve the knowledge on the UTLS during the convection, which is needed for forecasting and climate changes studies. In this way it could be relevant and beneficial for several meteorological and climatological programmes such as the Global Earth's Water Experiment (GEWEX) Cloud Systems Study (GCSS), the CLImate VARiability and predictability (CLIVAR), the Global Earth Observation System of Systems (GEOSS) and the Stratospheric Processes and their Role in Climate within the World Climate Research (SPARC) helping the development of weather forecast, the understanding of the climate changes and the impact of the convection on the climate changes.

Chapter 7

Summary and conclusions

In this thesis, we presented a new approach for convective systems analysis using the GPS RO technique.

The convection plays a fundamental role in the troposphere-stratosphere interaction influencing the climate changes. The convective systems change the thermal structure of the atmosphere and they can have overshoots penetrating the tropopause and injecting water vapor in the stratosphere. As shown by Solomon et al. (2010) the increase of stratospheric water vapor has a climatic impact comparable to those due to carbon dioxide. The study of UTLS (especially during extreme events) is very difficult and for this reason the processes which determine the details of the UTLS structure and change the stratospheric water vapor content are still debated. The global coverage, the independence from the weather conditions, the high vertical resolution and high accuracy make the GPS ROs a good tool to study the UTLS and to understand the UTLS processes governing the troposphere-stratosphere transport. The future ACES mission will contribute to the increase of RO in the tropics enhancing this kind of analysis.

In this work we used several different datasets. The GPS ROs from all the past and ongoing missions were collected as primary dataset for the analysis of the convective systems. The GPS soundings coordinates were compared with the location of TCs (from the TC best track archives) and CSs (from ISCCP Deep Convection Tracking Database) to get profiles co-located with the storms. In order to validate the results we used independent datasets as total attenuated backscatter from satellite (CALIPSO), RAOB profiles, airborne data and ECMWF model analysis. We used other satellite (GOES, GMS, MTSAT) data and ground based acquisitions (WWLLN) to detect the exact location of overshooting. Then we validated the thermal structure during of TCs with simulations from a meso-scale model (CM1).

We developed the bending angle anomaly technique using the GPS bending angle profile during the convective system and analyzing its variation ($\alpha_{Anomaly}$) with respect to the climatology. We conducted a sensitivity analysis showing that the bending angle is not affected by the water vapor variation in the UTLS. However the $\alpha_{Anomaly}$ analysis has shown a typical “TC trend” highlighting a clear signature of the convection in the UTLS due to the temperature variation.

We reported several case studies and statistics describing the capabilities of the bending angle technique to detect the convective systems (including TCs) cloud top altitude and to analyze their thermal structure. We also provided comparisons with independent co-located measurements corroborating the results obtained with the ROs.

We highlighted the final results taking into account the uncertainties of the method and we described the impact and future applications of this work.

It is time to give an answer the questions asked in the introduction chapter.

The first question was: what is the contribution that the future missions ACES will provide to the study of the convection?

As discussed in the paragraph 2.4, the coverage of the ongoing GPS RO missions is not uniformly distributed. Due to the orbit inclination, the mid-latitudes are covered better than the tropics. ACES will add a large number of occultations within the tropics increasing the actual coverage by 32% particularly beneficial for the convective systems studies.

The second question was: is the GPS signal able to provide information on the water vapor content in the UTLS during extreme events?

In the paragraph 5.1 we have demonstrated that, even during extreme events when the water vapor is moved to upper altitudes from the convection, the influence of the water vapor on the refractivity and bending angle variation is negligible. Thus, the answer to this question should be “no”.
After all the studies I would answer “not directly”. The convection increases the water vapor of the UTLS through the overshooting, but the variation at those altitudes is too small (just a ppmv) to be detected with the GPS signal according to the present knowledge. The model retrieving the secondary products from the GPS signal is not able to distinguish the contribution given by the water vapor to the bending angle variation in the UTLS, but this does not mean that there is no contribution. If it is assumed that the overshooting in general contributes to the increase of the water vapor content in the UTLS, the detection of overshooting also allows the assessment of the water vapor content during the convection.

The last question was: is the GPS signal able to provide any interesting information on troposphere-stratosphere transport?

The answer is definitely “yes”. We have demonstrated that the GPS signal can be used to characterize the thermal structure of the convective systems, but it is especially suited to detect the storm cloud top. The bending angle contains interesting information in connection to the troposphere–stratosphere transport and the bending angle anomaly technique helps in characterizing this process. The bending angle anomaly has a specific trend during the TCs and the CSs giving a clear signature of these processes on the atmosphere. The double tropopause is another feature characterizing them.

References

Intergovernmental Panel on Climate Change (IPCC), The Scientific Basis, edited by: J. T. Houghton, Y. Ding, D. J. Griggs, M. Noguer, P. J. vand der Linden, X. Dai, K. Maskell, and C. A. Johnson, 881 pp., Cambridge Univ. Press, New York, 2001

Adriani, A., Viterbini, M., Cairo, F., Mandolini, S. and Di Donfrancesco, G.: Multiwavelength Aerosol Scatterometer for airborne experiments to study the stratospheric particle optical properties. J. Atmos. Oceanic Technol., 16, 1328–1335, 1999

Anthes, R. A., Bernhardt, P. A., Chen, Y., Cucurull, L., Dymond, K. F., Ector, D., Healy, S. B., Ho, S.-H., Hunt, D. C., Kuo, Y.-H., Liu, H., Manning, K., McCormick, C., Meehan, T. K., Randel, W. J., Rocken, C., Schreiner, W. S., Sokolovskiy, S. V., Syndergaard, S., Thompson, D. C., Trenberth, K. E., Wee, T.-K., Yen, N. L., and Zeng, Z.: The COSMIC/Formosat/3 mission: Early results, Bull. Amer. Meteor. Soc., 89, 313-333, 2008

Bath, G.S., Chakraborty, A., Nanjundiah, R.S. and Srinivasan, J.: Vertical thermal structure of the atmosphere during active and weak phases of convection over north Bay of Bengal: observation and model results, Curr. Sci. India, 83, 296-302, 2002

Beyerle, G., Wickert, J., Schmidt, T. and Reigber, C.: Atmospheric sounding by GNSS radio occultation: An analysis of the negative refractivity bias using CHAMP observations. J. Geophys. Res., doi:10.1029/2003JD003922, 2004

Beyerle, G., Schmidt, T., Michalak, G., Heise, S., Wickert, J., and Reigber, Ch.: GPS radio occultation with GRACE: Atmospheric Profiling utilizing the zero difference technique, Geophys. Res. Lett., 32, L13806, 2005

Biondi, R., Neubert, T., Syndergaard, S., Nielsen, J.: Measurements of the upper troposphere and lower stratosphere during tropical cyclones using the GPS radio occultation technique, Adv. Space Res., 47, 348-355, 2011a

Biondi, R., Neubert, T., Syndergaard, S., Nielsen, J.: Radio occultation bending angle anomalies during tropical cyclones, Atmos. Meas. Tech., 4, 1–25, doi:10.5194/amtd-4-1-2011, 2011b

Biondi, R., Randel, J. W., Ho, S. P., Neubert, T. and Syndergaard, S.: Thermal structure of convective clouds derived from GPS radio occultations, Atmos. Chem. Phys. Discuss., 11, 29093–29116, doi:10.5194/acpd-11-29093-2011, 2011c

Biondi, R., Ho, S. P., Randel, J. W., Neubert, T. and Syndergaard, S.: Tropical cyclone cloud top detection using the GPS bending angle, Atmos. Meas. Tech.,, in preparation, 2011d

Borrmann, S., Stefanutti, L. and Khattatov, V.: Chemistry and aerosol measurements on the Geophysika Stratospheric Research Aircraft: The Airborne Polar Experiment. Phys. Chem. Earth, 20, 97–101, 1995

Brasseur, G. P. and Solomon, S.: Aeronomy of the Middle Atmosphere, Second Edition, D. Reidel, Dordrecht, 1984

Braun, J.J., Van Hove, T., & Mayo, T.: Observed integrated moisture fields within tropical storm systems, 11th Symposium on Integrated Observing and Assimilation Systems for the Atmosphere, Oceans, and Land Surface (IOAS-AOLS), 2007

Brewer, A. W.: Evidence for a world circulation provided by the measurements of helium and water vapor distribution in the stratosphere, Q. J. Roy. Meteor. Soc., 75, 326, 351–363, 1949

Bryan, G. H. and Fritsch, J. M.: A benchmark simulation for moist nonhydrostatic numerical models. Mon. Wea. Rev., 130, 2917–2928, 2002

Bryan, G. H. and Rotunno, R.: The maximum intensity of tropical cyclones in axisymmetric numerical model simulations. Mon. Wea. Rev., 137, 1770–1789, 2009

Cairo, F., Buontempo, C., MacKenzie, A.R., Schiller, C., Volk, C. M. , Adriani, A., Mitev, V., Matthey, R., Di Donfrancesco, G., Oulanovsky, A., Ravegnani, F., Yushkov, V., Snels, M., Cagnazzo, C., and Stefanutti, L.: Morphology of the tropopause layer and lower stratosphere above a tropical cyclone: a case study on cyclone Davina (1999), Atmos. Chem. Phys. 8, 3411-3426, 2008

Cairo, F., Pommereau, J. P., Law, K. S., Schlager, H., Garnier, A., Fierli, F., Ern, M., Streibel, M., Arabas, S., Borrmann, S., Berthelier, J. J., Blom, C., Christensen, T., D'Amato, F., Di Donfrancesco, G., Deshler, T., Diedhiou, A., Durry, G., Engelsen, O., Goutail, F., Harris, N. R. P., Kerstel, E. R. T., Khaykin, S., Konopka, P., Kylling, A., Larsen, N., Lebel, T., Liu, X., MacKenzie, A. R., Nielsen, J., Oulanowski, A., Parker, D. J., Pelon, J., Polcher, J., Pyle, J. A., Ravegnani, F., Rivire, E. D., Robinson, A. D., Rckmann, T., Schiller, C., Simes, F., Stefanutti, L., Stroh, F., Some, L., Siegmund, P., Sitnikov, N., Vernier, J. P., Volk, C. M., Voigt, C., von Hobe, M., Viciani, S., and Yushkov, V.: An introduction to the SCOUT-AMMA stratospheric aircraft, balloons and sondes campaign inWest Africa, August 2006: rationale and roadmap, Atmos. Chem. Phys., 10, 2237–2256, doi:10.5194/acp-10-2237-2010, 2010

Cardinali, C.: Monitoring the observation impact on the short-range forecast. Q. J. R. Meteorol. Soc., 135, 239-250, 2009

Chaboureau, J.-P., Cammas, J.-P., Duron, J., Mascart, P. J., Sitnikov, N. M., and Voessing, H.-J.: A numerical study of tropical cross-tropopause transport by convective overshoots, Atmos. Chem. Phys., 7, 1731-1740, 2007

Chae, J. H., Wu, D. L., Read, W. G., and Sherwood, S. C.: The role of tropical deep convective clouds on temperature, water vapor, and dehydration in the tropical

tropopause layer (TTL), Atmos. Chem. Phys., 11, 3811–3821, doi:10.5194/acp-11-3811- 2011, 2011

Collard, A. D. and Healy, S. B.: The combined impact of future space-based atmospheric sounding instruments on numerical weather-prediction analysis fields: A simulation study, Q. J. R. Meteorol. Soc., 129, 2741-2760, 2003

Corti, T., Luo, B. P., de Reus, M., Brunner, D., Cairo, F., Mahoney, M. J., Martucci, G., Matthey, R., Mitev, V., dos Santos, F. H., Schiller, C., Shur, G., Sitnikov, N. M., Spelten, N., Vossing, H. J., Borrmann, S., and Peter, T.: Unprecedented evidence for overshooting convection hydrating the tropical stratosphere, Geophys. Res. Lett., 35, L10810, doi:10.1029/2008GL033641, 2008

Danielsen, E. F.: A dehydration mechanism for the stratosphere, Geophys. Res. Lett., 9, 605-608, 1982

Danielsen, E. F.: In situ evidence of rapid, vertical, irreversible transport of lower tropospheric air into the lower tropical stratosphere by convective cloud turrets and by larger-scale upwelling in tropical cyclones, J. Geophys. Res., 98, 8665-8681, 1993

Dessler, A. E. and Yang, P.: The distribution of tropical thin cirrus clouds inferred from Terra MODIS data, J. Climate, 16, 1241-1247, 2003

Dobson, G. B. M.: Origin and Distribution of the Polyatomic Molecules in the Atmosphere, P. Roy. Soc. Lond. A Mat., 236, 1205, 187-193, 1956

Dowden, R. L., Brundell, J. B., Rodger, C. J.: VLF lightning location by time of group arrival (TOGA) at multiple sites, J. Atmos. Sol.-Terr. Phy., 64, 7, 817-830, DOI: 10.1016/S1364-6826(02)00085-8 2002

Durre I., Vose R., Wuertz D. B. Overview of the integrated global radiosonde archive. Journal of Climate 19: 53–68, 2006

Fjeldbo, G., Kliore, A.J., Eshleman, V.R.: The Neutral Atmosphere of Venus as Studied with theMariner V Radio Occultation Experiments. Astron. J., 76, 123-140, 1971

Flury, T., Hocke, K., Haefele, A., Kampfer, N. and Lehmann, R.: Ozone depletion, water vapor in-crease, and PSC generation at midlatitudes by the 2008 major stratospheric warming, J. of Geophys. Res., 114, D18302, doi: 10.1029/2009JD011940, 2009

Forster P.M. and Shine, K.P.: Stratospheric water vapor changes as a possible contributor to observed stratospheric cooling, Geophys. Res. Lett. 26, 3309-3312, 1999

Forster, P. M. and Shine, K. P.: Assessing the climate climate impact of trends in stratospheric water vapor, Geophys. Res. Lett., 29, 101–102, 2002

Fueglistaler, S., Dessler, A.E., Dunkerton, T.J., Folkins, I., Fu, Q. and Mote P. W.: Tropical tropopause layer, Rev. Geophys., 47, RG1004, DOI:10.1029/2008RG000267, 2009

Gilmore, M. S., Straka, J. M. and Rasmussen, E. N.: Precipitation and Evolution Sensitivity in Simulated Deep Convective Storms: Comparisons between Liquid-

Only and Simple Ice and Liquid Phase Microphysics, Mon. Wea. Rev., 132, 1897–1916, 2004

Gorbunov, M. E. and Gurvich, A. S.: Comparative analysis of radioholographic methods of processing radio occultation data, Radio. Sci., 35, 1025-1034, 2000

Gorbunov, M. E.: Canonical transform method for processing radio occultation data in the lower troposphere, Radio. Sci., 37, 1076, doi:10.1029/2000RS002592, 2002

Grosvenor, D. P., Choularton, T. W., Coe, H., and Held, G.: A study of the effect of overshooting deep convection on the water content of the TTL and lower stratosphere from Cloud Resolving Model simulations, Atmos. Chem. Phys., 7, 4977-5002, doi:10.5194/acp-7-4977-2007, 2007

Haladay, T. and Stephens, G.: Characteristics of tropical thin cirrus clouds deduced from joint Cloudsat and Calipso observations, J. Geophys. Res., 114, D00A25, 2009

Hajj, G. A., Ao, C. O., Iijima, B. A., Kuang, D., Kursinski, E. R., Mannucci, A. J., Meehan, T. K., Romans, L. J., de La Torre Juarez, M., and Yunck, T. P.: CHAMP and SAC-C atmospheric occultation results and intercomparisons, J. Geophys. Res., 109, D06109, doi:10.1029/2003JD003909, 2004

Hartmann, D. L., Holton, J. R. and Fu, Q.: The heat balance of the tropical tropopause, cirrus, and stratospheric dehydration, Geophys. Res. Lett., 28, 1969–1972, 2001

Hofman, D.J. and Oltmans, S.J.: The effect of stratospheric water vapor on the heterogeneous re-action rate of ClONO2 and H2O for sulphuric acid aerosol, Geophys. Res. Lett., 19, 22, 2211-2214, 1992

Holton, J.R., Haynes, P.H., McIntyre, M.E., Douglass, A.R., Rood, R.B. and Pfister, L.: Stratosphere-Troposphere exchange, Rev. Geophys., 33, 95RG02097, 403-439, 1995

Holz, R. E., Ackerman, S., Antonelli, P., Nagle, F., Knuteson, R. O., McGill, M., Hlavka, D. L., and Hart, W. D.: An Improvement to the High-Spectral-Resolution CO2-Slicing Cloud-Top Altitude Retrieval, J. Atmos. Oceanic Technol., 23, pp. 653–670, doi: 10.1175/JTECH1877.1, 2006

Huang, C. Y., Kuo, Y. H., Chen, S. H. and Vandenberghe, F.: Improvements in Typhoon Forecasts with Assimilated GPS Occultation Refractivity, Weather Forecast., 20, 931–953, 2004

Jensen, A.S., Lohmann, M.S., Benzon, H.-H. and Nielsen, A.S.: Full spectrum inversion of radio occultation signals, Radio. Sci., 38, 1040, doi:10.1029/2002RS002763, 2003

Jensen, E., Pfister, L., Bui, T., Weinheimer, A., Weinstock, E., Smith, J., Pittman, J., Baumgardner, D., Lawson, P., and McGill, M. J.: Formation of a tropopause cirrus layer observed over Florida during CRYSTAL-FACE, J. Geophys. Res., 110, D03208, doi:10.1029/2004JD004671, 2005

Jones, R. L., Pyle, J. A., Harries, J. E., Zavody, A. M., Russell III, J. M. and Gille, J. C.: The water vapor budget of the stratosphere studied using LIMS and SAMS satellite data, Q. J. R. Meteorol. Soc., 112, 1127-1143, 1986

Kessler E.: On the distribution and continuity of water substance in atmospheric circulations, Am. Meteorol. Soc. Meteorol. Monogr., 32, 1969

King, M. D., Kaufman, Y. J., Menzel, W. P., and Tanre, D., : Remote sensing of cloud, aerosol and water vapor properties from the moderate resolution imaging spectrometer (MODIS), IEEE Trans. Geosci. Remote Sens., 30, 2-27, 1992

Kley, D., Schmeltekopf, A. L., Kelly, K., Winkler, R. H., Thompson, T. L., and McFarland, M.: Transport of water through the tropical tropopause, Geophys. Res. Lett., 9, 617-620, 1982

Kim, H.C., The effect of deep convection on temperatures in the tropical tropopause layer and its implications to the regulation of tropical lower stratospheric humidity. PhD Thesis, University of Houston, USA, 2005

King, M. D., Kaufman, Y. J., Menzel, W. P., and Tanre, D.: Remote sensing of cloud, aerosol and water vapor properties from the moderate resolution imaging spectrometer (MODIS), IEEE Trans. Geosci. Remote Sens., 30, 2-27, 1992

Kuo, Y. H., Wee, T. K., Sokolovskiy, S., Rocken, C., Schreiner, W., Hunt, D., and Anthes, R. A.: Inversion and error analysis of GPS radio occultation data, J. Meteor. Soc. Japan, 82, 507-531, 2004

Kuo, Y. H., Schreiner, W., Wang, J., Rossiter, D. L. and Zhang, Y: Comparison og GPS radio occultation soundings with radiosondes, Geophys. Res. Lett., 32, L05817, DOI: 10.1029/2004GL021443, 2005

Kursinski, E. R., Hajj, G. A., Schofield, J. T., Linfield, R. P. and Hardy, K. R.: Observing Earth's atmosphere with radio occultation measurements using the Global Positioning System, J. Geophys. Res., 102, 23429-23465, 1997

LeTexier, H., Solomon, S., and Garcia, R. R.: The role of molecular hydrogen and methane oxidation in the water vapor budget of the stratosphere, Q. J. R. Meteorol. Soc., 114, 281-295, 1988

Lin, Y. L., Farley, R. D., Orville, H. D.: Bulk parameterization of snow filed in a cloud model, J. Clim. Appl. Metereol., 22, 1065-1092, 1983

Liu, C. and Zipser, E. J.: Global distribution of convection penetrating the tropical tropopause, J. Geophys. Res., D23104, doi:10.1029/2005JD006063, 2005

Liu, C.: Geographical and seasonal distribution of tropical tropopause thin clouds and their reltion to deep convection and water vapor viewed from satellite measurements, J. Geophys. Res., 112, D09205, 2007

Luo, B.P., Peter, Th., Fueglistaler, S., Wernli, H., Wirth, M., Kiemle, C., Flentje, H., Yushkov, V.A., Khattatov, V., Rudakov, V., Thomas, A., Borrmann, S., Toci, G., Mazzinghi, P., Beuermann, J., Schiller, C., Cairo, F., Di Don Francesco, G., Adriani, A., Volk, C.M., Strom, J., Noone, K., Mitev, V., MacKenzie, R.A., Carslaw, K.S., Trautmann, T., Santace-saria, V. and Stefanutti, L.: Dehydration

potential of ultrathin clouds at the tropical tro-popause, Geophys. Res. Lett., 30, 11, 1557, 2003

Luo, Z., Stephens, G. L., Emanuel, K. A., Vane, D. G., Tourville, N. D., and Haynes, J. M.: On the use of CloudSat and MODIS data for estimating hurricane intensity, IEEE Geosci. Remote Sens. Lett., 5, 13– 16, 2008

Manabe, S., Wetherald, R.T.: Thermal equilibrium of the atmosphere with a given distribution of relative humidity, J. Atmos. Sci., 24, 241-259, 1967

McGill, M.J., Hlavka, D.L. Hart, W.D. Spinhirne, J.D. Scott, V.S. and Schmid, B.: The Cloud Physics Lidar: Instrument description and initial measurement results, Applied Optics, 41, 3725-3734, 2002

Miloshevich, L. M., Vömel, H., Whiteman, D. N., Lesht, B. M., Schmidlin, F. J. and Russo, F.: Absolute accuracy of water vapor measurements from six operational radiosonde types launched during AWEX-G and implications for AIRS validation. J. Geophys. Res., 111, D09S10, doi:10.1029/2005JD006083, 2006

Ming, F. C., Chen, Z., and Roux, F.: Analysis of gravity-waves produced by intense tropical cyclones, Ann. Geophys., 28, 531–547, 2010

Minnis, P., Yost, C. R., Sun-Mack, S., and Chen, Y.: Estimating the top of the cloud of optically thick ice clouds from thermal infrared satellite observations using CALIPSO data, Geophys. Res. Lett., 35, L12801, 2008

Molinari, J., Moore, P., Idone, V.,: Convective Structure of Hurricanes as Revealed by Lightning Locations. Mon. Wea. Rev., 127, 520–534, doi: 10.1175/1520-0493, 1999

Morrison, H., Curry, J. A., Khvorostyanov, V. I.: A New Double-Moment Microphysics Parameterization for Application in Cloud and Climate Models. Part I: Description. J. Atmos. Sci., 62, 1665–1677, doi: 10.1175/JAS3446.1, 2005

Neubert, T., Crosby, B., Huang, T. Y. et al., ASIM - an Instrument Suite for the International Space Station. AIP Conference Proceedings, pp: 8-12, DOI: 10.1063/1.3137718, 2009

Newell, R. E. and Gould-Stewart, S.: A stratospheric fountain?, J. Atmos. Science, 38, 2789–2796, 1981

Peter, Th., Luo, B.P., Wirth, M., Kiemle, C., Flentje, H., Yushkov, V.A., Khattatov, V., Rudakov, V., Thomas, A., Borrmann, S., Toci, G., Mazzinghi, P., Beuermann, J., Schiller, C., Cairo, F., Di Don Francesco, G., Adriani, A., Volk, C.M., Strom, J., Noone, K., Mitev, V., MacKenzie, R.A., Carslaw, K.S., Trautmann, T., Santacesaria, V. and Stefanutti, L.: Ultra-thin tropical tropopause clouds (UTTCs): I. cloud morphology and occurrence, Atmos. Chem. Phys., 3, 1083-1091, 2003

Peterson, T.C., and Baringer M.O.: State of the climate in 2008, Special supplement to BAMS, 90, 2009

Platnick, S., King, M. D., Ackerman, S. A., Menzel, W. P., Baum, B. A., Riedi, J. C., and Frey, R. A.: The MODIS cloud products: Algorithms and examples from Terra, IEEE Trans. Geosci. Remote Sens., 41, 459-473, 2003

Pommereau, J. P., and Held, G.: Is there a stratospheric fountain?, Atmos. Chem. Phys. Discuss., 7, 8933–8950, 2007

Puschell, J. J., Lowe, H. A., Jeter, J., Kus, S., Hurt, W. T., Gilman, D., Rogers, D. and Hoelter, R.: Japanese Advanced Meteorological Imager: A next generation GEO imager for MTSAT-1R. Proc. SPIE-Earth Observing Systems VII, 4814, 152-161, 2002

Ramaswamy, V, Schwarzkopf, M. D., Randel, W. J., Santer, B. D., Soden, B. J., Stenchikov, G. L.: Anthropogenic and Natural Influences in the Evolution of Lower Stratospheric Cooling, Science 311, 1138, DOI: 10.1126/science.1122587, 2006

Randel W. J., Wu., F., Vomel, H., Neduluha, G. E., Forster, P. M. D.: Decreases in stratospheric wa-ter vapor after 2001: Links to changes in the tropical tropopause and the Brewer-Dobson circulation, J. Geophys. Res., 111, doi:101029/2005JD006744, 2006

Ray, E.A. and Rosenlof, K.H.: Hydration of the upper troposphere by tropical cyclones, J. Geophys. Res., 112, D12311, 2007

Rocken C., Anthes, R., Exner, M., Hunt, D., Sokolovskiy, S., Ware, R., Gorbunov, M., Schreiner, W., Feng, D., Herman, B., Kuo, Y.-H., Zou, X.: Analysis and validation of GPS/MET data in the neutral atmosphere, J. Geophys. Res., 102, 29849-29860, 1997

Rodger, C. J., Brundell, J. B., and Dowden, R. L.: Location accuracy of VLF World Wide Lightning Location (WWLL) network: Post-algorithm upgrade. Ann. Geophys., 23, 277-290, 2005

Rohs, S., Schiller, C., Riese, M., Engel, A., Schmidt, U., Wetter, T., Levin, I., Nakazawa, T. And Aoki, S.: Long term changes of methane and hydrogen in the stratosphere in the period 1978-2003 and their impact on the abundance of stratospheric water vapor, J. .Geophys. Res., 111, D14315, 2006

Romps, D.M. and Kuang, Z.: Overshooting convection in tropical cyclones, Geophys, Res. Lett. 36, L09804, 2009

Rossow, W. B., and Schiffer, R. A.: Advances in understanding clouds from ISCCP, Bull. Am. Meteorol. Soc., 80, 2261– 2288, 1999

Rotunno, R., and Emanuel, K.: An air–sea interaction theory for tropical cyclones. Part II: Evolutionary study using a nonhydrostatic axisymmetric numerical model. J. Atmos. Sci., 44, 542–561, 1987

Scherer, M., Vömel, H., Fueglistaler, S., Oltmans, S. J., Staehelin, J.: Trends and variability of midlatitude stratospheric water vapor deduced from the re-evaluated Boulder balloon series and HALOE, Atmos. Chem. Phys., 8, 1391-1402, 2008

Schmetz, J., Tjembs S. A., Gube, M., and Van de Berg, L.: Monitoring deep convection and convective overshooting with Meteosat, Adv. Space Res., 19, 433-441, 1997

Schiller,C., Grooß, J.-U., Konopka, P., Ploger, F., Silva dos Santos, F. H. and Spelten N.: Hydration and dehydration at the tropical tropopause, Atmos. Chem. Phys., 9, 9647–9660, 2009

Schmit, T. J., Prins, E. M., Schreiner, A. J. and Gurka, J. J.: Introducing the GOES-M imager. Natl. Wea. Assoc. Digest, 25, 28–37, 2001

Seinfeld, J. H. and Pandis, S. N.: Atmospheric chemistry and physics: from air pollution to climate change, 2nd edition, Ed. Wiley Interscience, 2006

Sherwood, S.C., Horinouchi, T. and Zeleznik, H.A.: Convective impact on temperatures observed near the tropical tropopause, J. Atmos. Sci. 60, 1847–1856, 2003

Sherwood, S.C., Minnis, P., McGill, M., and J. C. Chae: Underestimation of deep convective cloud tops by thermal imagery, Geophys. Res. Lett., 31, L11102, doi:10.1029/2004GL019699, 2004

Shindell, D.T.: Climate and ozone response to increased stratospheric water vapor, Geophys. Res. Lett., 28, 8, 1551-1554, 2001

Soden, B.J., Fu, R.: A satellite analisys of deep convection, upper tropospheric humidity and the greenhouse effect. J. Clim., 8, 2333-2351, 1995

Sokolovskiy, S. V.: Tracking tropospheric radio occultation signals from low Earth orbit, Radio. Sci., 36, 483-498, 2001

Solomon, S., Rodenlof, K., Portmann, R. et al.: Contribution of stratospheric water vapor to decadal changes in the rate of global warming, Sciencexpress, doi:10.1126/science.1182488, 2010

Solorzano, N. N., Thomas, J. N. and Holzworth, R. H.: Using WWLLN and TRMM data to investigate lightning activity and convective parameters in 2005 - 2010 tropical cyclones, AGU Fall Meeting 2010, abstract #AE21A-0260

Stenke, A. and Grewe, V.: Impact of dynamically induced ozone mini-hole events on PSC formation and chemical ozone destruction, Climate Change Processes In The Stratosphere, Earth-Atmosphere-Ocean Systems, And Oceanographic Processes From Satellite Data Advances In Space Research, 33, 7, 1062-1067, 2004

Svehla, D., Rothacher, M., Ziebart, M. et al., Galileo on board International Space Station and synergy with the ACES clock ensemble. EGU General Assembly, 2006

Syndergaard, S.: Modeling of the effect of the Earth´s obleteness on the retrieval of temperature and pressure profiles from limb sounding, J. Atmos. Sol.-Terr. Phys., 60, 171-180, 1998

Tian W., Chipperfield, M.P. and Lu, D.: Impact of increasing stratospheric water vapor on ozone depletion and temperature change, Adv. Atmos. Sci., 26, 3, 423-437, 2009

Thompson, G., R. Rasmussen, M. and Manning, K.: Explicit forecasts of winter precipitation using an improved bulk microphysics scheme. Part I: Description and sensitivity analysis. Mon. Wea. Rev., 132, 519–542, 2004

Toon, O. B., Starr, D. O., Jensen, E. J., et al.: Planning, Implementation and First Results of the Tropical Composition, Cloud and Climate Coupling Experiment (TC4), J. Geophys. Res., 115, D00J04, 2010

Vaughan, M., Young, S., Winker, D., Powell, K., Omar, A., Liu, Z., Hu, Y., and Hostetler, C.: Fully automated analysis of space-based lidar data: An overview of the CALIPSO retrieval algorithms and data products, Proc. SPIE Int. Soc. Opt. Eng., 5575, 16–30, 2004

Wang, P. K.: Moisture plumes above thunderstorm anvils and their contributions to cross-tropopause transport of water vapor in midlatitudes, J. Geophys. Res., 108, D6, 4194, doi:10.1029/2002JD002581, 2003

Wennberg, P.O., Cohen, R. C., Stimpfle, R. M., Koplow, J. P., Anderson, J. G., Salawitch, R. J., Fahey, D. W., Woodbridge, E. L., Keim, E. R., Gao, R. S., Webster, C. R., May, R. D., Toohey, D. W., Avallone, L. M., Proffitt, M. H., Loewenstein, M., Podolske, J. R., Chan K. R. and Wofsy, S. C.: Removal of Stratospheric O-3 by Radicals - In-Situ Measurements of OH, HO2, NO, NO2, CLO, and BrO, Science, 266, 398-404, 1994

Wickert, J., Reigber, C., Beyerle, G., König, R., Marquardt, C., Schmidt, T., Grundwaldt, L., Galas, R., Meehan, T. K., Melbourne, W. G., and Hocke, K.: Atmosphere sounding by GPS radio occultation: First results from CHAMP, Geophys. Res. Lett., 28, 3263-3266, 2001

Winker, D. M., Hunt, W. H., and McGill, M. J.: Initial performance assessment of CALIOP, Geophys. Res. Lett., 34, L19803, doi:10.1029/2007GL030135, 2007

Wong, V., and Emanuel, K. A.: Use of cloud radars and radiometers for tropical cyclone intensity estimation, Geophys. Res. Lett., vol. 34, no. 12, L12811, DOI:10.1029/2007GL029960 , 2007

Yushkov, V., Merkoulov, S., Astakhov, V., Pommereau, J. P. and Garnier, A.: A lyman alpha hygrometer for long duriation IR montgol_er during lagrangian-THESEO experiment, in Stratospheric ozone 1999, Proc. of the 5th European Symposium on Stratospheric Ozone, edited by N. R. P. Harries, M. Guirlet, and G. T. Amanatidis, Air pollution research report 73, European Commission, 2000

Zoger, M., Afchine, A., Eicke, N., Gerhards, M.-T., Klein, E., McKenna, D., Morschel, U., Schmidt, U., Tan, V., Tuitjer, F., Woyke, T. and Schiller, C.: Fast in situ stratospheric hygrometers: A new family of balloon-borne and airborne Lyman a photofragment fluorescence hygrometers, J. Geophys. Res., 104, 1807–1816, 1999